AFRL-AFOSR-VA-TR-2020-0044

Resilient Self-Healing Materials for the Extreme Environment of Space Electric Propulsion & Power

NASR GHONIEM
UNIVERSITY OF CALIFORNIA LOS ANGELES

11/18/2019
Final Report

Air Force Research Laboratory
AF Office Of Scientific Research (AFOSR)/ RTA1
Arlington, Virginia 22203
Air Force Materiel Command

REPORT DOCUMENTATION PAGE

Form Approved
OMB No. 0704-0188

1. REPORT DATE *(DD-MM-YYYY)*	2. REPORT TYPE	3. DATES COVERED *(From - To)*
23-03-2020	Final Performance	30 Sep 2016 to 29 Sep 2019

4. TITLE AND SUBTITLE
Resilient Self-Healing Materials for the Extreme Environment of Space Electric Propulsion & Power

5a. CONTRACT NUMBER

5b. GRANT NUMBER
FA9550-16-1-0444

5c. PROGRAM ELEMENT NUMBER
61102F

6. AUTHOR(S)
NASR GHONIEM

5d. PROJECT NUMBER

5e. TASK NUMBER

5f. WORK UNIT NUMBER

7. PERFORMING ORGANIZATION NAME(S) AND ADDRESS(ES)
UNIVERSITY OF CALIFORNIA LOS ANGELES
11000 KINROSS AVE STE 102
LOS ANGELES, CA 90095-0001 US

8. PERFORMING ORGANIZATION REPORT NUMBER

9. SPONSORING/MONITORING AGENCY NAME(S) AND ADDRESS(ES)
AF Office of Scientific Research
875 N. Randolph St. Room 3112
Arlington, VA 22203

10. SPONSOR/MONITOR'S ACRONYM(S)
AFRL/AFOSR RTA1

11. SPONSOR/MONITOR'S REPORT NUMBER(S)
AFRL-AFOSR-VA-TR-2020-0044

12. DISTRIBUTION/AVAILABILITY STATEMENT
A DISTRIBUTION UNLIMITED: PB Public Release

13. SUPPLEMENTARY NOTES

14. ABSTRACT
The project objectives were to develop a fundamental understanding for the limits of using micro-engineered materials in Electric Propulsion (EE) and Pulsed Power (PP), and the opportunity to design material architectures that have dramatically improved their performance.

15. SUBJECT TERMS
plasma material coupling, sheat dynamics

16. SECURITY CLASSIFICATION OF:			17. LIMITATION OF ABSTRACT	18. NUMBER OF PAGES	19a. NAME OF RESPONSIBLE PERSON
a. REPORT	b. ABSTRACT	c. THIS PAGE			BIRKAN, MITAT
Unclassified	Unclassified	Unclassified	UU		19b. TELEPHONE NUMBER *(Include area code)* 703-696-7234

Standard Form 298 (Rev. 8/98)
Prescribed by ANSI Std. Z39.18

Resilient Self-Healing Materials for the Extreme Environment of Space Electric Propulsion & Power

Final Project Report

Air Force Office of Scientific Research (AFOSR)
Arlington, Virginia

(FA9550-16-1-0444)
RTB1 - Aerospace Materials for Extreme Environments

Program Managers: Ali Sayer & Mitat Birkan

For the Period
September 29, 2016 through September 30, 2019

Nasr M. Ghoniem, **Principal Investigator**
Telephone Number (310) 825-4866 E-mail: ghoniem@ucla.edu

Jaime Marian (UCLA) **Co-Principal Investigator**
Giacomo Po (UCLA) **Co-Principal Investigator**

Collaborators
Brian Williams (Ultramet, Inc.)
Richard Wirz, Yongjie Hu (UCLA)

Submitted by
Mechanical and Aerospace Engineering Department
University of California, Los Angeles (UCLA),
420 Westwood Plaza,
Los Angeles, CA. 90095-1597

Contents

1. Project Overview

Continued development of space Electric Propulsion (EP) and Pulsed Power (PP) systems relies on fundamental advances in our understanding of material performance and survival in extraordinarily severe environments. A wide range of structural and functional materials are employed in current day technologies. The materials of interest include conducting refractory metals (e.g. W, W-Re, Mo, Ta, and Re), insulating dielectric ceramics (e.g. BN and Al_2O_3), and high-strength copper alloys as heat sinks. These classes of materials serve various design functions; primarily in cathode and anode applications, in accelerator grids, and in beam dumps of High Power Microwave (HPM) sources.

The demand of higher performance materials is even greater in future technologies that will require materials to operate in substantially more aggressive environments. Several unique aspects distinguish the severe EP & PP environments. These are: (1) strong thermal and mechanical fields; (2) simultaneous plasma bombardment of the material; (3) coupled electric field; and (4) the severe, non-equilibrium phenomena are confined to a shallow surface layer. Understanding such characteristics and underlying physics present extraordinary opportunities in designing novel approaches to the development of plasma-resilient and self-healing materials for many technological applications of EP & PP. Figure 1 depicts the scaling of the lifetime FOM (Kw.hr/cm^2) versus a measure of the aggressiveness of the EP & PP environment (as the heat flux (MW/m^2, carried by plasma ions, photons, and electrons). The figure shows approximate FOM limits for current state-of-the art technologies (light green region). This includes some common technologies, like turbine blades of jet engines, photo-voltaic solar cells, as well as comparable technologies under development (e.g. fusion energy). The FOM ranges from 100-600 Kw.hr/cm^2 for the most demanding technologies of today. To achieve greater lifetimes in the future (e.g. in excess of 1000 Kw.hr/cm^2), new materials with special surfaces are required, and the science behind their degradation mechanisms must be clearly understood.

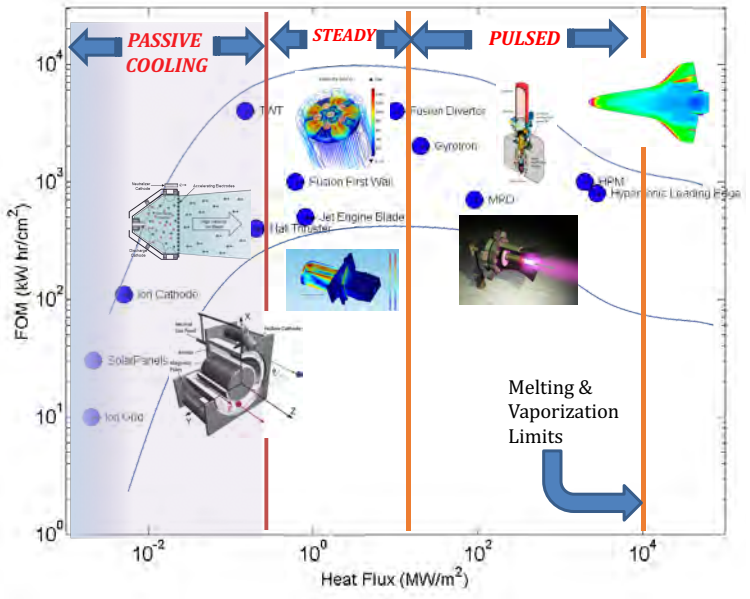

Figure 1: Lifetime Figure-Of-Merit (FOM) metric of plasma-facing materials measured in KW.hr/cm^2, as a function of the incident heat flux (rough indicator of environmental severity).

Plasma-Facing Materials (PFMs) in a wide range of space propulsion and power system applications are subjected to repetitive and intense heat and energetic particle flux in addition to mechanical loads. This leads to thermomechanical (TM) damage and eventual failure. In addition, the erosion rates due to ion and neutral-induced sputtering is so high that solid surfaces are not expected to last very long. The current program was aimed at the development of plasma-resilient micro-engineered refractory metals using the Chemical Vapor Deposition (CVD) process. Refractory metals with surface micro architecture are fabricated by the CVD process. The manufacturing method is extremely versatile and relatively inexpensive of molecular forming of materials and structures that are difficult to manufacture by conventional powder processing and machining. The benefits of CVD include the ability to produce deposits of controlled density, thickness, orientation, and composition. Purity levels in excess of 99.99% are achievable. In addition, the CVD process exhibits the greatest throwing power, or ability to uniformly deposit materials onto/into intricately shaped or textured substrates, thus allowing fabrication of near-net shape parts with geometries that cannot be produced through conventional processing and machining. Refractory metal dendrites (nano-rods) are grown from a substrate surface through control of the pressure and temperature of the CVD process. The diameter, length, surface density, and vertical taper can all be controlled. Another architecture is based on the deposition of refractory metals on reticulated graphite foams, then removing the graphite core and producing 3-D interconnected foam ligaments that form a "micro-truss." This foam architecture can be tailored through control of the relative density, foam cell-size, and ligament basic dimensions, thus controlling the effective thermal and mechanical properties. The third type of architecture that we investigated is a hybrid between the micro-pillar covered surface and the 3D reticulated foam microstructure. In this third architecture, dendrites (micro-pillars) are grown on top of every and each ligament of foam microstructure. Thus, a hierarchical" micro-engineered material is produced.

The project objectives were to develop a fundamental understanding for the limits of using micro-engineered materials in EE & PP, and the opportunity to design material architectures that have dramatically improved their performance. The project played a critical role in the establishment of the fundamental science base required for the development of new forms of materials that will reliably operate in the extreme, far-from-equilibrium, electric propulsion and pulsed power environments at unprecedented performance levels, resulting in vastly improved efficiencies and enabling new generations of technologies.

In the following, we discuss our main achievements during the funding period September 29, 2016 through September 30, 2019. The summary of our research funded by the current AFOSR grant, which is presented in section 2, will closely follow the four project tasks: (1) Development of nano- & micro-engineered materials; (2) Multiscale modeling of plasma interaction with complex surfaces; (3) In-situ testing of erosion and re-deposition; and (4) Experimental thermomechanics of micro-engineered materials. Furthermore, we present our research productivity and publications during the funding period in section 3.

2. Summary of Research Accomplishments

2.1. Task 1. Development of Nano & Micro-engineered Materials

In an effort to influence the implantation rate of energetic plasma ions into the surface, we increased the surface area that intercepts incoming ions. Thus, by increasing the exposed area while maintaining the incoming projected plasma flux, we expect a decrease in the local implantation

rate, leading to lower plasma damage. A geometrically convex shape extending from the metal surface will increase the exposed surface area. Furthermore, a conical/cylindrical shape would cause the incoming ions to strike the tungsten surface at an oblique angle of incidence. Ion backscattering increases with the deviation from normal incidence, and this will additionally decrease total ion deposition. While the bias potential of a slant surface tends to draw plasma ions towards it in a perpendicular direction, when the designed surface has high pillar density, ions would impact the surface normal to the projected area, resulting in a drastic increase in backscattering. Ultimately, the decrease of the effective ion flux via an increase in surface area and the corresponding increase in backscattering are both factors that have been explored experimentally.

Three different surface architectures have been fabricated with these ideas in mind. The fabrication process is primarily based on Chemical Vapor Deposition (CVD) [1], which is very versatile and can be controlled to produce the following architecture:

1. The first type of micro-engineered surface is covered with a uniformly dense layer of micro-pillars bonded firmly to an underlying substrate.
2. The second type is an open cell 3-dimensional foam structure, where each cell is composed of 12-14 ligaments, and the overall structure looks like a micro-truss.
3. The third type is fabricated by an additional step, where W is deposited as a coating on top of the uniform layer of dense Re micro-pillars.

We fabricated tungsten (W) pillar-covered surfaces, with conic tapered micro-pillars by growing such them atop of a tungsten substrate. The fabrication process starts with rhenium pillars deposited via CVD atop the tungsten substrate roughly 1 inch (25.4 mm) in diameter and 1/8 inch (3.175 mm) in thickness. Rhenium pillars are then coated with tungsten, which conforms to the conical shape of the Re pillars with a hexagonal cross-section. Two distinct pillar shapes are tested. One set has relatively thin and cylindrical pillars that are relatively dense across the substrate surface with diameter $\sim 1\mu$m and height of $\sim$20-25 μm. The other set of pillars are thicker and more conically shaped, with top diameter $\sim 2\mu$m, base diameter $\sim 8\mu$m, and height ~ 20 μm to 25 μm. These surface architecture are shown in Fig. 2. If one assumes uniformly placed pillars, the conic shapes would result in an $\sim$650% increase in surface area, while the cylindrical pillars would exhibit an $\sim$3000% increase in effective surface area. However, neither of these pillars are absolutely uniform, but grew rather randomly across the surface with some overlap. Nevertheless, there is an obvious significant increase in the effective surface area intercepted by incoming helium ions.

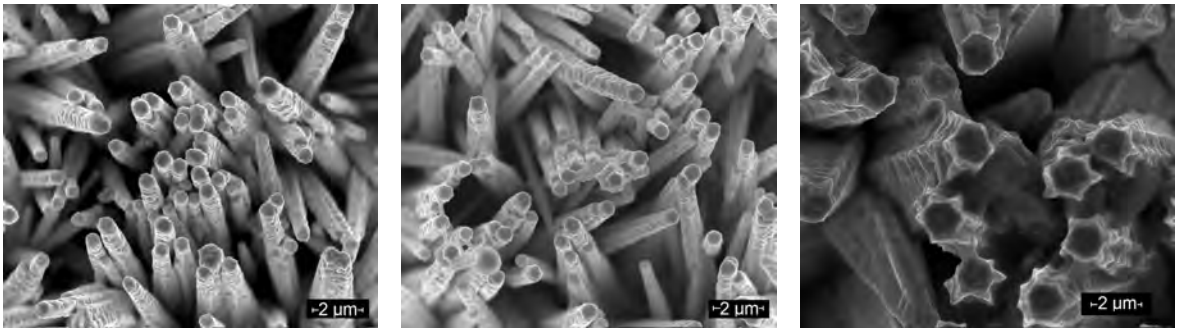

Figure 2: SEM images for thin cylindrical pillars, and thick conic pillars, shown at 10,000X magnification to depict pillar size, roughly 1-2 μm in diameter, and their density.

The second set of samples are fabricated with an architecture, where individual W-foam ligaments are covered with rhenium pillars. We will refer to this architecture as TEX2. A total of 8 samples were prepared with this surface architectural design, 4 at 45 PPI and 4 at 80 PPI. The micro-pillars display a conical shape, each with 2 - 8 μm in diameter at the base, and are $\approx$25 μm in height. They are coated somewhat uniformly on all ligament surfaces, as shown in Fig. 3.

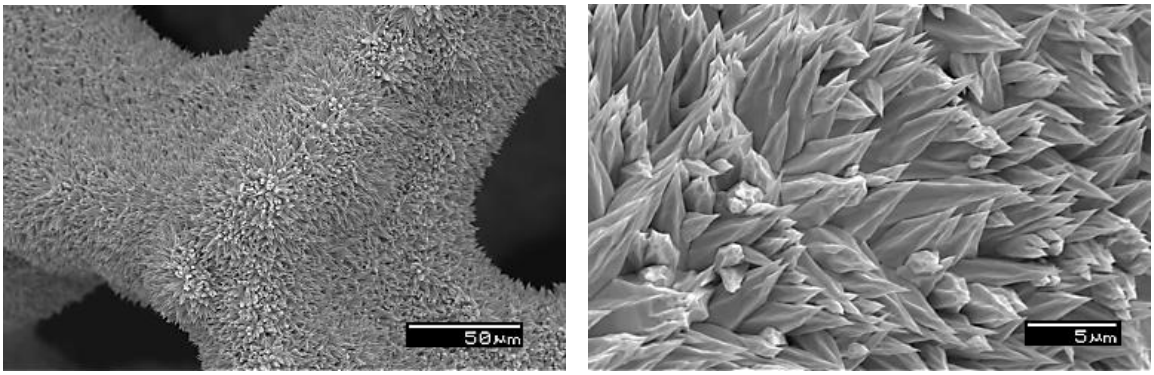

Figure 3: SEM images of the TEX2 surface architecture showing close-up of W-ligaments covered with Re micro-pillars directly atop of the ligaments.

The third set of samples were fabricated with one additional CVD step, where the rhenium micro-pillars were uniformly coated with an additional W layer, roughly 1μm in thickness. These samples, which we will refer to as TEX3, were all fabricated at 45 PPI. The tungsten coating is shown to reduce the sharpness of the underlying dendritic tips of the Re micro-pillars, leading to more tightly-packed nearly cylindrical micro-pillars that may play an effect in ion shielding. The SEM images of the tungsten coated pillars are shown in Fig. 4. The materials are manufactured by the CVD process, which is a versatile and relatively inexpensive method of molecular forming of materials and structures that are difficult to create by conventional powder processing and machining. The typical deposition rate for metals is 0.010 in/hr. Tungsten is deposited at just 550 °C through the hydrogen reduction of its hexafluoride under vacuum, flowed over a heated substrate in accordance with the following chemical reaction: $WF_6 + 3H_2 \longrightarrow W + 6HF$.

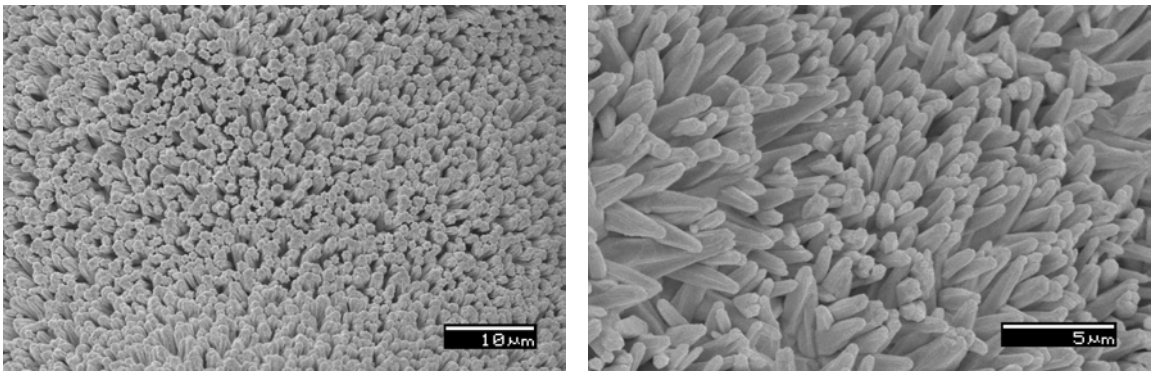

Figure 4: SEM images of the TEX3 surface architecture showing close-up of a W-ligament covered with W-coated Re micro-pillars directly atop of the ligaments.

2.2. Task 2: Multiscale Modeling of Plasma Interaction with Complex Surfaces

2.2.1. Coupled Nano/Micro Plasticity & Fracture

Micro-architectured materials exposed to pulsed thermal transients may accommodate the deformation caused by thermomechanical loads by either residual plasticity or fracture. Our working hypothesis is that the interplay between material parameters and the geometry of micro-architetured surfaces has an important role in determining which deformation mode takes place. We investigate this hypothesis by developing a novel unified computational method for plasticity and fracture at the mesoscale ($0.1 - 10\mu m$). The model will be used to optimize the geometry of micro-architectured refractory metals and ceramics exposed to plasma transients. The standard Discrete Dislocation Dynamics (DDD) method is the ideal tool to study plasticity at the mesoscale, because it allows a mechanism-based description of dislocations without resorting to expensive atomistic details.

The complex process of crack growth has proven itself difficult to model. It is highly dependent on several factors including the geometry, loading conditions, and material properties. Several efforts have been made to model crack propagation, however the singular elastic field at the crack tip still poses a challenge for FEM-based fracture models. Previous methods such as the Element Erosion and Inter-element Separation techniques are disadvantaged by their high degree of mesh dependence [2]. More recent developments such as the eXtended Finite Element Method (XFEM) display a decreased mesh-sensitivity. However, it faces difficulties when considering small-scale cracking and still requires knowledge of the crack location relative to the mesh so that the appropriate nodal shape functions can be enriched [3].

We have recently developed a mesh-independent fracture modeling technique called Discrete Crack Mechanics (DCM) whereby cracks are constructed using discrete Volterra dislocations [4]. The method takes advantage of the similarity between the elastic fields of cracks and dislocation pileups, an observation first made by Eshelby, Frank, and Nabarro [5]. DCM is based on the Parametric Discrete Dislocation (PDD) method developed to investigate the evolution of crystal dislocation ensembles [6–8]. Crack dislocations (referred to as such in order to distinguish them from crystal dislocations) are similarly represented with parametric space curves, and their mutual interactions are completely resolved as to give an accurate model of a crack. In this summary, the concept behind DCM is presented and a brief introduction to the development of the equation of motion governing crack growth is given. An example of stable crack growth is shown, highlighting the mesh-independence of the DCM method.

The Somigliana dislocation is described by a continuous Burgers vector distribution $\boldsymbol{B}(\boldsymbol{x}')$ representing a smooth displacement discontinuity in a material. Eshelby noted that an array of Volterra dislocation loops with Burgers vectors $\boldsymbol{b}$ arranged along a plane could be used to construct a stepped Somigliana dislocation [5]. A crack can be considered equivalent to a Somigliana dislocation, as it also introduces a continuous displacement discontinuity in a material that can be represented with a distributed Burgers vector $\boldsymbol{B}^c(\boldsymbol{x}')$. Borrowing from Eshelby's observation, DCM utilizes discrete Volterra dislocations with Burgers vectors $\boldsymbol{b}^c$ as building blocks to construct an approximation of $\boldsymbol{B}^c(\boldsymbol{x}')$:

$$\boldsymbol{B}^c(\boldsymbol{x}') \approx \sum_{i=1}^{N} \boldsymbol{b}_i^c H(\boldsymbol{x} - \boldsymbol{x}')$$

where N is the number of Volterra dislocations used in the crack representation.

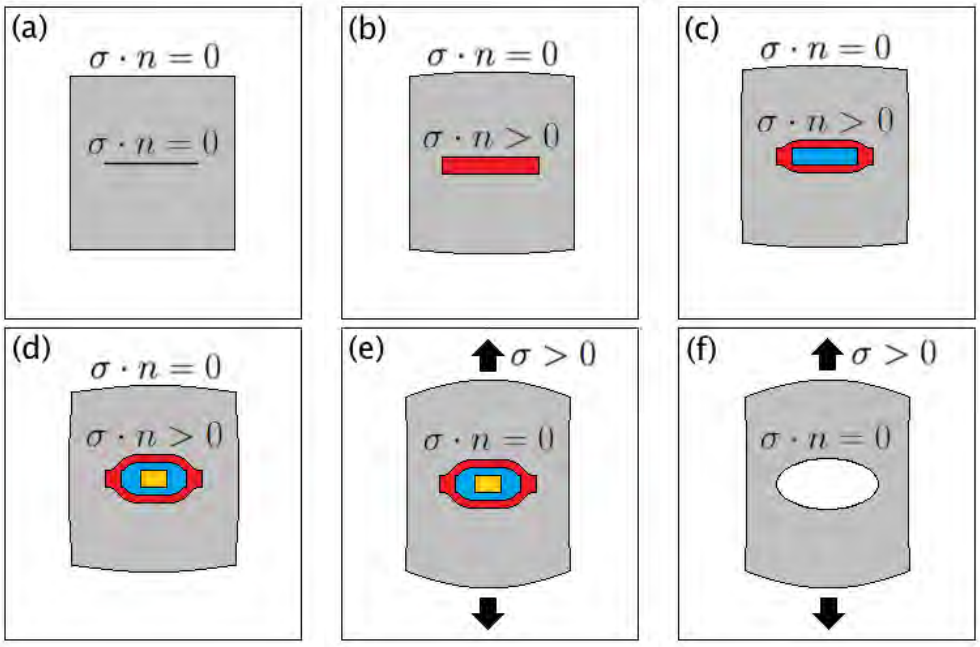

Figure 5: Volterra dislocation reconstruction of a crack

Figure 5 illustrates the concept of the dislocation-based crack approximation through a simple thought experiment. A cut is made in a stress-free material (grey) into which a rigid strip (red) with a thickness equal to $\boldsymbol{b}^c$ is inserted.

A cut is then made in the strip and another shorter strip (blue) with the same thickness is inserted. The process is repeated until a desired crack shape is achieved. At this point, the outer boundary remains traction-free while the tractions on the cut surfaces in the material are non-zero. Applying a load to the outer boundary that results in the tractions on the cut surfaces to vanish gives us the elastic fields of the crack under the same loading conditions. Note that the crack in this illustration is a mode-I crack, and the strips equivalent to edge dislocations. Mode-II cracks can also be represented using edge dislocations that are rotated, as shown in figure 6. Screw dislocations are used to model mode-III cracks.

The outer-most, or leading dislocation, in DCM is fixed and coincides with the shape of the crack. The inner, or trailing dislocations, are free to move according to the Peach-Koehler (PK) configurational force acting on them. The PK force is dependent on the stress field due to the interation between all of the dislocations σ_{ij}^D as well as the applied stress σ_{ij}^A. When the dislocations are contained within a finite body, the presence of a boundary results in an additional component, known as the image stress σ_{ij}^i, which is accounted for by a superposition-based method first numerically implemented by van der Giessen and Needleman [8]. First the elastic fields of the dislocation ensemble in an infinite domain are computed. The tractions on a virtual boundary that matches that of the finite body is then calculated. In a second problem, referred to henceforth as the correction problem, the tractions on the virtual boundary are applied in reverse to the finite body without dislocations. The final solution is obtained by summing the two problems.

The advantage of this procedure is that the dislocation fields can be computed analytically with relative ease, eliminating the singularities that pose numerical issues in traditional FEM-based

(a) (b) (c)

Figure 6: (a) Mode-I crack, (b) Mode-II crack, (c) Mode-III crack

crack models. This means that mesh refinement and re-meshing are not needed when modeling growing cracks. In the next section, a basic introduction to the governing equations for crack motion in DCM is presented.

Quasi-Static Crack Motion

Using the Principle of Maximum Entropy Production Rate (PMEP), the equations which govern the evolving crack system can be obtained. In the Parametric Dislocation Dynamics method [7, 9], dislocations are represented by uniform cubic or quintic Hermite splines which ensure continuity of the tangent vectors at points along the spline referred to as dislocation nodes. At each node α, Hermite-type degrees of freedom can be assigned: a position vector $\boldsymbol{p}_\alpha$ and a tangent vector $\boldsymbol{t}_\alpha$. A dislocation segment defined by the nodes (α, β) is then associated with a cubic spline $\boldsymbol{r}_\alpha^\beta$.

To implement the equation of motion, a fixed dislocation loop which defines the crack shape is placed in the crack location. A mobile dislocation is placed inside the fixed loop and the PK force is calculated at the dislocation nodes. The dislocation node velocity is then calculated. A pre-specified maximum displacement dx_{max} is then used in conjunction with the maximum nodal velocity to calculate a maximum simulation time step dt_{max}. The trailing dislocation nodes are then moved according to the product of their velocities and dt_{max}. Once the entire system is in equilibrium, a new dislocation is inserted and the process is repeated. Once the applied load is no longer sufficient to support any additional dislocations, the full crack representation is obtained. At this point, the stress intensity factor along the crack tip dislocation is calculated and if it exceeds the fracture toughness, the crack tip is advanced. In the next section, an example is given to demonstrate the ability of DCM to simulate stable crack growth.

DCM applied to fracture of Hall thrusters

We have recently applied the DCM method to analyze the fracture pattern that has been observed in the Hall thruster channel walls [10], as shown in Fig. 7. Using DCM, it was found that that under the operating conditions described in [10], the the coefficient of thermal expansion mismatch between the thruster BN wall and the graphite base can induce a sufficiently high tangential stress on the wall to nucleate a crack. The crack is under mode-I stress, and it is nucleated on the external surface of the BN wall. It was also found that, once nucleated, the crack grows towards the inner surface of the wall first, and it then climbs along the height of the BN wall. It was also shown that for the specific thermo-mechanical load, once nucleated the crack grows unstable.

2.2.2. High Temperature Dislocation Dynamics for Polycrystals

In order to increase the lifetime of structural materials exposed to thermal cycles in EP and PP systems, it is critical to understand whether plastic deformation increases in each cycle up to failure (plastic *ratcheting*), or it reaches a steady-state limit (plastic *shakedown*). Repetitive ther-

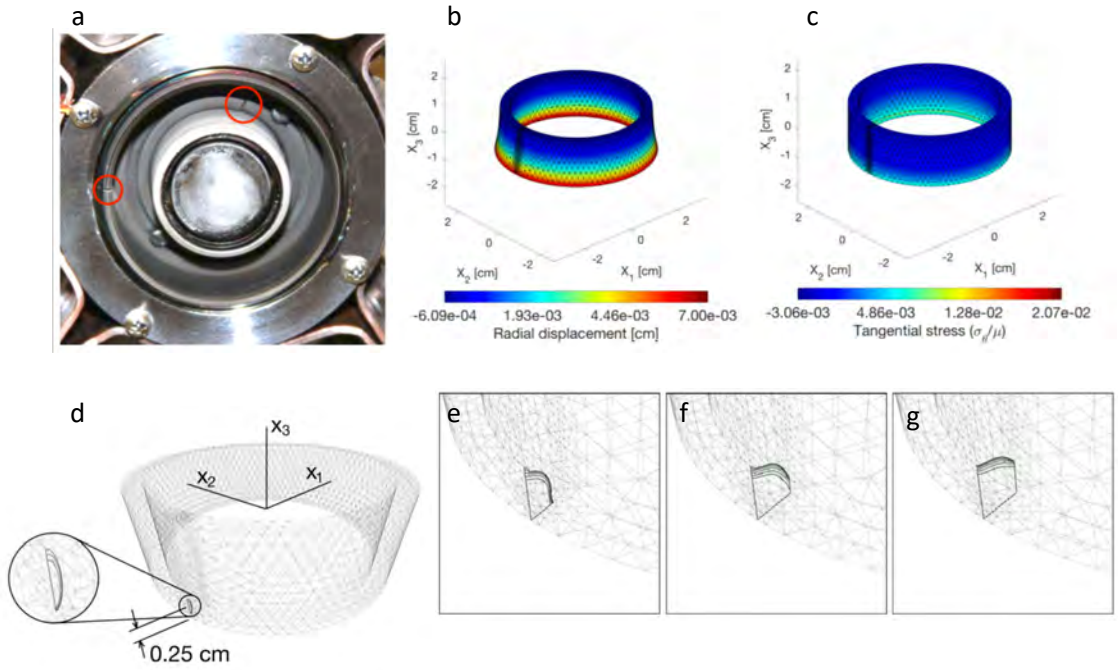

Figure 7: DCM method applied to fracture of Hall thruster channel walls. a) Crack pattern observed in [10]. b-c) Radial displacement and hoop stress due to the coefficient of thermal expansion mismatch. d-g)

mal stresses, when associated with incremental plastic deformation, result in thermomechanical fatigue failure. The objective of this research task is to understand which of the two deformation modes occurs in micro-architectured materials as a function of both external factors (e.g. sample geometry, mechanical and thermal loads) and material properties (e.g. dislocation microstructure, dislocation mobility). In either case, it is highly desirable to understand how cracks nucleate as a result of thermal cycling. In particular, we wish to investigate the role of plastic recovery assisted by high-temperature dislocation climb in determining creep-fatigue damage of micro-engineered features in plasma-facing surfaces, such as micro-pillars and micro- foam ligaments.

We began to study high temperature plastic deformation of micro-engineered materials by developing the High Temperature Dislocation Dynamics method (HTDD), where not only *glide* but also *climb* motion of dislocations is taken into account. Although two- and three-dimensional DD models incorporating climb have been proposed [11–16], the self-consistent implementation of climb in three-dimensional DD has been achieved using *ad-hoc* rules. The origin of the difficulty associated with climb can be traced back to the so called *virtual-work* formulation of the DD method, which offers no indication on how to couple the problem of dislocation motion and flux of point defects. On the other hand, in the *variational* formulation of the method which we have recently proposed [17], this difficulty is removed because physical constraints on dislocation motion are accounted for at the outset and as an intrinsic requirement of the Principle of Maximum Entropy Production rate (PMEP).

Polycrystal Dislocation Dynamics

Plasticity of polycrystalline materials is distinct from single crystal deformation, primarily as a consequence of dislocation pile-ups at GBs, which generate large stress concentrations in front of

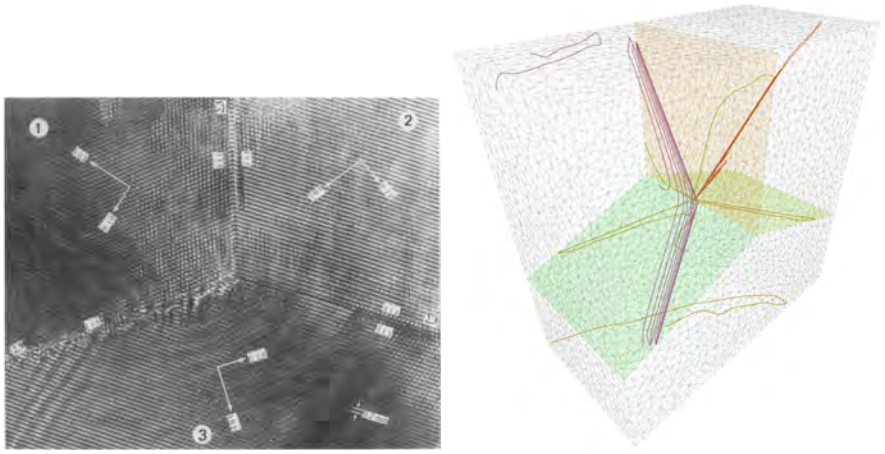

Figure 8: a) HRTEM image of a triple junction [23]. b) DD simulation in a triple crystal with same grain orientation.

the tip. The localized nature of the concentrated stress fields in pile-ups at GBs cannot be correctly mapped to a specific slip system in continuum-based crystal plasticity models [18]. On the other hand, full-fidelity Molecular Dynamics (MD) models of multi-dislocation pile-ups at the micro-scale would exceed current time and length scale capabilities. This situation establishes a strong need to develop "meso-scale" models of polycrystal plasticity, where the grain boundary structure and all dislocation reactions are resolved.

The primary objective of this research task was to develop a discrete physics-based method involving penetrable interfaces, GB sliding and a diverse selection of crystal interfaces. Another novel feature of the present implementation is the self-consistent constraint of dislocations to glide within the local crystallographic lattice in a physically realistic manner, including modeling inter-granular slip transmission and GB sliding, using DSCLs that are unique for the GB misorientation angle and structure. We also aim to demonstrate that computational modeling of dislocation and GB dynamics can be fruitfully used to study the discrete structure-dependent mechanical response of recent bi-crystal micropillar compression experiments [19]. The present implementation of DDD expands upon the framework developed by Ghoniem et al. [20], and recently by Po et al. [21]. The method provides an invaluable multi-scale bridge between atomistic and macroscopic crystal plasticity simulations, and is expected to enhance the future of design optimization for applications such as GB engineering. It is also ideally suited for heterophases, such as epitaxial thin films and precipitate-hardened alloys. The present work is a significant improvement and extension of a previously published 3D polycrystals DD study (see ref. [22]).

Implementation of polycrystal Dislocation Dynamics (polyDD)

At its core, the dislocation dynamics simulation method is a sequential solver for a discretized force-balance equation, taking as inputs the interactions between all dislocation loops in an ensemble. Dislocation loops are discretized into line elements and nodes to produce a discrete representation of nano-scale dislocation interactions without solving for individual atomic interactions. Increasingly sophisticated methods have been developed to reproduce short-range interactions such as junction formation, cross-slip, annihilation and superposition, both with singular and non-singular elastic field representations [7, 21]. The central premise is that dislocation-mediated components of plastic deformation can be determined by tracking the motion of the discretized dislocation network as determined by Peach-Koehler interactions. Mathematical details of the cur-

rent foundation of DDD can be found in references [7, 21], and thus will not be repeated here. When finite boundary conditions are desired, a mesh can be utilized to define the geometry of the simulation domain, and to define an elastic "correction problem" which satisfies both displacement and traction boundary conditions imposed on the simulation domain [24]. The reference single-crystal implementation is the open-source code within the "Mechanics of Defect Evolution Library" [25]. Compared to the single-crystal version, the polycrystalline extension of the DDD method developed here requires additional computation stages. These include:

1. An initialization stage where a 'multi-region' mesh is created, with each region corresponding to a grain. During the initialization stage, the code reads the necessary information to create the lattice structure within each grain, the lattice structure of the grain boundaries. Based on the type of grain-boundaries that are identified, their physical properties are looked up for subsequent use.
2. During the main simulation loop, a new computational phase is dedicated to performing discrete events at grain boundaries. The types of events which have been implemented are described in the following.

Early *in-situ* transmission electron microscopy (TEM) observations [26] have revealed three main mechanisms of lattice dislocation interactions with GBs. These are:

a) the absorption and immobilization of lattice dislocations into the grain boundary.

b) the dissociation of lattice dislocations into grain boundary dislocations with lattice vectors in the DSC lattice of the GB [27]. Subsequent motion of GB dislocations which are glissile on the GB plane give rise to Rachinger-type GB sliding [28].

c) the transfer of dislocations across GBs, with residual Burgers vector deposited on the GB. In turn, dislocation transfer can be *direct* or *indirect* [29]. In direct transmission the glide planes of the incoming and outgoing dislocations share a line on the GB plane. Indirect transmission involves either offset planes or incident planes [30, 31], and it may be mediated by GB dislocations [32, 33]. If transmission happens in the grain of the incoming dislocation, the process is referred to as *reflection*.

Here we model the energetics of heterogeneous nucleation and subsequent merging of arrays of half loops pinned by intrinsic GB dislocations. Consider a GB between grains 1 and 2, and assume that an dislocation line with Burgers vector $\boldsymbol{b}_1$ is deposited on the grain boundary from within grain 1. Let this be our reference state, and consider the process of nucleation and merging of an array of half dislocation loops on plane 2 of grain 2, each with with Burgers vector $\boldsymbol{b}_2$. These loops are pinned at the intrinsic GB dislocations, and therefore their diameter D is related to the intrinsic GB dislocation spacing d by the relation $D \sin\theta = d$, where θ is the angle formed by the direction of the intrinsic GB dislocations and the trace of the slip plane 2 on the GB plane. The transfer process is completed if the loop embryos travel a certain distance λ into grain 2, when they merge and unpin from the intrinsic grain boundary dislocations. It is reasonable to assume that for large D (e.g. for vanishing θ), the merging distance λ be some constant value λ_c which is independent of D. For D comparable or smaller than λ_c, however, the merging distance λ should be controlled by D, therefore we choose

$$\lambda = \frac{D\lambda_c}{D + \lambda_c} = \frac{d\lambda_c}{d + \lambda_c \sin\theta} \tag{1}$$

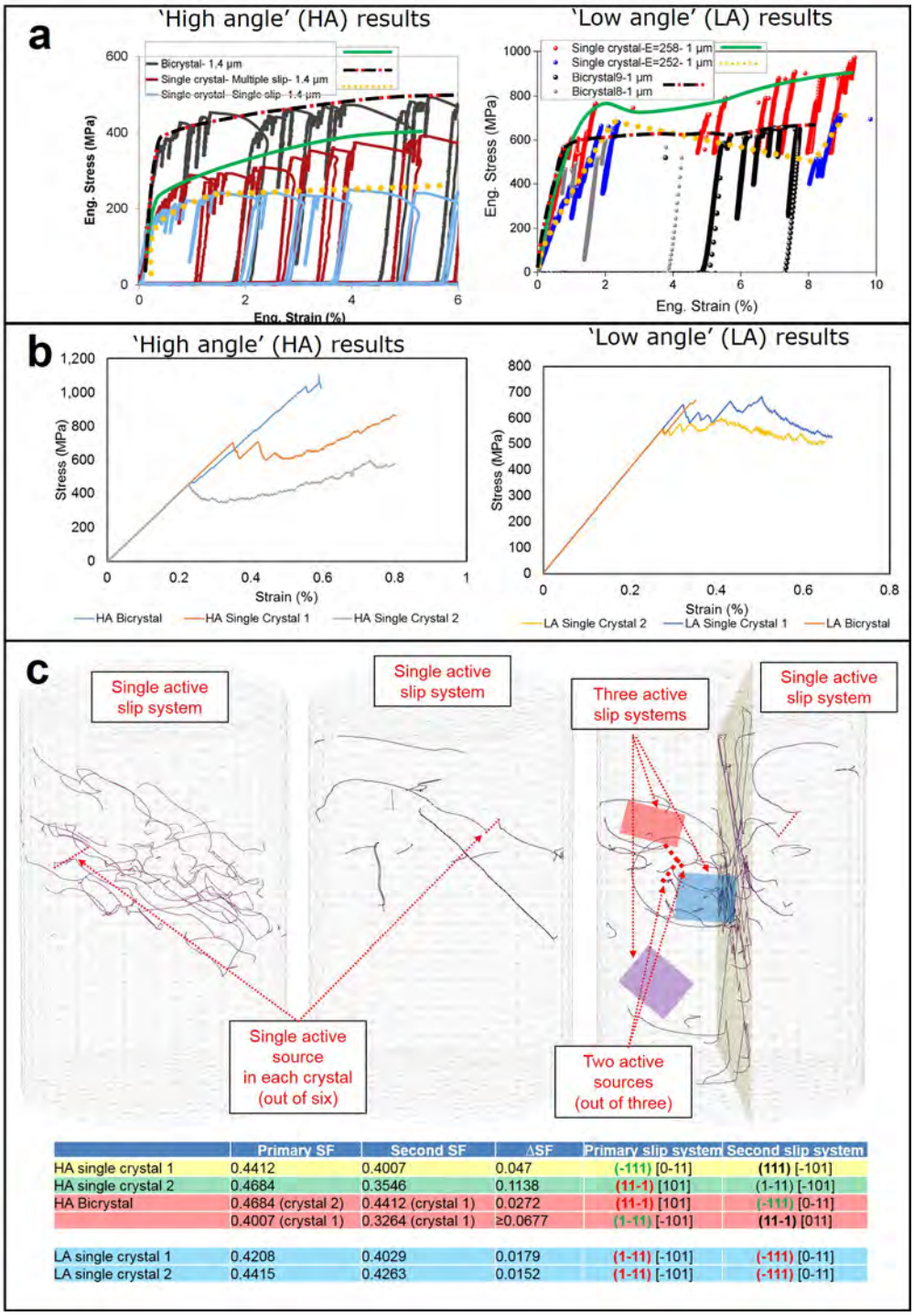

	Primary SF	Second SF	ΔSF	Primary slip system	Second slip system
HA single crystal 1	0.4412	0.4007	0.047	(-111) [0-11]	**(111)** [-101]
HA single crystal 2	0.4684	0.3546	0.1138	(11-1) [101]	(1-11) [-101]
HA Bicrystal	0.4684 (crystal 2)	0.4412 (crystal 1)	0.0272	(11-1) [101]	(-111) [0-11]
	0.4007 (crystal 1)	0.3264 (crystal 1)	≥0.0677	(1-11) [-101]	**(11-1)** [011]
LA single crystal 1	0.4208	0.4029	0.0179	(1-11) [-101]	(-111) [0-11]
LA single crystal 2	0.4415	0.4263	0.0152	(1-11) [-101]	(-111) [0-11]

r

Figure 9: Experimental benchmark of influence of GB structure (high vs low angle) and enabling slip-transmission. Quantitative results based on comparing bi-crystal stress-strain with the stress-strain results of two single crystal micropillars of identical crystallographic orientations: a) Experimental results (obtained from [19]). b) polycrystals DD simulation results, with impenetrable GBs.

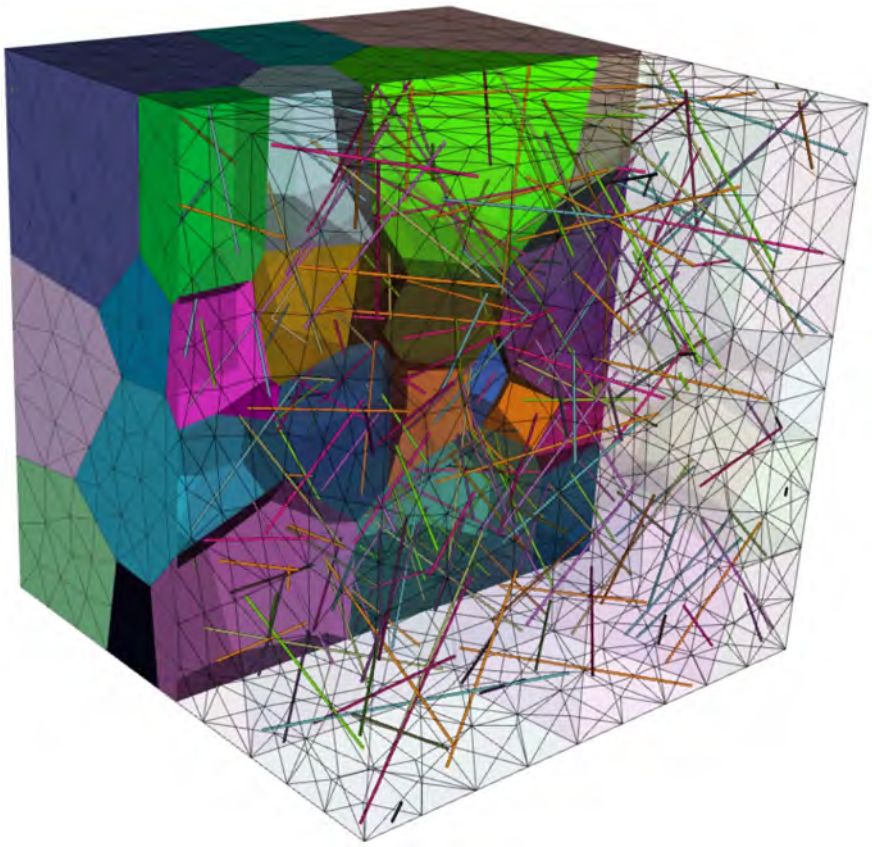

Figure 10: Example of DDD simulation in polycrystalline Cu containing 50 grains. Dislocation transmission criteria are specific to each grain boundary in the simulation.

Let us now compute the change in free energy per unit length Δg associated with the nucleation and merging of an array of loop embryos. We consider only the line tension contribution of the elastic energy, with a tension parameter $T = \alpha\mu/2$, where α is an adjustable and dimensionless parameter. Neglecting entropic effects we have:

$$\Delta g = \begin{cases} \alpha\mu b_2^2 - \tau_2 b_2 \lambda & \text{(indirect transfer)} \\ \frac{\alpha\mu}{2}\left(\|\boldsymbol{b}_1 - \boldsymbol{b}_2\|^2 + b_2^2 - b_1^2\right) - \tau_2 b_2 \lambda & \text{(direct transfer and GB nucleation)} \end{cases} \tag{2}$$

Note that, in the case of indirect transfer, the change in elastic energy per unit length corresponds to the creation of two new dislocation lines, one deposited on the GB as residual Burgers vector, and the other in grain 2. In the case of direct transfer, on the other hand, the change in elastic energy corresponds to a change in residual Burgers vector (from $\boldsymbol{b}_1$ to $\boldsymbol{b}_2 - \boldsymbol{b}_1$), plus the the creation of the new line element in grain 2. The array length L is found as the consecutive length over which $\Delta g < 0$. For each slip system in grain 2, we then compute the change in free energy $\Delta G = L\Delta g$. The slip system with the lowest ΔG is considered for a transfer event.

The model described so far was applied to DD simulations of low- and high-angle GB bicrystals under uniaxial loads, and compared to experiments, as summarized in Fig. 9. During the current reporting period, the polycrystal DD framework has been refined and optimized for large-scale simulations. Computer simulations of dislocation-plasticity in polycrystalline sample containing

up to 50 grains are now possible for the first time, as shown in Fig. 10. These simulations include both the fully-resolved mechanics of dislocation transmission across grain boundaries and grain boundary sliding, thus allowing a study of the temperature-dependence of bulk vs grain-boundary deformation in high-temperature materials. Current development also includes (a) integration between polycrystalline DDD and the DCM method described above and (b) implementation of dislocation climb within each grain.

2.2.3. Multiscale, Coupled Energy Transport & Deformation

We developed a multiphysics computational model in a finite element framework in order to investigate the synergistic effects of transient high heat loads and plasma ion implantation. The model utilizes the capabilities of the COMSOL multiphysics platform, in which a transient heat conduction analysis, coupled with a large deformation quasi-transient elastic structural mechanics analysis with contact elements along the grain boundaries are solved. We report here on several achievements in this area.

Mesoscale plasticity: the 2D Continuum Dislocation Dynamics method

We now discuss a modeling technique which is developed to study plasticity of single crystals and polycrystals at the length-scale of hundreds of μm to mm range. The model is based on the so-called continuum theory of dislocations (CDD), where dislocations are modeled as continuum density populations as opposed to discrete entities as in the discrete Dislocation Dynamics (DDD) method discussed above. The CDD method is here formulated in the large-deformation settings, and it is applied to a benchmark case of wedge indentation of fcc metals. The model is compared to the experimental measurements of lattice rotation and geometrically-necessary dislocation density (GNDs) performed using High Resolution EBSD by Kysar and co-workers [34, 35]. Indentation is as an important test for hard and brittle materials. In fact, due to its simplicity and the need for minimal specimen preparation, indentation has extensively been used as a mechanical test aimed at extracting bulk properties of metals from hardness measurements [36]. A notable example of this practice is Tabor's law relating to Vickers hardness and yield strength [37]. More recently, depth-sensing indentation has been used to extract other properties of bulk metals without the need to measure the residual imprint area [38].

A turning point in the history of indentation was the discovery of the ISE. For self-similar indenters (conical, Berkovich), hardness increases with decreasing indentation depth Nix and Gao rationalized this effect in terms of GND accumulating under the indenter [39]. This implies that indentation reveals fundamental properties of plastic deformation, such as self patterning and microstructure formation.

In order to model these phenomen, we consider a fcc crystal loaded by a wedge indenter along a $]110]$ direction, as shown in Fig. 11. Note that this is the same setup used in the experiments by Kysar. Under these conditions, it is well known that the slip systems act in pairs and result in three equivalent slip systems in the $[\bar{1}10]$-$[001]$ plane. On each slip system there two families of effective dislocations with opposite Burgers vector. The six effective dislocation densities are labeled ρ^s ($s = 1 \ldots 6$). The Nye tensor (GND tensor) corresponding to the six dislocation families is

$$\boldsymbol{\alpha} = \sum_s \rho^s \boldsymbol{b}^s \otimes \boldsymbol{\xi}^s \tag{3}$$

where $\boldsymbol{b}^s$ and ξ^s are the Burgers vector and the tangent vector for family s. The $\boldsymbol{\alpha}$ tensor can also be expressed in terms of the incompatibility of the plastic deformation. If assume a multiplicative

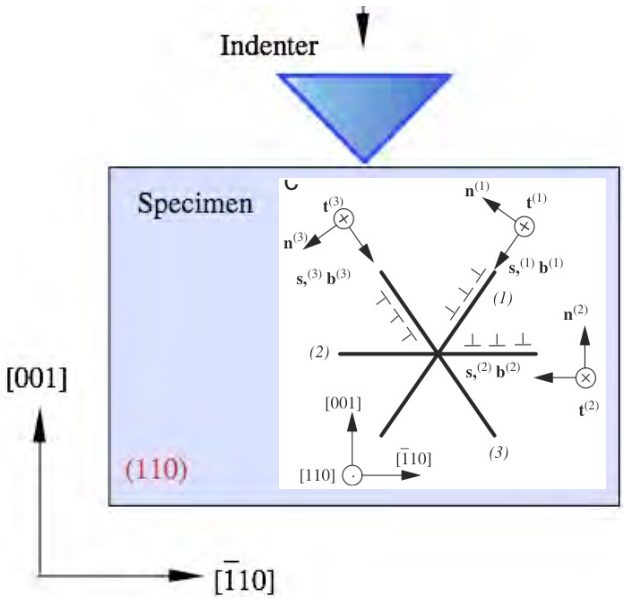

Figure 11: Experimental benchmark of influence of GB structure (high vs low angle) and enabling slip-transmission. Quantitative results based on comparing bi-crystal stress-strain with the stress-strain results of two single crystal micropillars of identical crystallographic orientations: a) Experimental results (obtained from [19]). b) polycrystals DD simulation results, with impenetrable GBs.

decomposition of the deformation gradient tensor as $\boldsymbol{F} = \boldsymbol{F}^E\boldsymbol{F}^P$, then compatibility arguments can be used to show that

$$\boldsymbol{\alpha} \equiv -\frac{1}{J^P}\left(\boldsymbol{F}^P \times \boldsymbol{\nabla}\right)\boldsymbol{F}^{PT} \tag{4}$$

Comparing the time rates of (3) and (4), one finds that the rate of plastic deformation is

$$\dot{\boldsymbol{F}}^P = \boldsymbol{L}^P\boldsymbol{F}^P \qquad\qquad L^p_{\gamma\delta} = \sum_s \tilde{b}^s_\gamma \tilde{\varrho}^s w^s n^s_\delta \tag{5}$$

where w^s is the dislocation velocity on the s-th slip system and $\boldsymbol{n}$ is its plane normal. Moreover, from the balance law of each dislocation density we have

$$\dot{\rho}^s = \boldsymbol{\nabla}\cdot(\rho^s\boldsymbol{w}^s) + p^s \tag{6}$$

The dislocation velocity is now found from thermodynamic considerations. The dissipation inequality consistent with the kinamatic framework discussed above reads:

$$\left(\tilde{M}_{\delta\gamma} - \delta_{\gamma\delta}\tilde{W}\right)\tilde{L}^P_{\gamma\delta} - \sum_s \frac{1}{J^P}\mu^s_{,K}J^s_K = T\tilde{\rho}\gamma \geq 0 \tag{7}$$

where $\boldsymbol{M}$ is the Mandel stress $M_{\alpha\gamma} = \frac{1}{J^P}F^P_{\alpha I}P_{Im}F^E_{m\gamma}$, and μ^s is the "chemical potential" of the s-th family of dislocations. Together with the constitutive relations

$$P_{mI} = J^P F^E_{m\alpha}\frac{\partial\tilde{W}}{\partial E^E_{\alpha\beta}}G^P_{I\beta} = J^P\left.\frac{\partial\tilde{W}}{\partial F_{mI}}\right|_{\boldsymbol{F}^P} = F_{mI}S_{IJ} \qquad\qquad \mu^s = J^p\frac{\partial\tilde{W}}{\partial\varrho^s} \tag{8}$$

the thermodynamics forces acting on the dislocation system are determined. The quantity γ is the rate of internal entropy production due to irreversible dissipative processes. For low dislocation speed compared to the speed of sound, dislocation dissipation can be considered proportional to the square of dislocation velocity, therefore we assume

$$T\tilde{\rho}\gamma = T\frac{1}{2}\sum_s B\tilde{\varrho}^s\tilde{w}^{s2} \tag{9}$$

Applying now the *principle of maximum dissipation*, we finally find the dislocation velocities to be:

$$\tilde{w}^s = \frac{b}{BT}\Big(\underbrace{\tilde{M}_{\delta\gamma}s^s_\gamma n^s_\delta}_{\tau^s_{\text{rss}}} - \underbrace{\mu^s_{,N}G^P_{N\gamma}s^s_\gamma/b}_{\tau^s_{\text{back}}}\Big) \tag{10}$$

We shall now consider a constitutive model where the microstructure energy $\tilde{W}_m$ depends explicitly only on the *total* scalar dislocation density

$$\varrho^T = \sum_r \varrho^r\,. \tag{11}$$

The microstructural energy reads:

$$\tilde{W} = \tilde{W}^{(1)}(E^T, T, \varrho^T(\varrho^1, \varrho^2, \ldots)) \tag{12}$$

A consequence of this assumption is that the chemical potential is the same for all scalar dislocation densities, in fact:

$$\mu^s = J^P\frac{\partial\tilde{W}_m}{\partial\varrho^s} = J^P\frac{\partial\tilde{W}_m}{\partial\varrho^T}\frac{\partial\varrho^T}{\partial\varrho^s} = J^P\frac{\partial\tilde{W}_m}{\partial\varrho^T}\,. \tag{13}$$

What remains to be fixed is the form of the free energy W. Several models are being considered. Here we discuss a simple model where the free energy is the sum of an elastic contribution plus a defect contribution of the form [40]

$$\tilde{W} = kG\ln\frac{1}{1-\varrho^T/\varrho^*} \tag{14}$$

where k and ϱ^* are material constants of the order of 10^{-4} and 10^{14} m^{-2}, respectively for aluminum. With this thermodynamic closure, the CDD model can be summarized in three coupled BVPs:

$$\text{macroscopic mechanical equilibrium: } \begin{cases} P_{Ij,I} = 0 & \text{in } \mathcal{B}_0 \\ P_{Ij}N_J = t_i & \text{on } \partial_N\mathcal{B}_0 \\ u_i = \overline{u}_i & \text{on } \partial_D\mathcal{B}_0 \end{cases} \tag{15}$$

$$\text{evolution of plastic deformation: } \begin{cases} \dot{F}^P_{\alpha I} = L^P_{\alpha\beta}F^P_{\beta I} & \text{in } \mathcal{B}_0\times[0,T] \\ F^P_{\alpha I}(\boldsymbol{X},0) = \delta_{\alpha I} & \text{on } \partial_N\mathcal{B}_0 \end{cases} \tag{16}$$

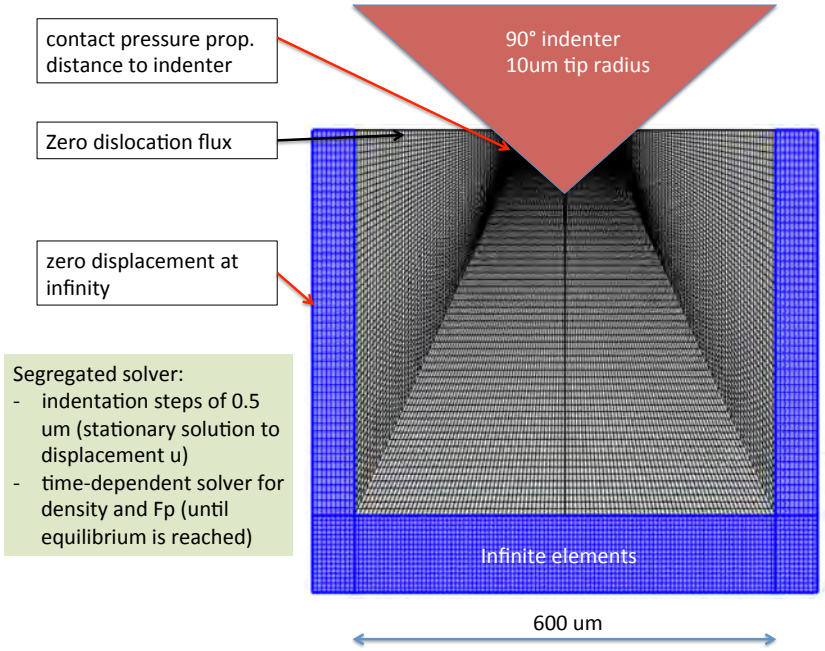

r

Figure 12: Details of the CDD model of indentation

$$\text{evolution of dislocation densities:} \quad \begin{cases} \dot{\varrho}^s = -\left(\varrho^s w_K^s\right)_{,K} + P^s & \text{in } \mathcal{B}_0 \times [0,T] \\ \varrho^s w_K^s N_K = 0 & \text{on } \partial_N \mathcal{B}_0^- \end{cases} \tag{17}$$

Next, the CDD model is compared to experimental micro-indentation measurements of lattice rotation and GND density [35]. Simulation details are shown in Fig. 12, while model results are shown below in Figs. 13, 14, 15, 16, and 17. Results show a very good qualitative and quantitative agreement between experiments and simulations. These results serve as an important validation of the plasticity model which will be applied to study the plasticity of Resilient Self-Healing Materials.

2.2.4. Surface Stability

In the sputtering process, the bombardment of energized particles on a material surface results in the ablation of surface atoms. This phenomenon can lead to roughening, as well as the development of various types of surface features driven by erosive instabilities [41]. Experimental evidence shows that ion sputtering can result in the formation of periodic surface ripples [42–46]. The nature of these ripples, including their wavelength, amplitude, and orientation depends on a number of factors, such as ion energy, flux, angle of incidence, substrate temperature, and material properties. Considerable research has been done by a number of groups to examine the effects of these various parameters on the surface features that develop under ion bombardment. It has been observed by [44] that the bombardment of a clean glass surface with an ion beam will produce a new surface morphology based on the incidence angle, θ of the ion beam. The observed

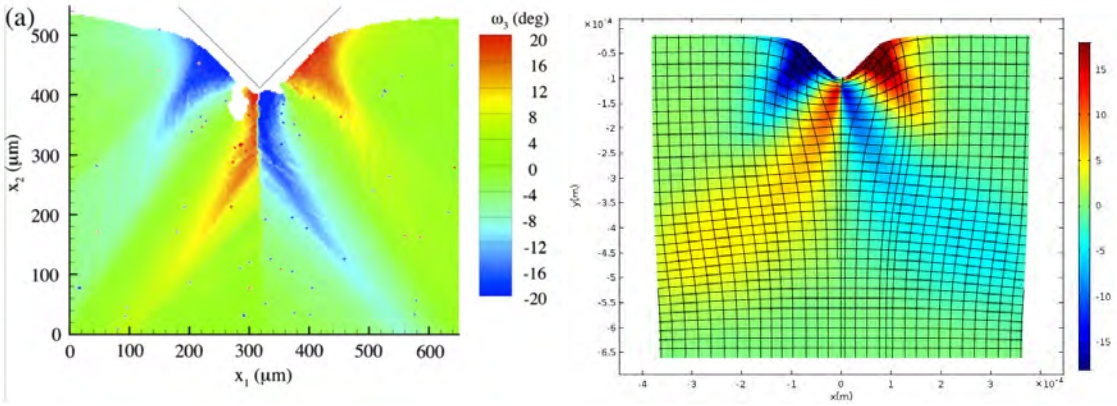

Figure 13: Lattice rotation: experimental (left) vs model (right)

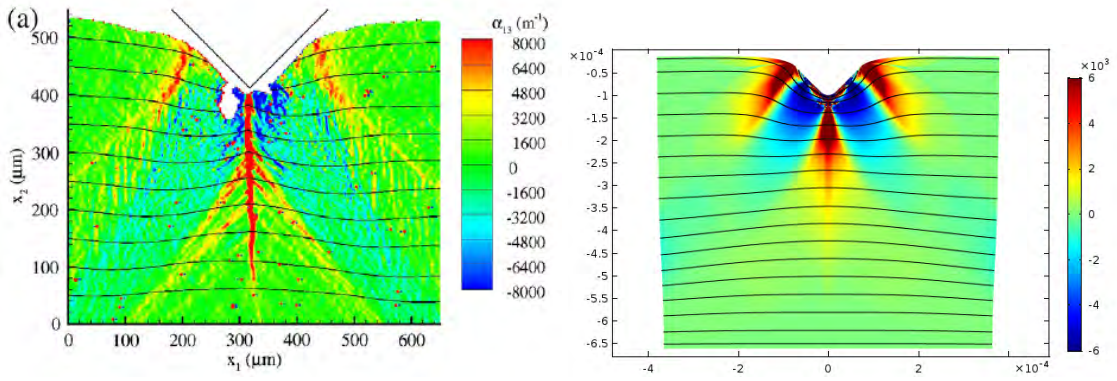

Figure 14: GND density component 13: experimental (left) vs model (right)

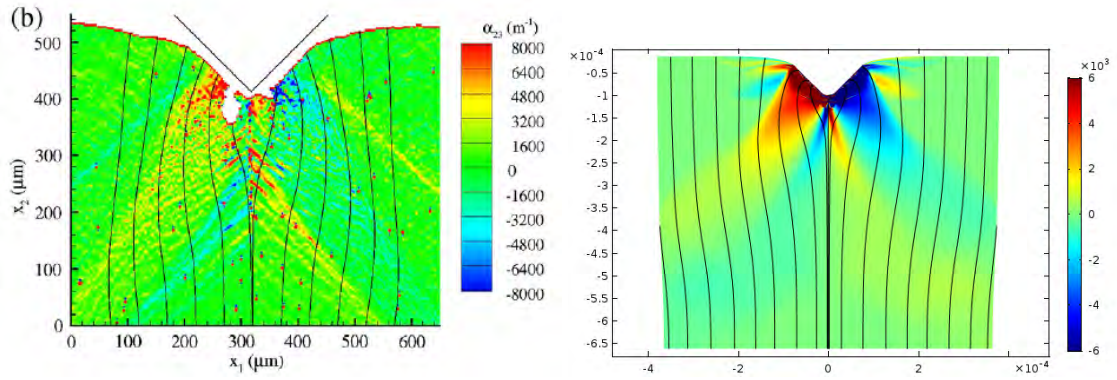

Figure 15: GND density component 23: experimental (left) vs model (right)

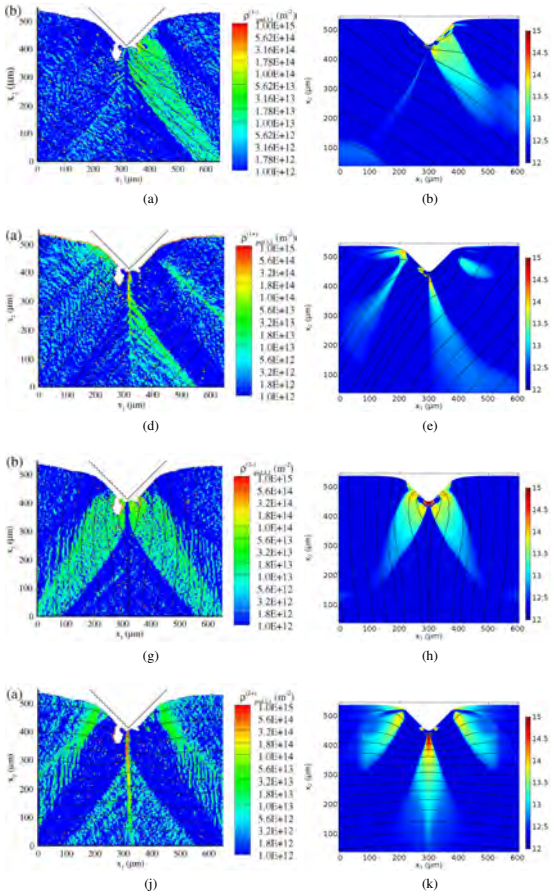

Figure 16: Density of dislocations on each slip system, experimental (left column) vs simulations (right column)

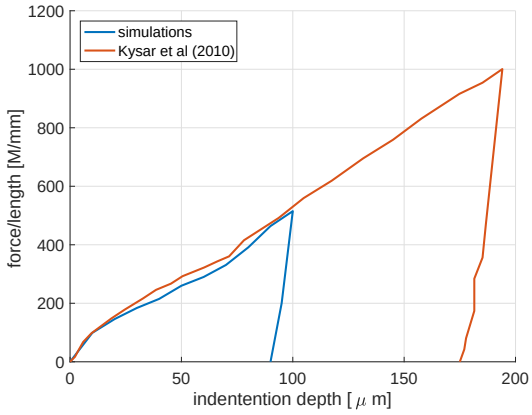

Figure 17: Indenter load vs depth, experiments and simulations

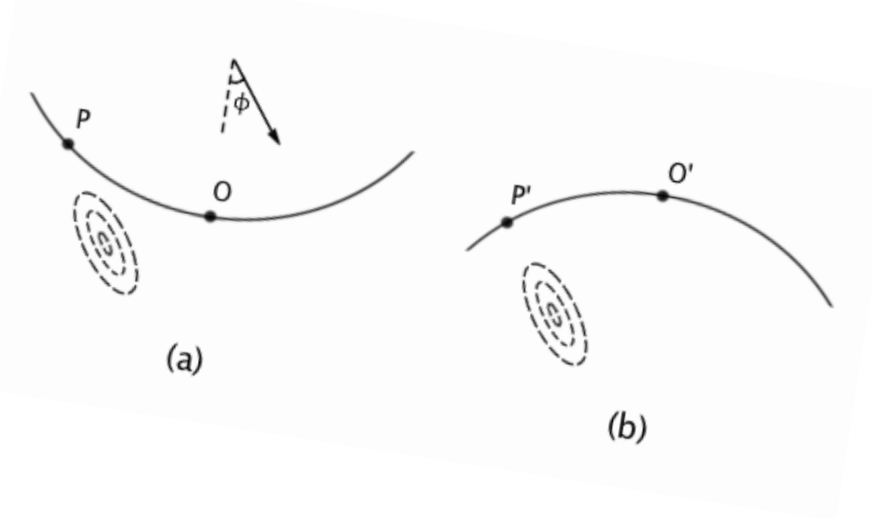

Figure 18: Illustration of the effect of the collision cascade on surface features of differing curvature

phenomena was the formation of ripple structures oriented perpendicular to the ion beam for incidence angles close to normal ($\theta = 0$), and parallel to the ion beam for incidence angles close to grazing. This experimental phenomenon is analogous to wavelike structures formed by wind in a sand bed. This natural occurrence comes about due to the fluid-like behavior of sand particles, which can be considered as an immiscible fluid with air, moving at very different speeds [46]. The boundary between them can develop wavelike structures through an unstable process. If a small sand pile or hollow randomly forms, it will disrupt the airflow around it. In the case of a pile, the wind is slowed and can not carry as much sand with it. This causes continuously more sand to be deposited, making the pile grow larger. Similarly, the wind is sped up in a hollow, which results in more sand to be swept away and the hollow to grow deeper. A theoretical approach to describing the sputtering process first came from [47], in which he associated the local sputtering yield to the deposited energy distribution of incoming ions.

When an obliquely-incident ion bombards the surface of a material, it initiates a collision cascade downstream, leading to the removal of atoms affected by the energy distribution. This process begins as the incoming ion embeds itself in the bulk of the material and transfers some of its energy to the atoms it comes in contact with. These atoms then may experience secondary collisions, producing the collision cascade. Some atoms will receive enough energy to be permanently displaced from their lattice sites. Those atoms close to the surface that receive enough energy to break their bonds will be sputtered. Figure 18 shows physically how the surface curvature affects the erosion. The collision cascade originating from an ion penetrating at P (P′) affects a point on the surface at O (O′). Here we see that the distance between the source of the collision cascade and O′ is much greater than it is to O. Therefore in the case of concave curvature, O will be more significantly affected than the case of convex curvature, O′, and more material will be removed [48].

The geometric effect of surface profiles on the erosion characteristics of ion-sputtered material surfaces offers great opportunity for further exploration. The development of nano- and micro-architectured surfaces introduces a new area of study, in which the effects of complex surface topography may alter the erosive development of a plasma-facing material surface. Practically speaking, understanding the nature of these textured geometries may offer the potential to design sputter-resistant surfaces. Surfaces of this variety may be characterized by a network of dendritic structures produced through a chemical vapor deposition (CVD) process. Experimental work has

shown that these nano-textured surfaces demonstrate a decrease in the net sputter rate at normal ion incidence compared to planar surfaces. The improved behavior of architectured dendritic surfaces may be attributed to several physical factors. Thermal stresses are reduced, resulting from the capability of fine surface features to withstand a greater level of distortion. Additionally, net sputtering erosion from the ion bombardment is minimized because of geometric trapping of redeposited atoms. Further, the higher surface area promotes better heat distribution, preventing localized overheating. While these material structures possess attributes that can improve the resilience and longevity of sputtered surfaces, there is much to be understood about their ability to withstand degradation according to traditional sputter erosion models. Therefore, it is desired to explore the effect of various surface structures on the erosive evolution of a material surface that is subjected to ion bombardment.

The primary focus of this task is to understand the relationship between initial architecture and pattern evolution of an ion-bombarded surface. We have made contributions to the understanding of surface stability as a result of plasma exposure during the current funding cycle. A theory has been formulated, and a special numerical method utilizing the FFFT technique has been developed. However, the forumlated theory does not take into account the influence of the surface stress state, which can be important in some EP & PP applications. The plan in this proposal is: (1) develop a unified theory that accounts for sputtering erosion, surface diffusion, sputter deposition and redeposition, and thermally-induced surface stress. The proposed approach is outlined below.

Since the mid seventies, a great deal of research showed that a flat surface is elastically unstable, and that any perturbation in the surface stress field can lead to surface roughening. This idea originated from the work of [49], who developed a theory that demonstrates how an initially planar surface of a uniaxially stressed solid will develop an instability in which any perturbation will become amplified. This result is attributed to the principle of minimum potential energy, in which the lower elastic energy of rippled surfaces cause an instability to form in the absence of a stabilizing mechanism [50]. It has been shown that the chemical potential is given by $\mu = \mu^0 + \Delta W V^0 + \gamma\kappa V^0$, where ΔW is the strain energy, κ is the mean curvature, V^0 is the atomic volume, and γ is the surface free energy. In the case of a material phase front, the existence of a ripples on the boundary of a liquid-solid interface, for example, will necessitate reducing the average elastic energy density of the solid profile. This occurs by growing the peaks, where the stress is lower, and increasing the depth of troughs, where higher stresses cause the density of elastic energy to be greater [51]. This behavior is described by first expressing the difference between chemical potentials of the interfacial phases:

$$\Delta\mu = \frac{1-\nu^2}{2E\rho_s}(\sigma_{tt} - \sigma_{nn})^2 + \frac{1}{\rho_s}\gamma\kappa + \frac{\Delta\rho}{\rho_s}g\zeta(x) \tag{18}$$

Here E is Young's modulus, ν is the poisson ratio, ρ_s is the density of the solid, and σ_{tt} and σ_{nn} are the stresses tangential and normal to the surface. The second term characterizes the stabilizing effect of surface stiffness, γ, as it relates to the surface curvature, κ. The last term is the contribution of gravity, g, where $\Delta\rho$ is the difference in density between the solid and liquid phases, and $\zeta(x)$ is the interface height at x. From the difference in the chemical potential, the normal velocity may be expressed as: $v_n = -\frac{1}{k}\Delta\mu$, where k is a rate constant with the dimension a velocity.

In Sigmund's theory of sputtering [47, 52], the average energy deposited by an ion within the bulk of a material is described by the Gaussian distribution. Surface geometries have a significant bearing on the consideration of Sigmund's model. Non-uniform profiles result in varying erosive

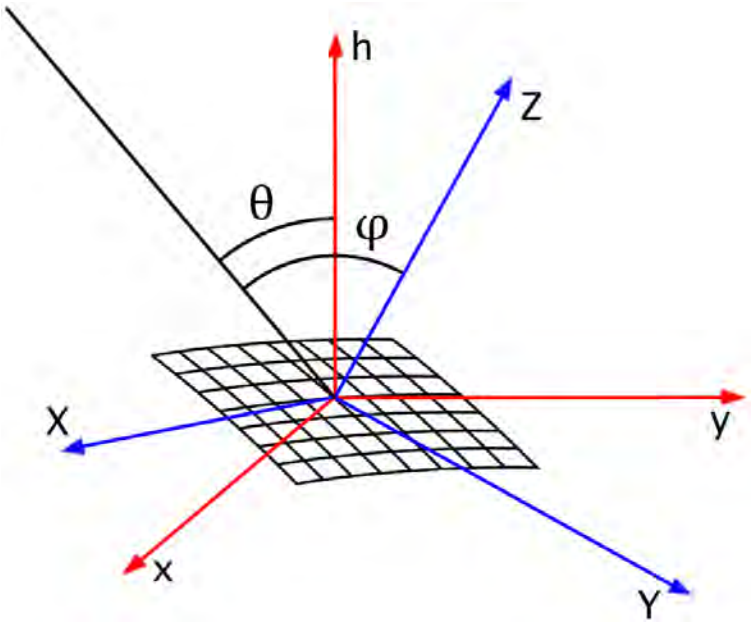

Figure 19: Illustration of the local reference frame (X, Y, Z) relative to the laboratory frame (x, y, h). θ is the angle between the h-axis and the ion trajectory, and φ is the angle between the local normal, Z, and the ion trajectory.

effects, depending on the distance of a surface point from the center of the collision cascade, where an impinging ion releases its energy distribution (Figure 18). Following Sigmund's theory [47], a theoretical model can be developed to describe the evolution of surface ripples on an ion-sputtered surface. This begins with the principle of conservation of energy, in which the energy deposited onto the surface by incoming ions is equivalent to the energy lost through the removal of material. $E_{in} = E_{out}$. The former is accounted for by taking the product of the ion flux $\Phi(\boldsymbol{r})$ with the average energy deposited per incoming ion. The quantity is then integrated over the region $\mathcal{R}$, where energy is deposited by incoming ions. This expression is equivalent to the flux of removed particles, J_{out}, multiplied by the surface binding energy, U_0. $\int_{\mathcal{R}} \boldsymbol{dr}\Phi(\boldsymbol{r})E(\boldsymbol{r}) = J_{out} \cdot U_0$. The particle flux may be expressed as the atomic density of ablated particles, n_{out}, multiplied by the local erosion velocity normal to the surface, v_n. Next, a transformation must be done between the local and laboratory coordinates (see Figure 19) to relate the normal velocity of erosion v_n to the velocity of erosion along the h axis [53]: $\frac{\partial h}{\partial t} = -v_n\sqrt{g}$. Here $g \equiv 1 + (\partial_x h)^2 + (\partial_y h)^2$, so that $\sqrt{g}$ is the magnitude of the vector normal to the surface. The negative sign is needed to reflect the rate at which the hight decreases, as v_n is simply the erosion velocity.

Additionally, the effect of surface diffusion acts as a stabilizing mechanism to the equation, and is joined into the theory by the inclusion of an additional term.

$$\frac{\partial h}{\partial t} = -v_n\sqrt{g} - K\nabla^4 h \tag{19}$$

The surface diffusion is temperature-induced, with coefficient K given by: $K = \frac{D_s\gamma\Omega^2\nu}{kT}$, where D_s is the surface diffusivity, γ is the surface free energy density, Ω is the atomic volume, ν is the number of atoms per unit volume, k is Boltzmann's constant, and T is the absolute temperature.

Self-deposition is be modeled for normal incidence ion bombardment by the addition of a non-linear term to the equation of motion [54]. We included this effect by modifying the governing equation for surface motion. The Kardar-Parisi-Zhang (KPZ) equation, presented to describe the profile of a growing interface [55], can be used for the time evolution of the surface height profile,

taking into account random height increases as well as local smoothing [56]. The anisotropic form of the KPZ equation was introduced by [57] to describe crystal growth by ion beams at different length scales. On the other hand, the Kuramoto-Sivashinsky (KS) equation is a deterministic, nonlinear equation originally developed to describe chemical turbulence [58] and laminar flame fronts [59]. In addition, a damping term may be added to produce the Damped Kuramoto-Sivashinsky (DKS) equation. The damping term results in smoothing of all spatial frequencies, thereby inhibiting kinetic roughening [60]. Its presence in the continuum equation for ion-bombarded surfaces has been used to account for redeposition of sputtered material [61]. The selected equation, following the theory outlined by the BH model [48], also possesses elements of the KPZ and KS equation forms. The resulting equation contains a second order term to account for geometric effects, a nonlinear term, and a fourth order stabilizing term to model temperature-induced surface diffusion. Additionally, redeposition is accounted for through the addition of a damping term. The final hybrid equation is expressed in the following way:

$$\frac{\partial h}{\partial t} = -v_0 - \alpha(h - h_A) - \frac{Fa}{2}\nabla^2 h - \frac{Fa_\alpha}{2}\left(\nabla h\right)^2 - K\nabla^4 h \tag{20}$$

Equation (20) is the time evolution equation of the surface in the laboratory frame. This expression has been simplified for normal ion incidence ($\theta = 0$), and by assuming an isotropic, or spherical energy distribution for the collision cascade (i.e. $\alpha = \beta$). Numerical simulations performed using the FFT numerical method produced a number of useful results that offer insight into the effects of various characteristics of the governing equation.

The numerical simulations of this study show that the initial surface architecture of a material under ion bombardment has been found to influence the long-term evolution under certain conditions related to the angle of incidence. Beginning with a surface described as a 4 by 4 grid of Gaussian-shaped "bumps", the surface was eroded at various incident angles for both the linear and nonlinear cases. The results showed a transition within a range of angles of incidence in which the initial surface architecture impacted the final morphology. This transition angle occurs between $\theta = 50°$ and $\theta = 55°$, and is an occurrence that has shown to be consistent over various initial architectures.

Figure 20 displays the contour plots of the surface profile before and after the transition point. It can be seen that prior to the transition at an angle of incidence of $\theta = 50°$, the evolved surface possesses a pattern that is unrelated to the initial Gaussian bump form for both the linear and nonlinear cases. After the transition, at an incident angle of $\theta = 55°$, the pattern in the x-direction shows a structure that correlates with the bumps of the initial profile, while in the y-direction the structure is consistent with the result prior to the transition. The difference between the linear and nonlinear results is demonstrated by the topography of the surface features. The nonlinearly evolved profile shows individual peaks, where the linear profile displays peaks that alternate in direction along rows following the y-axis.

To understand the main mechanisms of localized surface erosion, we start with Sigmund's theory of sputtering. The average energy deposited by an ion is given by:

$$E(r) = \frac{\epsilon}{(2\pi)^{3/2}\alpha\beta^2}\exp\left\{-\frac{Z'^2}{2\alpha^2} - \frac{X'^2 + Y'^2}{2\beta^2}\right\} \tag{21}$$

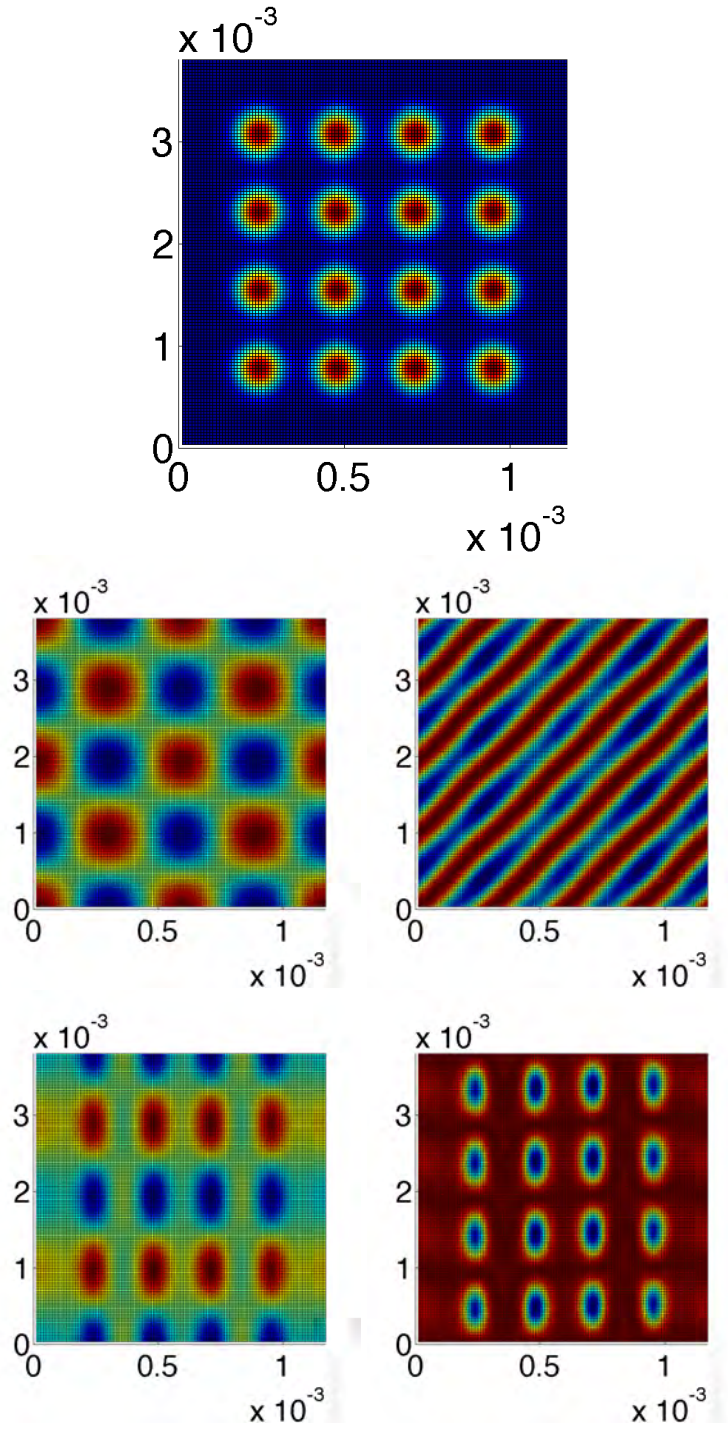

Figure 20: Comparison of evolved surfaces for initial profile (top row) of 4×4 gaussian bumps. Second row in Figure shows $\theta = 50^\circ$ and third row for $\theta = 55^\circ$.

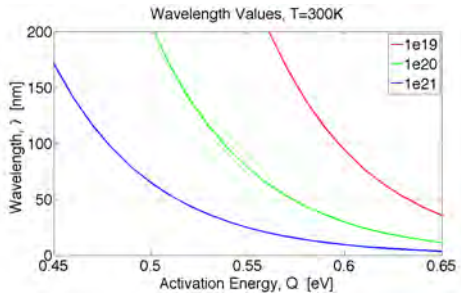

Figure 21: Stable wavelengths predicted at different activation energies for various ion fluxes

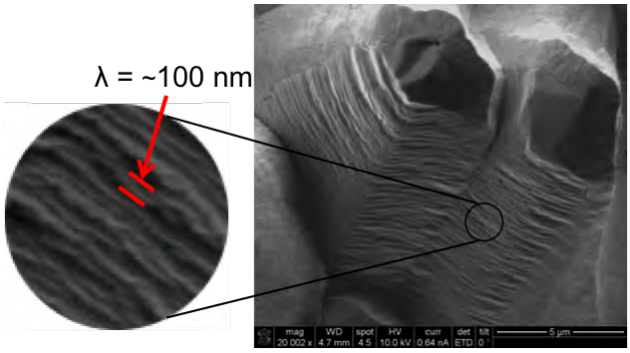

Figure 22: Ripples observed on dendrite faces after ion fluence exposure

This evaluates to:

$$v_n(\varphi, R) = \frac{J}{n} Y_0(\varphi) \left[\cos\varphi - \Gamma_X(\varphi) a/R_X - \Gamma_Y(\varphi) a/R_Y\right] \tag{22}$$

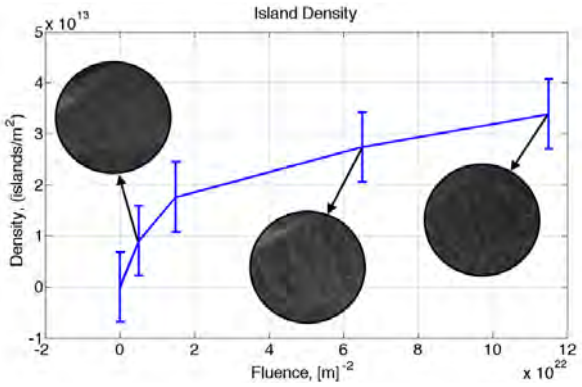

Figure 23: Density of islands across fluence exposures

Projecting the normal velocity along the vertical h-axis, and adding a term for surface diffusion results in the following height equation:

$$\frac{\partial h}{\partial t} = -v_0 - \frac{J\epsilon p a_\alpha^2 e^{-a_\alpha^2/2}}{2(2\pi)^{1/2}} \left[\frac{a}{2}\nabla^2\bar{h} + \frac{a_\alpha^2}{2}(\nabla\bar{h})^2\right] - K\nabla^4\bar{h} \tag{23}$$

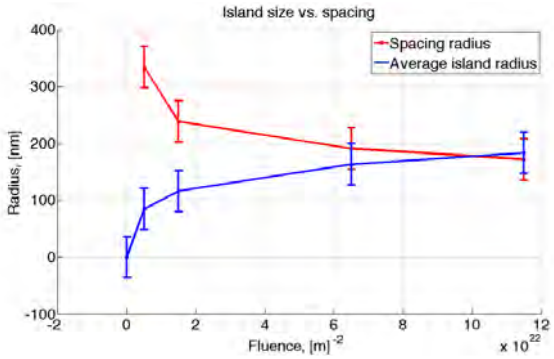

Figure 24: Island radius plotted against spacing radius

The results of liner stability analysis of the surface height equation are shown in Fig. 21, where the selected wavelength is dependent on the surface activation energy for atomic diffusion. We have found, using ab initio calculations, that the surface energy for diffusion in W will be quite small, on the order of 0.2-0.3 eV, as a result of a discovered surface crowding mechanism. Experimentally observed surface ripples are shown in Fig. 22.

2.2.5. Secondary Electron Emission From Complex Surfaces

We present results of secondary electron emission (SEE) yield calculations on flat tungsten surfaces subjected to plasma electrons. The idea behind these calculations is to define the source term fro *ray-tracing* Monte Carlo simulations of secondary electron emission yields in nanoarchitected surfaces. The coupling between these results and the ray-tracing Monte Carlo calculations will be discussed below. Here we use electron scattering theory implemented also in Monte Carlo (MC) setting to explore the dependence of SEE yields to incident beam energy and angle. Conventional MC approaches derived the average energy dissipation rate of a penetrating electron from Bethe's theory of stopping power on the basis of a continuous slowing-down approximation (CSDA) [62]. However, this treatment becomes inappropriate when an electron occasionally loses a large fraction of its energy in a single collision. To develop a more comprehensive Monte Carlo approach, incorporating differential cross sections for each of the inelastic events seems necessary [63–66]. The Monte Carlo method adopted in this work produces a stepwise simulation of the scattering of electrons in solids and their re-emission from the surface. The trajectory of the full cascade of electrons moving inside the material is simulated on the basis of theoretical probability distributions or empirical models.

Direct Simulation Monte Carlo Method

The present Monte Carlo calculation is based on the Mott's formula for elastic scattering [67–70], the Gryzinski [71–74] excitation function for core electrons, the Streitwolf excitation function [75] for conduction electrons, and the Ferrel excitation function [76, 77] for plasmon. Figure 25 shows schematically the Monte Carlo model of electron scattering in solids.

The scattering processes included in this model are briefly described in the following:

1. Elastic Scattering: electron-electron collisions resulting in no net energy loss, only directional changes. The most widely used theory that captures elastic scattering is that due to Mott and implemented with corrections by various authors [69, 70, 78]. This theory provides formulas for the total elastic scattering cross section, from which the scatetring angle and the

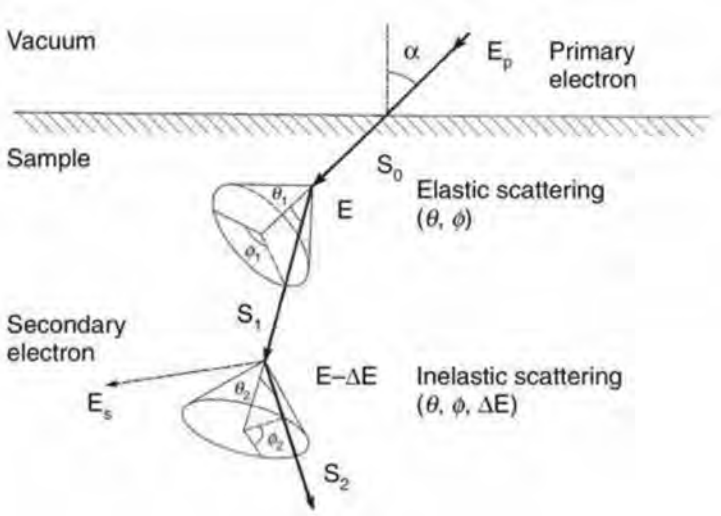

Figure 25: Scheme of the discrete model for Monte Carlo simulation of electron scattering. Figure reproduced from Ref. [63].

mean free path can be calculated.

2. Inelastic Scattering: It implies collisional energy loss and can in turn be subdivided into several elementary processes [79], each represented by a model that provides expressions for the scattering angle, cross section, and mean free path.
   (a) Core-shell Electron Excitation: Due to Gryzinski [71–74], the core-shell electron excitation model provides the energy loss due to interactions between primary electrons and core electrons.
   (b) Conduction Electron Excitation: It represents the energy loss due to interactions of electrons with conduction electrons [75].
   (c) Plasmon Excitation: The Coulomb field of the electron beam can perturb electrons of the solid at relatively long range as it passes through the foil. Beam electrons can excite oscillations, called plasmons, in the conduction electron "gas" that exists in a metallic sample with loosely bound outer-shell electrons. The theory used in our model is by Ferrel [76, 77, 80].

Experimental & Modeling Results of SEY Measurements in Metallic Foams

The basis that secondary emission had been shown to change with beam incident angle and sample topography laid the footing for the developing field. These data, in combination with an ambiguity regarding responsible physical phenomena led to subsequent work into improving yield prediction accuracy and differentiating electrons as a function of their total energy. Baroody drew upon Whittington's law which predicts the loss of primary energy, E, with penetration depth, x. A is a constant that differs for each material. Whiddington's law is written as

$$\frac{dE}{dx} = -\frac{A}{E(x)} \tag{24}$$

Baroody describes a set of assumptions that draw a normalized SEY curve independent of a solid sample's geometric or material parameters. Plotting the SEY relative to its maximum value, δ/δ_m

versus the primary energy relative to its value at peak yield, E_0/E_{0m} gives this curve. The equation is written as

$$\frac{\delta}{\delta_m} = \frac{1}{F(.92)} F\left(\frac{0.92E_0}{E_{0m}}\right) \tag{25}$$

where $F(r)$ is the function of the effective range of the secondaries for the specific material under investigation and is shown as

$$F\left(r\right) = e^{-r^2} \int_0^r e^{y^2} dy \tag{26}$$

In response to poor agreement between Baroody's theoretical curve and experimental data for metallic samples at beam energies greater than that at maximum yield, δ_m, Lye and Dekker improved upon this derivation with their "power law" formulation. This elementary theory of SE starts with a subtle but prevailing addition to Whiddington's law. Raising the penetration energy to a fitted power, n, results in SEY curves which more closely match experimental results. Following a similar derivation to Baroody, the updated expression for the universal reduced yield curve became

$$\frac{\delta}{\delta_m} = \frac{1}{G_n(r_m)} G\left(\frac{r_m E_0}{E_{0m}}\right) \tag{27}$$

where r_m is the value of r for which the maximum range of the secondaries occurs and is evaluated as

$$G_n\left(r\right) = e^{-r^{n+1}} \int_0^r e^{y^{n+1}} dy \tag{28}$$

Refinements in SEE analytics have been paired with decades of revising and augmenting direct measurements. One of the foundational experiments for polycrystalline copper was performed by Koshikawa and Shimizu. The team aimed an electron gun at a flat copper specimen inside of a vacuum chamber and gathered data using a spherical retarding-field analyzer. Using this apparatus, the team quantified SEY as a function of primary energy and beam incident angle. The former was tested between 0.5 and 10.0 keV and the latter from 0 to 70°. The two most relevant conclusions Koshikawa and Shimizu make are that polycrystalline copper has a δ = 1.43 at 500 eV and SEY increases monotonically with incident angle. Applying a polynomial trend line to δ vs. θ at this beam energy and increasing the order until the coefficient of determination is above 0.99, the resulting third order polynomial is found to be $\delta = 0.0058E_0^3 - 0.0461E_0^2 + 0.1453E_0 + 1.3129$. Bruining expressed the relationship of SEY and beam incident angle as

$$\ln \frac{\delta(\theta)}{\delta(0)} = A(1 - \cos(\theta)) \tag{29}$$

where A is a constant. Closeness of fit to this equation shall be discussed later in the paper.

It is important to note that SEY is sensitive to surface phenomena. This includes contaminants such as oxide layers, carbon films, and water content as well as differences in geometry at the nano- and microscale. This point has two implications, one theoretical and one practical. Respectfully, (1) in-depth material characterization is necessary to pinpoint SEY and (2) practically,

SEY has a range of values that should be expected. Davies and Dennison performed experiments quantifying the range of values to be expected after contaminating a sample with outgassed polytetrafluoroethylene, commonly referred to as Teflon. As testing continued in the ultrahigh vacuum environment, the sample experienced an approximate doubling in oxide presence. Electron stimulated absorption was found to result in a 30% decrease to SEY after a couple minutes of continuous electron bombardment. Further reduction in SEY, up to an additional 25% after several hours, can be attributed to the deposition of disordered carbon.

Monte Carlo algorithms have been developed to predict SEY for various materials including copper. Among other assumptions, Furman and Pivi incorporate in their model that (1) Secondary electrons are generated instantaneously when a primary electron hits a surface, (2) the energy of an emitted electron is no greater than the incident energy, and (3) emission angles of the secondary electrons are independent of incident angle as well as beam and emission energy. The team at Lawrence Berkeley National Laboratory is able to reproduce the experimental data for polycrystalline copper with a handful of fitting parameters. Extra attention is paid to SEY at incident energies below 20 eV since their model assumes only backscattered electrons are emitted at zero beam energy. This contrasts from a few previous analytical conclusions which say $\delta(0) \sim 0.07$. Furthermore, experimental data is understood to become increasingly sensitive as beam energy is lowered to only a few eV.

Unstable erosion of material surfaces, multipactor discharge, and electron cloud effects (ECE) have a direct impact on the lifetime and effectiveness of the previously mentioned applications. As discussed earlier, an overarching objective is thus to control SEY, with most uses having a penchant for δ minimization. Combining this target with previous evidence illustrating that rough or porous surfaces result in reduced SEY, it becomes clear that further quantification of δ with regard to such geometries could have far-reaching impacts. To close this knowledge gap, there must exist more cross-verified information regarding energy- and angular distributions of SEs for common materials such as elemental copper. This would allow spacecraft to more accurately model how SEE and charging are affected by re-absorption of low energy electrons in the presence of charge-induced electrostatic fields and ambient magnetic fields. Given this discussion, the study seeks to achieve the following objectives: (a) Experimentally quantify the change in SEY for foam copper relative to flat copper while varying beam energies and incident angles. (b) Predict SEY for copper foam and flat copper using Monte-Carlo simulations. (c) Compare empirical and computational results while identifying inherent differences. (d) Generalize findings to materials and microarchitectures other than flat and foam copper.

Experimental Approach

The two copper samples, one solid and the other porous, are examined thoroughly. Since SEY is sensitive to contaminants and surface texture, it is prudent to analyze the specimens with a variety of tools. Reticulation in the foam sample is illustrated using a high resolution CT scanner. SEM provides additional geometric information along with qualitative data on tilt and composition. Surface roughness and texture on the solid copper is quantified using AFM. EDS is used on both samples to quantify composition. Finally, XRD provides supplementary compositional information as well as plane prevalence and grain size. The two samples are shown in Figure 26.

A foam material can be simply described by its volume fraction, mean ligament thickness, and pore density. The values of these parameters, as given by the supplier and crosschecked using CT scans, are displayed in Table 1. While reticulated metals can be manufactured with a wide range of

Figure 26: Solid copper (left) and copper foam (right). Holes are created for mounting to sample holder.

foam parameters, the proposed experiment required small and dense features such that the 1 mm diameter electron beam would always be incident on a representative ligament cluster. On the other side of the scale, these features need to also be large enough for the characterization equipment to be resolute on individual ligaments.

Attribute	Symbol	Unit	Copper Foam
Volume Fraction	VF	-	4.6%
Mean Ligament Thickness	LT_m	μm	45
Pore Density	ρ_p	PPI	100

Table 1: Copper foam parameters.

Given the complex geometry of reticulated structures, computed tomography helps with visualization and analysis by scanning high-resolution slices of the specimen and reconstructing it to create a three-dimensional rendering. CT slices were obtained using the GE Phoenix Nanotom M and combined computationally to create the images in Figure 27. The machine outputs 15 W of power from a nanofocus X-ray tube and resolves details down to 200 nm for optimally small and reflective samples. The examined piece of copper foam resulted in CT scans with 2 μm resolution; this is sufficiently detailed for individual ligaments to be presented with considerable detail.

Four length scales fully illustrate foam specimens. These include the general foam structure, a ligament cluster, a ligament root, and a single ligament. The actual length of each scale is a function of the foam parameters with the general foam structure mostly reliant on pore density. In this instance, the 100 PPI specimen shows indicative homogeneity for a general foam structure in approximately 2.5 mm. A ligament cluster is characterized by a central pore with ligaments extending outwardly. There is clear loss of homogeneity, but a gain in radial symmetry. It follows that a ligament root is an intersection of ligaments. At this scale, a ligament's cross-sectional geometry can be ascertained. In the case of the copper foam specimen, each ligament has a cross-section comparable to a concave equilateral triangle. Figure 27-d displays a CT rendering of a single ligament. Severed from its root, this sample clearly shows hollowing along the ligament's length.

Complementary to CT renderings of the copper foam are analogous images using scanning electron microscopy (SEM). The model used is the NOVA 230 NanoSEM which employs a Schottky field emission gun. The four previously mentioned length scales are achieved with magnifications of 125x, 400x, 1000x, and 2,500x, respectively. An Everhart-Thornley detector, 5.0 spot size, and 10.0 kV accelerating voltage are consistent across the four images.

It is understood that brightness in SEM imagery indicates heavier elements, higher tilt angles, or both simultaneously. Since the copper foam sample is nearly void of microscale contaminants,

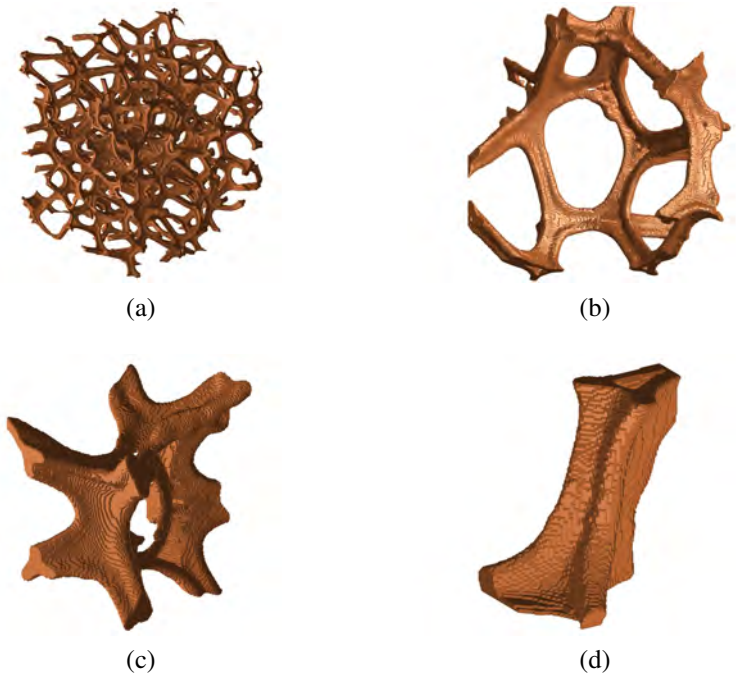

Figure 27: CT renderings of the copper foam's (a) general foam structure, (b) ligament cluster, (c) ligament root, and (d) a single ligament.

areas of higher brightness are solely indicative of tilt. Inspection of Figure 28-a validates the manufacturer's 100 PPI designation. To one significant figure, this suggests the copper foam exhibits four pores per millimeter. It follows that there are approximately four pores along the length of the 1 mm scale bar in the SEM image. The upper right SEM image shows a ligament cluster. Once again the central pore is clearly visible with ligaments extending outwardly. Figure 28-c zooms into the root visible at the center of Figure 28-b. At the ligament root length scale for this specimen, SEM provides resolution the CT scanner cannot. Dimples and microscale pores are identifiable, especially near the centerline of each ligament. These features, along with local surface roughness, are clearly visible at 2,500x magnification.

It is crucial to be aware of confounding variables and to minimize them where possible. Since this experiment aims to compare secondary electron yield between copper foam and solid copper, geometric and compositional differences between the specimens must be known. SEM images of the solid copper are provided in Figure 29. Note that the detector type, spot size, accelerating voltage, and magnifications are identical between these images and the corresponding ones in Figure 28. Rather than discussing general foam structure, ligament clusters, ligament roots, and single ligaments, respective magnifications give general texture, clusters of grains, individual grains, and a single grain. As with the copper foam, this specimen is nearly void of microscale contaminants. Thus, regions of greater brightness suggest locations with a tilt relative to neighboring darker areas. Figure 29-a shows the specimen has nearly homogeneous microstructure with grains oriented horizontally in this image. The grains, along with local ridges and valleys, are more pronounced in the higher magnification images.

While the copper foam's complex surface structure makes CT scans feasible and informative, the solid copper's relatively smooth and uniform surface makes it a strong candidate for

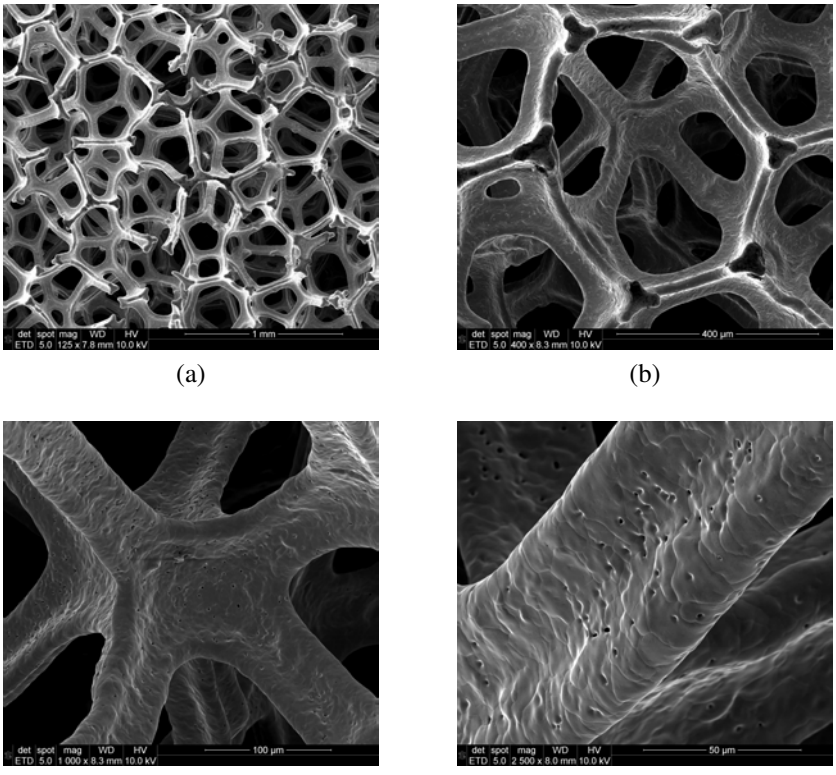

(a) (b)

(c) (d)

Figure 28: SEM images of the copper foam's (a) general foam structure, (b) ligament cluster, (c) ligament root, and (d) a single ligament.

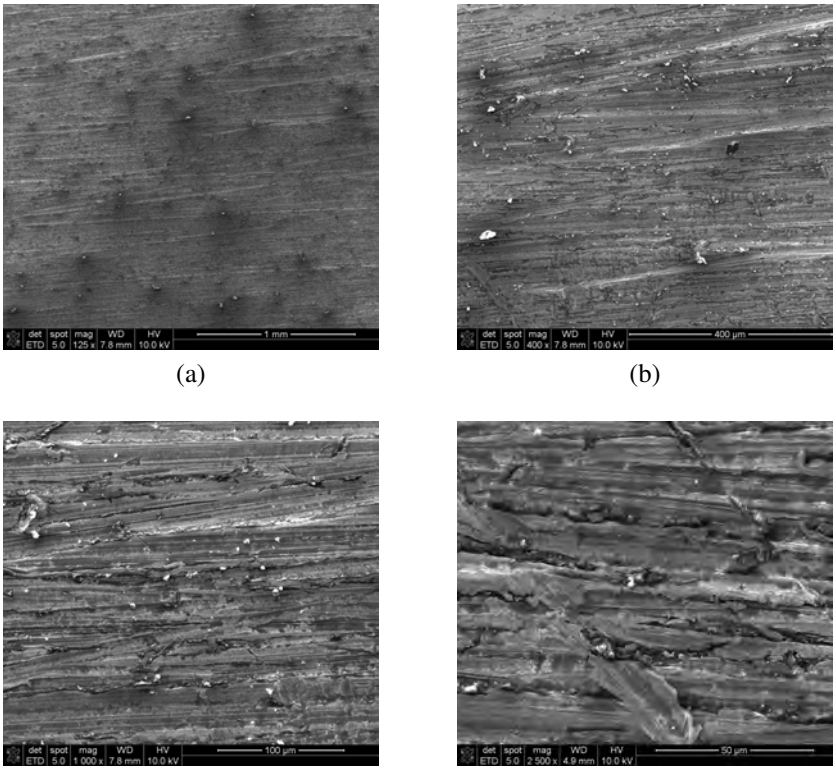

(a) (b)

(c) (d)

Figure 29: SEM images of the solid copper's (a) general texture, (b) cluster of grains, (c) individual grains, and (d) grain segments.

Atomic Force Microscopy (AFM). A piezoelectic cantilever is oscillated using an alternating voltage. Recording the amplitude of subsequent contractions and expansions allows the scanner to map a three-dimensional profile of the material's topography. Figure 30 displays a 40 μm by 34 μm section of the solid copper as measured by a Quesant Q-Scope 350. As evident from the legend, the height range in the segment is 2.4 μm. The majority of the segment, however, is substantially smoother. The median difference in height across the scanned piece is 1.07 μm. In terms of roughness standards, this puts the solid copper at an N7 ISO level.

Comparing Figure 30 and Figure 29-d, the AFM scan is a logical extension of the SEM image. The localized areas of peaking brightness in the SEM representation, and thus high tilt, exist in the AFM illustration as orange and brown crests. These towers stand approximately 1 μm above the median plane of the specimen. The valley that cuts diagonally across the scanned portion contains the grain boundary. While the width of the grain boundary is on the order of 2 nm, it is evident that the recession in which the boundary lies has a width of approximately 4 μm and a maximum depth about 1 μm below the median plane.

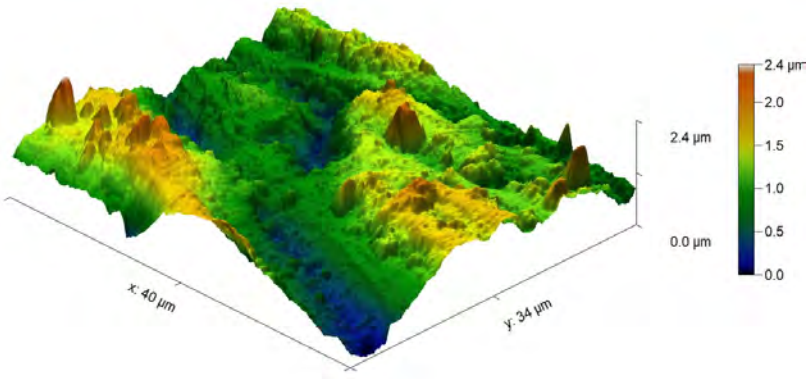

(a)

Figure 30: AFM measurements on solid copper.

CT, SEM, and AFM together provide a holistic picture of the geometric features of the two copper specimens, but only qualifiable information regarding composition. Energy-dispersive X-ray spectroscopy (EDS) helps bridge this gap. A spectrometer inside the NOVA 230 NanoSEM counts the discrete energies emitted from the specimens. This provides compositional information since these X-rays are characteristic, and thus point to particular emissions. Figure 31-a displays the EDS results for the solid copper sample and Figure 6b shows that for the copper foam specimen. The majority of X-rays measured from the are electrons returning to the L shell of copper. The other two peaks associated with the sample are identified as copper K-alpha and K-beta. While banal, these results do validate the specimen's composition and help to eradicate ambiguity regarding potential alloying, oxidation, and hydration. The copper foam EDS plot provides similar results.

The final form of material characterization in this experiment is X-ray diffraction (XRD). The method provides phase identification of crystalline materials and grain size. The instrument used is the BEDE D1 and is equipped with a 2.2 kW sealed tube X-ray generator, a goniometer with 0.16 inch resolution in θ and ω, and a high dynamic range scintillation detector. Similar to EDS, XRD plots show peaks of highest intensity according to characteristic energies. These energies, however, satisfy the Bragg Equation, whereby constructive interference reaches a local maximum. An X-ray diffractometer rotates the sample such that 2θ represents the angle between incident rays

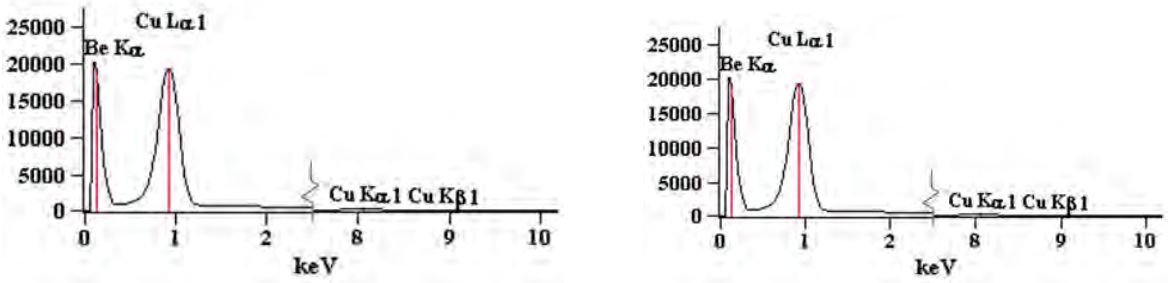

Figure 31: EDS measurements on (a) solid copper and (b) foam copper.

and the detector. This differs from ω which is the angle between incident rays and the sample surface. Figure 32 overlays the XRD scans for the two copper specimens. Five coinciding peaks are prominent in each data set. These represent the (111), (200), (220), (311), and (222) crystallographic planes of copper. This supports the EDS results which suggest negligible contaminants and impurities are present in the samples. Comparing the intensities of respective peaks.

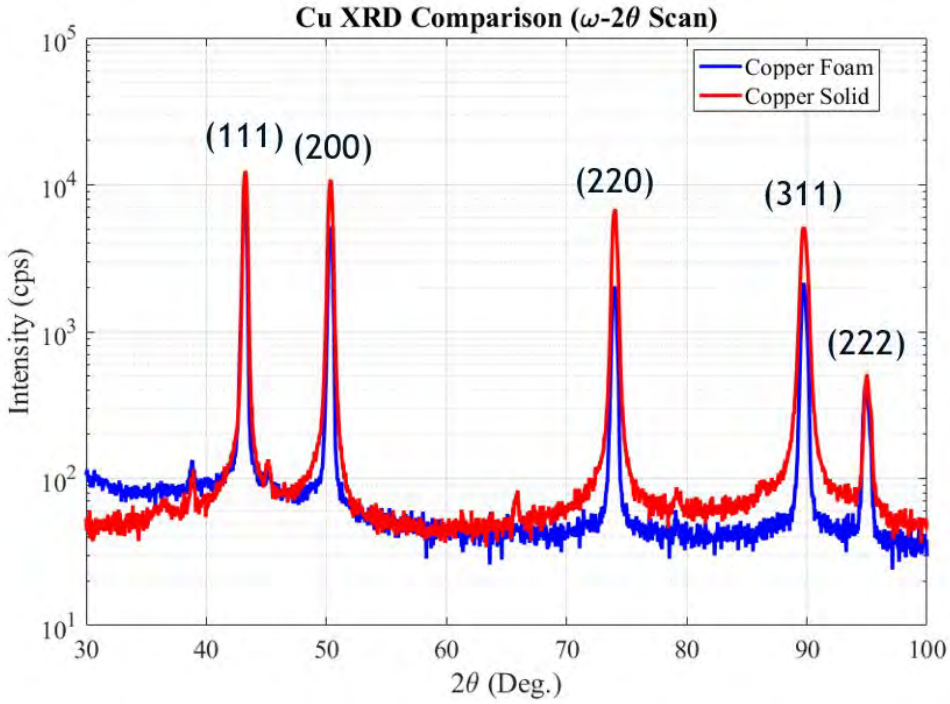

Figure 32: XRD measurements on both specimens.

The comprehensive review of material characterization allows one to conclude that the two specimens, copper foam and solid copper, differ by the existence of reticulation. That is, confounding variables such as subtle differences in composition are negligible. It was also discussed that the foam parameters in the reticulated sample are chosen to pair well with the secondary electron chamber. 6% volume fraction with 8 μm mean ligament thickness and 100 pores per inch maintain that the 1 mm diameter electron beam is sufficiently large relative to a ligament cluster.

The proceeding discussion delves into the components that comprise the experimental apparatus and the process by which SEY data is acquired from the two copper specimens.

Secondary electron yield is fundamentally the average number of emitted secondary electrons for a given incident electron. It follows that one must have a method to count or measure the number of electrons both entering and leaving the test specimen. Since electrons carry elementary charge, current, or the rate of charging, is a straightforward quantity that can be measured directly. Thus, SEY is the quotient of current produced from secondary electrons, I_{SE}, and current from primary electrons, I_p. Arbitrarily assigning SEY to δ, one can write this relation as $\delta = \frac{I_{SE}}{I_p}$. Since the number of secondary electrons is the difference in primary electrons and electrons remaining on the specimen, one can involve the sample current, I_s, and write $\delta = \frac{I_p - I_s}{I_p}$. This easily simplifies to the sample method's final expression

$$\delta = 1 - \frac{I_s}{I_p} \tag{30}$$

Rather than using the current of the sample, another technique of calculating SEY is by direct measurement of electrons given off as secondaries. Provided a strong enough voltage to collect the secondary electrons, this current, I_c, can be compared with the primary current to achieve the same result. This quotient, referred to as the collector method is written as

$$\delta = \frac{I_c}{I_p} \tag{31}$$

Both of these equations are experimentally valid for calculating SEY and the choice to use one over the other is based on the particular apparatus. It is previously mentioned that SEY is also a function of incident angle, θ. At increased values of θ, the shallow electron penetration depth favors the production of secondaries.

Apparatus

Discussion of the theory involved in measuring secondary electrons makes it clear that specimens need to receive primary electrons at a range of incident angles and at a variety of energies. This is achieved with a field-emission source, namely a thermionic electron emitter made of tungsten filament. The sample and emitter are located inside of a high vacuum chamber to maintain the specimen conditions across the test duration as well as to minimize interference from gas phase scattering while beam energy is low.

Sample current, I_s, is measured using wires that are electrically connected to the specimen via a conductive plate. A vacuum-jacketed port in the chamber allows the current to be read externally. This is identified in Figure 8 with the letter "S". Also inside the chamber is a Faraday cup which is used to collect the primary current, I_p. This is wired in a similar fashion to the sample current and measured at the adjacent external port. This connection point is designated with the letters "FC". Three components in the experimental apparatus control voltage potential: the sourcemeter, battery supply, and the grids. A potential of 72 V is found to be sufficiently strong to collect and accurately measure secondary electrons. Thus, the two batteries in series output 72 V and, for the appropriate setup, the sourcemeter is set to output the same potential.

The electron beam can be steady-state or pulsed. An oscilloscope makes the latter feasible and also provides a second method to record current measurements; the first method is direct

measurement from the sourcemeter. Both beam styles are viable using either the collector current or the sample current method. This gives rise to four ways of acquiring data, and thus four wiring schematics. The legend pairs a shape with a particular apparatus configuration. For instance, any wire with a circle is to be included when performing the experiment with a steady-state electron beam and the collector current method. Lastly, a circle is shown next to the sourcemeter and the label "0 V". This indicates that a sourcemeter is to read 0 V when using this setup. The other three schematics follow identical logic.

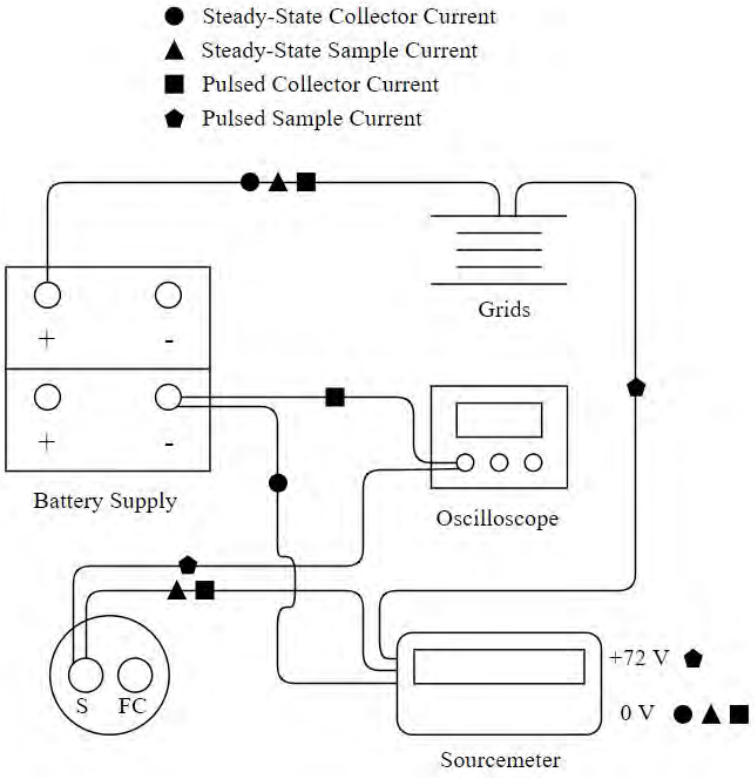

Figure 33: Wiring diagram with major apparatus components.

Procedure

One of the copper specimens is mounted onto the sample holder via nonconducting screws. The holder is then attached to a single-axis rod which articulates to test incident angles. Accuracy of θ is within 0.5°. And though the rod can rotate over 90°, the projected length of the electron beam onto the sample is sinusoidal with incident angle. This sets an upper limit of θ = 75°. The sample holder is placed inside the vacuum chamber, of which is brought to a pressure below 5e-6 Torr. At this point the electron gun is turned on and the beam is focused to a spot size of 1 mm. The apparatus is then configured according to one of the four wiring schematics shown in Figure 33. A particular beam energy, E_0, and incident angle, θ, are set and a data point can be recorded. E_0 and θ are updated until each combination of vectors $\theta = [0, 10, 30, 45, 60, 75]^\circ$ and $E_0 = [20, 80, 200, 400, 570]$ eV is complete. After the chamber is vented, the procedure repeats with the other copper sample.

Computational Approach

Solid copper is purposely chosen as one of the test specimens for its robust literature presence, and

thus a strong academic foundation to compare SEY results for reticulated copper. The profundity of the physics and underlying phenomena is further strengthened by comparing results against a computer simulation. The present model is based on the use of Mott's elastic scattering cross-section and Penn's dielectric function approach to electron inelastic scattering.

Elastic Scattering

Significant disparity in mass between electrons and atomic nuclei results in electron-atom collisions being acceptably approximated as perfectly elastic. A commonly used elastic scattering cross-section is that of Rutherford. Moreover, the analytical expression is readily adaptable to Monte Carlo calculations. This equation does have shortcomings, however. The screened Rutherford cross-section applies strictly to high-energy electrons and solids with low atomic number. For this reason, the relativistic partial wave expansion method (RPWEM) of the Mott scattering cross-section is the superior choice for modeling copper SEY from 20 eV to 570 eV. In the Mott theory [81], the differential elastic scattering cross section (DESCS) can be calculated as

$$\frac{d\sigma_{el}}{d\Omega} = |f(\theta)|^2 + |g(\theta)|^2$$

where $|f(\theta)|$ and $|g(\theta)|$ are the direct and indirect scattering amplitudes, respectively, given by

$$f(\theta) = \frac{1}{2iK}\sum_{l=0}^{\infty}\{(l+1)[\exp(2i\delta_l^+) - 1] + l[\exp(2i\delta_l^-) - 1]\}P_l(\cos\theta)$$

$$g(\theta) = \frac{1}{2iK}\sum_{l=1}^{\infty}[\exp(2i\delta_l^-) - \exp(2i\delta_l^+)]P_l^1(\cos\theta).$$

In these equations, K is the momentum of the electron, E the total energy, m the electron mass, c the speed of light, $P_l(\cos\theta)$ are the Legendre polynomials, and $P_l^1(\cos\theta)$ are the first-order associated Legendre polynomials:

$$P_l^1(x) = (1-x^2)^{1/2}\frac{dP_l(x)}{dx}.$$

The phase shifts $\delta_l^{\pm}$ can be computed by using the equation

$$\tan\delta_l^{\pm} = \frac{Kj_{l+1}(Kr) - j_l(Kr)[\xi\tan\phi_l^{\pm} + (1+l+k^{\pm})/r]}{Kn_{l+1}(Kr) - n_l(Kr)[\xi\tan\phi_l^{\pm} + (1+l+k^{\pm})/r]}$$

where

$$\xi = \frac{E+mc^2}{\hbar c}.$$

$k^+ = -l-1$, $k^- = l$, j_l are the regular spherical Bessel functions, n_l the irregular spherical Bessel functions and

$$\phi_l^{\pm} = \lim_{r\to\infty}\phi_l^{\pm}(r)$$

for which $\phi_l^{\pm}$ is the solution of Dirac's equation. With $V(r)$ being the electron-atom potential, this can be reduced, as shown by Lin, Sherman, and Percus [82] and by Bunyan and Schonfelder [83], to the first-order differential equation

$$\frac{d\phi_l^{\pm}(r)}{dr} = \frac{k^{\pm}}{r}\sin[2\phi_l^{\pm}(r)] - \frac{mc^2}{\hbar c}\cos[2\phi_l^{\pm}(r)] + \frac{E-V(r)}{\hbar c}$$

The atomic differential cross-sections for elastic scattering are extracted from the NIST Electron Elastic-Scattering Cross-Section Database and range from 0° to 180° for 16 incident energies between 50 eV and 600 eV (in increments of 10 eV from 50 to 100 eV and 50 eV from 100 eV to 600 eV, respectively) and put into a tabulated data file. The elastic differential cross-sections for energies and angles other than those in the table can be calculated by linear interpolation accurate to two decimal places. The total elastic scattering cross section for electron-molecule interaction can then be calculated by

$$\sigma_{el}(E) = \frac{\lambda_{el}^{-1}}{N} = 2\pi \int_0^{\pi} \frac{d\sigma_{el}(E,\vartheta)}{d\Omega} \sin\vartheta d\vartheta$$

where N is the number of molecules per unit volume in the target, and λ_{el} is the elastic mean free path. The angle of electron scattering at a certain step can be expressed by a random number

$$R = P_{el}(E,\theta) = \frac{1}{\sigma_{el}} \int_0^{\theta} \frac{d\sigma_{el}}{d\Omega} 2\pi \sin\vartheta d\vartheta.$$

The azimuthal angle, ϕ, can take on any value in the range 0 to 2π selected by a random number, R, uniformly distributed in that range.

$$\phi = 2\pi(R)$$

The total elastic scattering cross-section in turn defines elastic mean free path and is given by the formula

$$\lambda_{el} = \frac{1}{N\sigma_{el}} = \frac{A}{N_a \rho \sigma_{el}}$$

where N is the atomic number density. The path-length distribution is assumed to follow a Poisson-type law. The step length, Δs, is given by

$$\Delta s = -\lambda_{el} \log R$$

where R is a random number uniformly distributed in the range [0,1].

Inelastic Scattering

The energy loss function (ELF), which characterizes the inelastic scattering process, is defined as $\mathrm{Im}\left[-\frac{1}{\varepsilon(\mathbf{q},\Delta E)}\right]$ and is a function of momentum transfer, **q**, and energy loss, ΔE. The dielectric function $\varepsilon(\mathbf{q},\Delta E)$ in ELF reflects the response of a solid to an external electromagnetic perturbation. As it is impractical to determine the **q**-dependent ELF experimentally, Ritchie and Howie suggest deriving an approximate **q**-dependent ELF from the optical dielectric constants. By fitting the measured optical data into a finite sum of Drude-Lindhard model functions in the optical limit ($\mathbf{q} = 0$), one can extend the explicit formula to the required $\mathrm{Im}\left[-\frac{1}{\varepsilon(0,\Delta E)}\right]$ for finite **q**-values.

To perform this calculation the ELF of the material is parametrized in terms of an expansion of Drude-Lindhard-type oscillators at the optical limit with an N-term analytic form. This terms are obtained directly from the features observed in the reflection electron energy loss spectroscopy (REELS) spectrum:

$$\mathrm{Im}\left[-\frac{1}{\varepsilon(\mathbf{q},\Delta E)}\right] = \sum_{i=1}^{n} \frac{A_i \gamma_i \Delta E}{((\hbar\omega_{0i\mathbf{q}})^2 - \Delta E^2)^2 + \gamma_i^2 \Delta E^2} \times \theta(\Delta E - E_g),$$

where

$$\hbar\omega_{0i\mathbf{q}} = \hbar\omega_{0i} + \zeta\frac{\hbar^2\mathbf{q}^2}{2m}.$$

The $3n$ parameters A_i, γ_i, and $\hbar\omega_{0i\mathbf{q}}$, are the oscillator strength, the damping coefficient, and the excitation energy of the ith oscillator, respectively. The step function $\theta(\Delta E - E_g)$ simulates a band gap for the case of semiconductors and insulators such that $\theta(\Delta E - E_g) = 0$ if $\Delta E < E_g$ and $\theta(\Delta E - E_g) = 1$ if $\Delta E > E_g$. With the dependence of $\hbar\omega_{0i\mathbf{q}}$ on $\mathbf{q}$ being little understood. The parameter ζ value is related to the effective mass of the electrons; $\zeta = 1$ for for free electrons and $\zeta = 0$ for insulators with flat bands. A variety of pure elements and oxides have calculated fitting parameters of the ELF in an online database. [84]

An algorithm for determining the ELF($\mathbf{q}$,ΔE) from the ELF(0,ΔE) is required to continue computation. The model of Ashley (1988) [85] is one of approaches. According to Ashley, the electron differential inelastic scattering cross-section can be written as

$$\frac{d\sigma_{inel}(E,\Delta E)}{d\Delta E} = \frac{me^2}{2\pi\hbar^2 NE}\,\mathrm{Im}\left[-\frac{1}{\varepsilon(0,\Delta E)}\right]S\Big(\frac{\Delta E}{E}\Big)$$

where m is the electron mass, e the electron charge, N the number of molecules per unit volume in the target, E the electron energy, and ΔE the energy transfer.

$$S(x) = (1-x)\ln\frac{4}{x} - \frac{7}{4}x + x^{3/2} - \frac{33}{32}x^2$$

so the inelastic scattering cross-section $\sigma_{inel}(E)$ for the electron-electron interactions is given by

$$\begin{aligned}\sigma_{inel}(E) &= \int_{W_{min}}^{W_{max}} \frac{d\sigma_{inel}(E,\Delta E)}{d\Delta E}d\Delta E \\ &= \frac{\lambda_{inel}^{-1}}{N} = \frac{me^2}{2\pi\hbar^2 NE}\int_{W_{min}}^{W_{max}} \mathrm{Im}\left[-\frac{1}{\varepsilon(0,\Delta E)}\right]S\Big(\frac{\Delta E}{E}\Big)d\Delta E\end{aligned}$$

for which W_{min} is set to zero for conductors equated to the energy of band gap for semiconductors and insulating materials; $W_{max} = E/2$ is the maximum energy transfer.

$$\lambda_{inel}^{-1}(E) = \frac{me^2}{2\pi\hbar^2 E}\int_{W_{min}}^{W_{max}} \mathrm{Im}\left[-\frac{1}{\varepsilon(0,\Delta E)}\right]S\Big(\frac{\Delta E}{E}\Big)d\Delta E$$

$$\frac{\sigma_{inel}}{d\hbar\omega} = \frac{1}{N\pi a_0 E}\int_{q_-}^{q_+} \mathrm{Im}\left[-\frac{1}{\varepsilon(\hbar\omega,q)}\right]\frac{dq}{q}$$

With stopping power defined as $SP = -dE/ds$, the following equation is employed

$$-\frac{dE}{ds} = \frac{me^2}{\pi\hbar^2 E}\int_0^{W_{max}} \mathrm{Im}\left[-\frac{1}{\varepsilon(0,\Delta E)}\right]G\Big(\frac{\Delta E}{E}\Big)\Delta E d\Delta E$$

where the function $G(\frac{\Delta E}{E}) = G(x)$ can be approximated as

$$G(x) = \ln\frac{1.166}{x} - \frac{3}{4}x - \frac{x}{4}\ln\frac{4}{x} + \frac{1}{2}x^{3/2} - \frac{x^2}{16}\ln\frac{4}{x} - \frac{31}{48}x^2$$

To find the energy loss of an inelastic collision, W, of an incident electron with kinetic energy, E, it is necessary to calculate the function $P_{inel}(W, E)$. This value is accurate provided the fraction of electrons losing energy is less than or equal to W.

$$R = P_{inel}(W, E) = \frac{1}{\sigma_{inel}} \int_0^W \frac{d\sigma_{inel}}{d\Delta E} d\Delta E$$

for which R is a random number uniformly distributed in the range (0,1).

Monte Carlo Calculation

The probability of a given scattering event occurring is proportional to its cross-section. Thus, the cross-section specified for a given reaction is a proxy for asserting the probability that a given scattering process will occur. The stochastic process for multiple scattering events is assumed to follow Poisson statistics. If R is a random number uniformly distributed in the interval $(0, 1]$, the step length Δs is given by

$$\Delta s = -\lambda_T \ln R, \tag{32}$$

where λ_T is the electron mean free path and is given by

$$\frac{1}{\lambda_T} = \frac{1}{\lambda_{el}} + \frac{1}{\lambda_{inel}}. \tag{33}$$

The logic for determining elasticity of subsequent samples is defined as

$$\begin{aligned} &0 < R \leq \frac{1/\lambda_{el}}{1/\lambda_T} \implies \text{elastic scattering} \\ &\frac{1/\lambda_{el}}{1/\lambda_T} < R \leq 1 \Big(\equiv \frac{1/\lambda_{el} + 1/\lambda_{inel}}{1/\lambda_T} \Big) \implies \text{inelastic scattering} \end{aligned} \tag{34}$$

In this manner, events are sequentially sampled, executed, and followed as effective trajectories. These paths are tracked until an electron reaches the surface with an energy larger than the work function or until it is thermalized inside the material. Electrons that escape the surface are tallied and the net yields are computed as the ration of escaped electrons to the number of primary trajectories generated.

Results

Data presented describes the SEY for solid and foam copper as a function of beam energy and incident angle. These results are obtained experimentally per the aforementioned apparatus and procedure as well as computationally via the described Monte Carlo method. Comparing against existing literature for as-is solid copper δ collected using a normally-incident electron beam, it is evident per Figure 34 that the present experimental data aligns well. Together, these five sets of data are used to produce a 95% convergence interval, a 95% prediction interval, and a nonlinear regression curve. With the present data entirely within the prediction interval, the experimental data for solid copper is statistically valid. A range of δ are to be expected for as-is solid copper specimens due to subtle differences in surface charging, contaminants, and hydration. The 95% prediction interval approximates this range and provides evidence for a proposed data point's appropriateness in the existing collection of data. The nonlinear regression is defined using the polynomial model $\delta = (\theta_1 + \theta_2 E_0)/(1 + \theta_3 E_0 + \theta_4 E_0^2)$. Minimizing the residual gives the coefficients $\theta = [0.48, 0.15, 3.5\text{e-}3, 6.4\text{e-}6]$. The results shown in Figure 9 validate the control. Solid

copper δ has been experimentally calculated by several independent teams and is predominately shown for purposes of validation and direct comparison. Since the present data aligns well, novel results can be confidently presented.

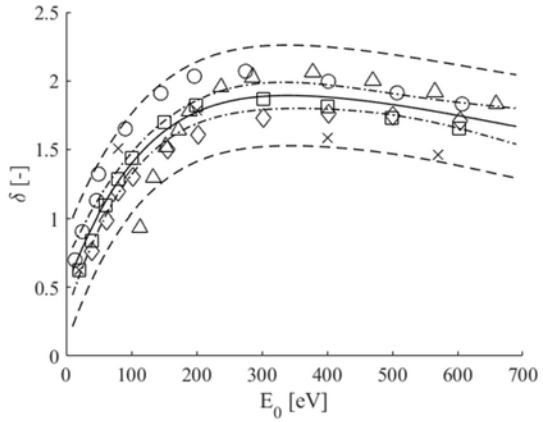

Figure 34: Comparison of solid copper and literature data.

The next set of results is for all normally-incident data. The comparisons that can be drawn are between experimental and computational data and between solid copper and copper foam data. Filled markers in Figure 35 represent experimentally-obtained data and the empty markers are from the computer simulations. The upper plot illustrates strong agreement between simulation and experiment for solid copper. Both curves quantify δ_m at approximately 1.8 and locate the peak at about $E_0 = 300$ eV. The copper foam simulation matches the shape of the respective experimental yield curve, but slightly under-predicts the quantity of secondaries to primaries. Reasons for this are discussed later. The copper foam reaches a δ_m of about 1.4 and occurs at about $E_0 = 500$ eV. This is a substantial and undeniably valuable reduction in secondary electron production. The yield saturates and remains nearly unchanged at energies higher than 400 eV. Minimal breakdown is found in the tested ranged. This contrasts from solid copper which gradually produces fewer secondaries for a given primary electron as energies are tested above E_{0m}.

Along with a range of beam energies, the experimental efforts and Monte Carlo simulation resulted in δ for a spectrum of incident angles. Maintaining the filled and empty marker distinction for experimental and computational results, respectively, Figure 36 displays the SEY curves for solid copper at $\theta = [0, 30, 45, 60, 75]^\circ$. The curves in Figure 36-a and 36-b both illustrate an increase in δ_m for an raise in incident angle. At $\theta = 75^\circ$ the solid copper plots report a δ_m of 2.5 and 2.2, respectively. This is a considerable increase in secondary electron production relative to the lower incident angles. Recall that normal incidence is calculated to have a δ_m of 1.8. Regarding differences between experimental and computational data, the simulations predict shallower breakdowns than the experiment calculates. Visually, SEY curves in Figure 36-a appear to diverge more noticeably at higher beam energies than the simulations suggest.

The separate SEY curves at different incident beam angles can be plotted on a third axis. Furthermore, nonlinear regression can be used once more to define a surface. This helps with visualization and interpolation.

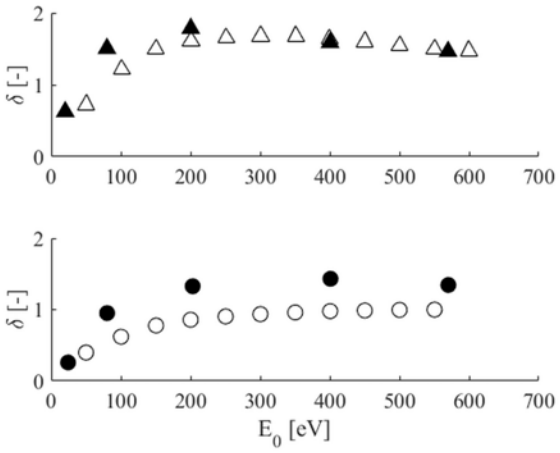

Figure 35: Comparison of solid copper and copper foam between empirical and computational results for normal incidence.

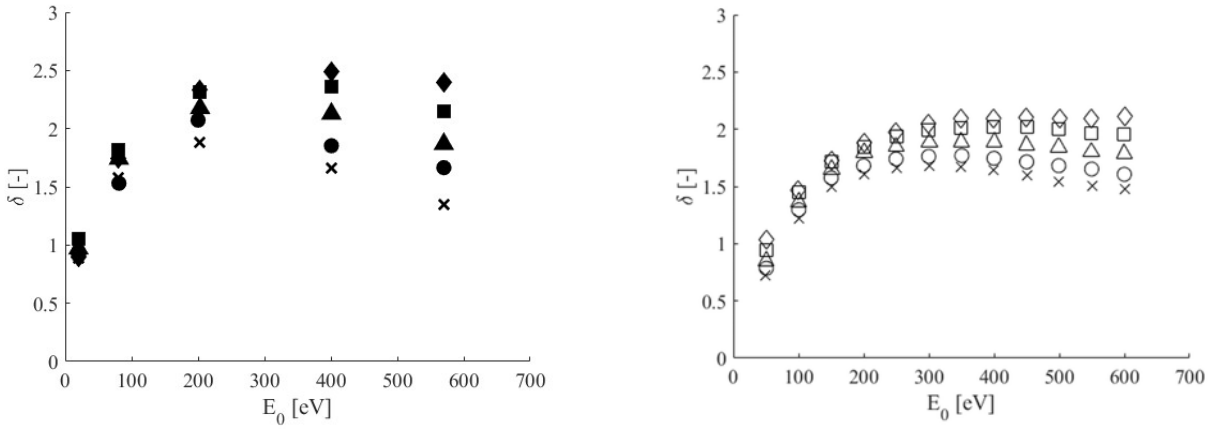

Figure 36: Solid copper data for different incident angles. (a) Experimental data (b) and computational data.

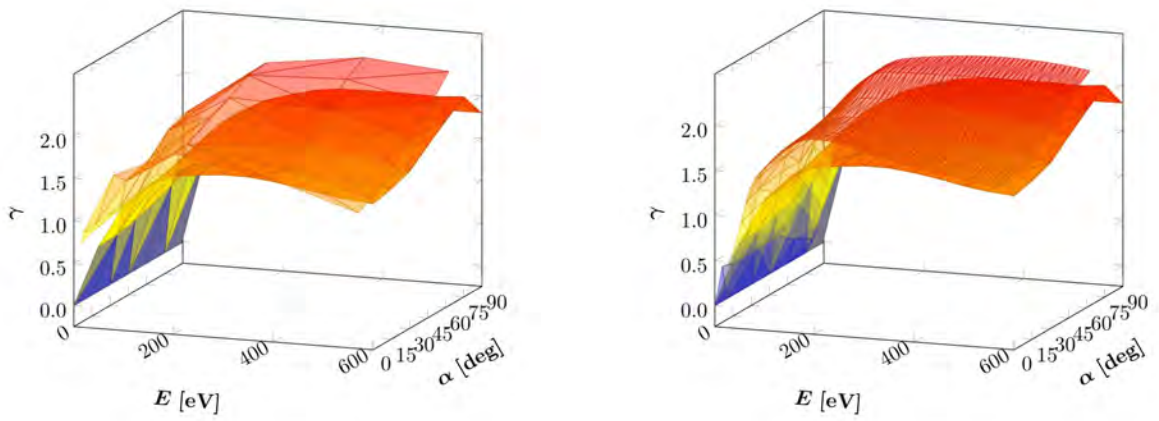

(a) (b)

Figure 37: (a) Solid copper SEY comparison between experimental and empirical results. (b) Copper foam SEY comparison between experimental and empirical results.

2.2.6. *Effective Sputtering and Redeposition*

Modeling sputtering redeposition on micro-architected surfaces involves considering the surface morphological changes over time. Thruster exhaust ions may erode (sputter) surfaces on which they impinge. In addition, this sputtered material may be re-deposited on other spacecraft surfaces. There, the deposited material may again be re-sputtered onto other surfaces. This re-sputtering process may be very important because, for certain geometries, it may influence the type and thickness of re-deposited material on a large percentage of the surface. To provide a consistent modeling of the sputtering and redeposition process of realistic surface geometries, we develop a Monte Carlo based ray tracing method and apply adaptive meshing techniques to account for surface morphological changes. To further boost the performance of the ray-tracing process, Bounding Volume Hierarchy (BVH) [86] suggests itself an ideal acceleration technique that uses a tree-based ”acceleration structure” that contains multiple hierarchically-arranged bounding boxes (bounding volumes) that encompass or surround different amounts of scene geometry or primitives. A key feature of this method is the Monte Carlo based pre-calculation of the position, direction, energy, and deposited energy of particles in each step for flat (ideal) surfaces. A set of bivariate fitting functions are generated from the pre-computed data using *symbolic regression* (SR) [87, 88], and serves as a sampling source for subsequent particle transport. This method is based on earlier work of Chang *et al.* [89, 90] and has been shown to reproduce full particle transport with a statistical accuracy of 3%. While updating the effective height of each triangular mesh element, sharp creases, edge, self-intersections, or triangle flips can occur. To address these issues, we develop a mesh-based solution to surface evolution to remesh the entire sample adaptively. Sputtering and redeposition are then updated self-consistently to give a realistic material evolution.

To model the dependence of sputtering yield and sputterants energy on ion energy and incidence angle, TRIM (the TRansport of Ions in Matter) is used, which is the core program included in the scientific software package SRIM (the Stopping and Range of Ions in Matter) [91] based on the work by Ziegler and Biersack on stopping theory. In SRIM, all ion-atom collisions receive a quantum mechanical treatment, and the stopping and range of ions can be calculated in the energy

range 10 eV–2 GeV. The calculations of the ion-atom screened Coulomb collisions use statistical algorithms to allow for jumps between calculated collisions before the collision results are averaged over the trajectory gap, and interactions between overlapping electron shells (electronic stopping) are included. For the particular purpose of calculating surface sputtering with TRIM, three material input parameters are of importance: the lattice displacement, surface binding and lattice binding energies. In the present calculation, the lattice displacement, surface binding and lattice binding energies are chosen as 25, 8.68 and 3 eV, respectively, as suggested by the TRIM table. Given that the sputtering yield is most sensitive to the surface binding energy, we can "calibrate" the surface binding energy so that the sputtering yield would match the experimental result obtained for xenon ions on tungsten at a certain primary ion energy, if needed. [92]

	Lattice Displacement Energy [eV]	Surface Binding Energy [eV]	Lattice Binding Energy [eV]	Sputtering Yield [atoms/ion]
TRIM Default Values	25	8.68	3	0.384

Table 2: TRIM input values

The main points of interest in the present study are the sputtering yield, angular and energy distribution of sputtered atoms. For both tungsten sputtering by low-energy xenon ions and tungsten self-sputtering, TRIM was run over a range of ion energies from 30 to 1000 eV and incidence angles from 0 to 89, and every simulation was run for each combination of energy and incident angle. With these tabulated data, we generated sputtering yield and ion emission energy functions of the incident ion energy and angle, and fit them to bivariate fitting functions using *symbolic regression* (SR) [87, 88], a type of regression analysis that searches the space to determine both the parameters and the form of mathematical equations simultaneously.

Nomenclature

a_0 Bohr radius = 0.529 [Å]
a_{BM} Sigmund Bohr-Mayer potential screening length = 0.219 [Å]
a_L Lindhard screening length [Å]
AW Atomic weight [g/mol]
E Ion energy [eV]
E_b Surface binding energy [eV]
S_n Nuclear stopping cross section [eV Å]
T Temperature [K]
U_s Surface binding energy [eV]
Y Sputter yield [atom/ion]
Y' Normalized angular sputter yield
Z Atomic number
e Elementary charge = 1.602 $\times 10^{-19}$ [C]
m Particle mass [kg]
n Number density $[1/\mathrm{m}^3]$
s_n Reduced nuclear stopping power
ϵ Reduced energy
ε_0 Vacuum permittivity = 8.854 $\times 10^{-12}$ [F/m] = 1.42 $\times 10^{-40}[\mathrm{C}^2/\mathrm{eV\AA}]$
α Ion incident angle [deg]
θ polar scattering angle of the incident on
ϑ polar scattering angle of the sputtered atom
ϕ azimuthal scattering angle of the incident on
φ azimuthal scattering angle of the sputtered atom

The expressions of the sputtering yield for tungsten under low-energy xenon ions exposure and tungsten self-sputtering are

$$\begin{aligned} Y_{Xe^+\to W}(E,\alpha) = {} & 7.246\times 10^{-2} + 2.236\times 10^{-3}E + 4.875\times 10^{-5}\alpha^2 + 4.775\times 10^{-7}E\alpha^2 \\ & - 5.515\times 10^{-3}\alpha - 4.702\times 10^{-7}E^2 - 6.214\times 10^{-11}E\alpha^4 \end{aligned} \tag{35}$$

$$\begin{aligned} Y_{W^+\to W}(E,\alpha) = {} & 7.246\times 10^{-2} + 2.236\times 10^{-3}E + 4.875\times 10^{-5}\alpha^2 + 4.775\times 10^{-7}E\alpha^2 \\ & - 5.515\times 10^{-3}\alpha - 4.702\times 10^{-7}E^2 - 6.214\times 10^{-11}E\alpha^4 \end{aligned} \tag{36}$$

Energy Distribution of Sputtered Atoms

The expressions of the emission energy distribution for tungsten under low-energy xenon ions exposure and tungsten self-sputtering are

$$\begin{aligned} E^{out}_{Xe^+\to W}(E,\alpha) = {} & 31.38 + 1.812\times 10^{-2}E - 569.7/E + 2.789\times 10^{-3}\alpha^2 \\ & + 9.318\times 10^{-8}E\alpha^3 - 0.1\alpha - 2.533\times 10^{-7}\alpha E^2 \end{aligned} \tag{37}$$

$$\begin{aligned} E^{out}_{W^+\to W}(E,\alpha) = {} & 7.12 + 1.11\times 10^{-1}E + 2.85\times 10^{-3}\alpha^2 + 4.579\times 10^{-5}\alpha^3 \\ & - 2.496\times 10^{-7}\alpha^5/(E - \cos(1.106\times 10^{-1}E)) - 6.145\times 10^{-2}\alpha - 2.664\times 10^{-4}E^2 \end{aligned} \tag{38}$$

We note that these expressions do not necessarily reflect the physics behind sputtering and are just intended for efficient numerical evaluations strictly in the ranges shown in the figures.

Angular distribution of Sputtered Atoms

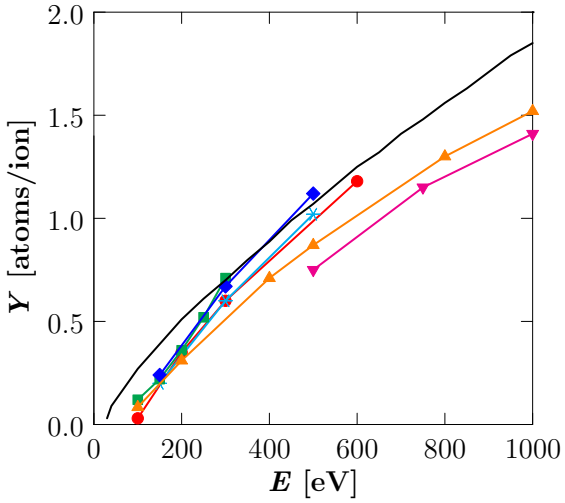

Figure 38: Total sputtering yield from smooth W surface as a function of Xe^+ ion energy and angle incident at 0°. • = Rosenberg (1962); ∗ = Wehner (1962); ■ = Stuart (1962); ♦ = Winters (1974); ▲ = Doerner (2005); ▼ = Tartz (2011); solid line = TRIM.

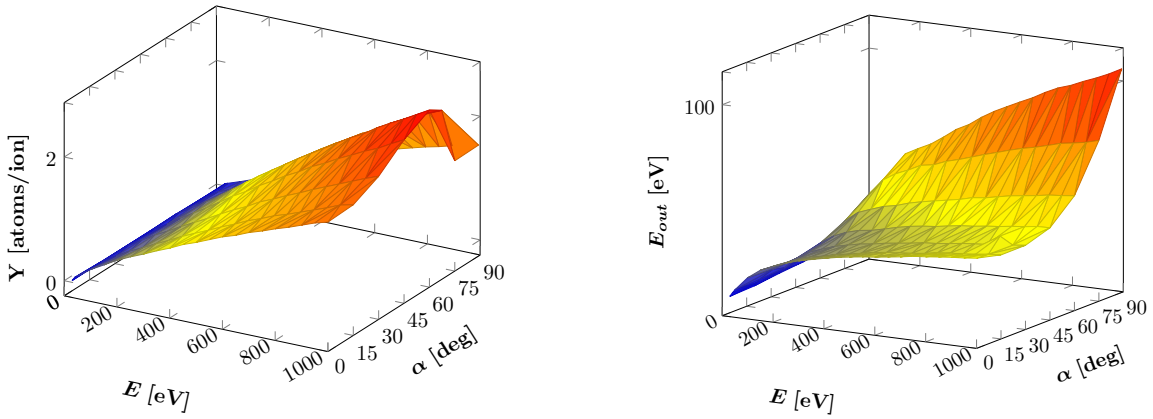

(a) (b)

Figure 39: (a) Surface plot of the total sputtering yield from smooth W as a function of Xe^+ ion energy and angle of incidence. (b) Surface plot of the emitted ion energy spectrum from smooth W as a function of Xe^+ energy and angle of incidence.

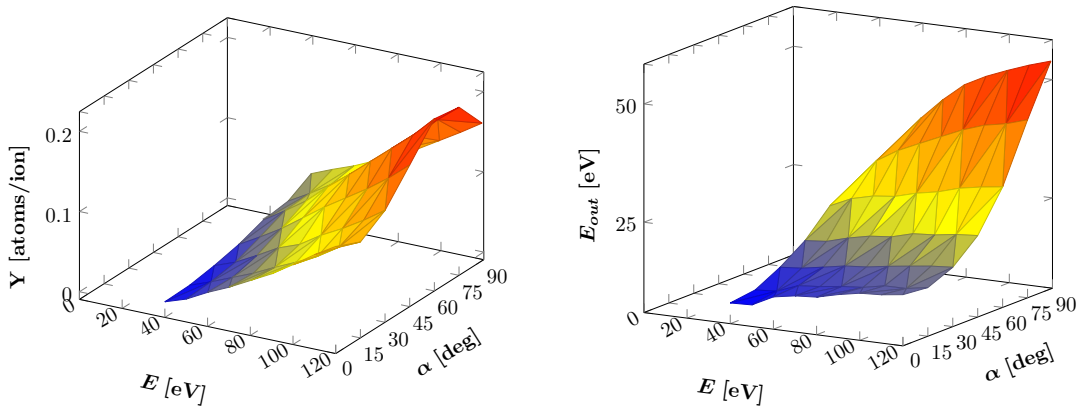

(a) (b)

Figure 40: (a) Surface plot of the self sputtering yield from smooth W as a function of W^+ ion energy and angle of incidence. (b) Surface plot of the emitted self ion energy spectrum from smooth W as a function of W^+ energy and angle of incidence.

Independent of ion incidence angle, the original Sigmund theory predicts sputtering profiles that are azimuthally symmetric and approximately diffuse in shape, corresponding to cosine-like profiles of the form $y \sim \cos(\alpha)^n$ ($n = 1$ for a diffuse profile). Namely, the emission angle ϑ measured from the target normal is sample from

$$\vartheta = \cos^{-1}(R^{1/2}), \tag{39}$$

whereas the azimuthal angle φ counted, say, from the x-axis within the target plane is a random fraction of 2π and generated as

$$\varphi = 2\pi R. \tag{40}$$

Note that in the above equations, and hereafter, all the random variables R are independent.

More recent experimental and numerical studies show a range of profile shapes. For normally incident ions on polycrystalline and amorphous targets, cosine-like profiles are generally observed with increasingly under-cosine shapes as ion energy is lowered and increasingly over-cosine shapes for higher ion energies, as shown in Figure 41. For obliquely incident ions at relatively high ion energy, observed profiles also tend to be azimuthally symmetric. However, for lower ion energies the measured profiles tend to be asymmetric with increased sputtering in the forward direction.

The current results will be used in ray-tracing Monte Carlo simulations of ion sputtering and redeposition in arbitrary surface geometries. In these simulations, primary rays are generated above the material surface with the corresponding incident energy E. Intersections of these primary rays with surface elements determines the corresponding angle of incidence α. E and α are then used to sample from the generated source functions, after which secondary rays with appropriate energies E_{out} and exit angles (sampled from a cosine distribution) are generated. These daughter rays are themselves tracked in their interactions with other surface elements, after which the sequence is repeated and granddaughter rays are produced. This process goes on until rays either escape the surface with an upward velocity –in which case the event is tallied as a successful sputtering event– or until their energy is below the threshold escape energy.

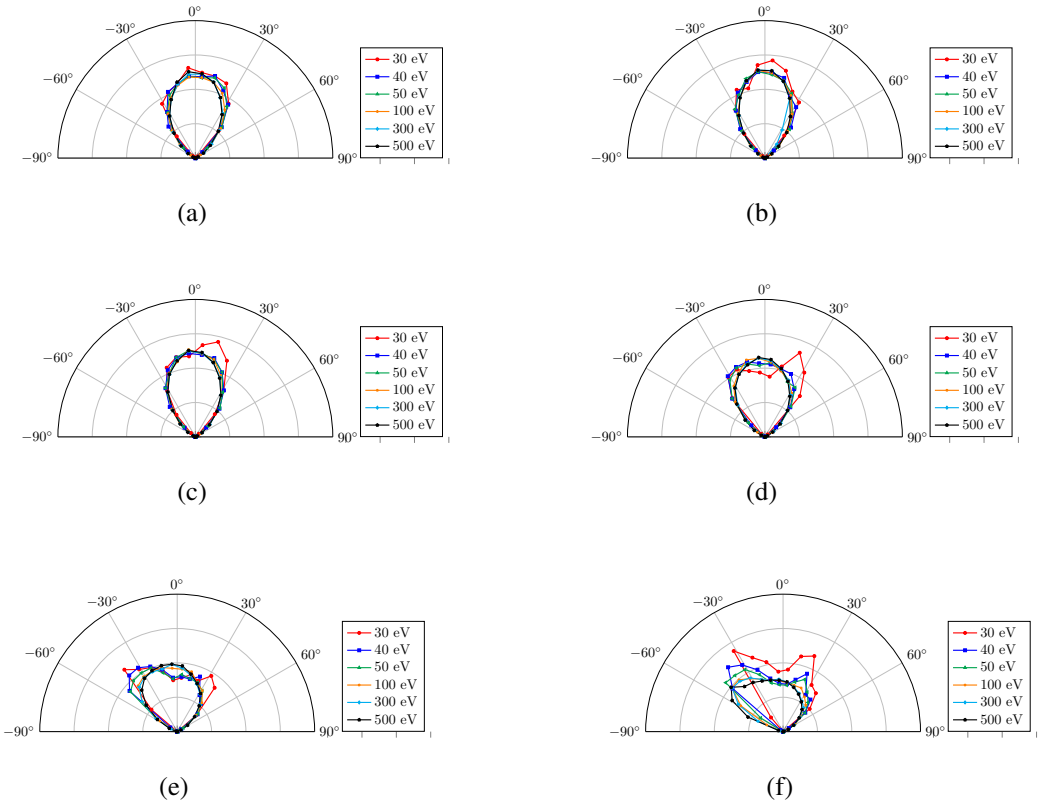

Figure 41: Angular distribution of sputtered W atoms under 30eV, 40eV, 50eV, 100eV, 300eV, 500eV Xe ion beam (a) at 0°, (b) 15°, (c) 30°, (d) 45°, (e) 60°, (f) 75°, (g) 89° incidence.

Adaptive Meshing

Sputtered atom deposition causes a surface to grow, opposing erosion of the surface caused by its own sputtering. These two processes must be accounted for in order to properly track the evolution of the surface in time. Surfaces are modeled in finite-element fashion as contiguous triangular elements joined at the vertices (nodes). For each iteration, the movement along mesh element i's surface normal Δh_i is given by

$$\Delta h_i = \frac{\left(N_{in}^W - N_{out}^W\right)_i \Omega \Phi A_{\text{eff}}}{A_i N_{in}^{Xe^+}} \Delta t$$

where N_{in}^W and N_{out}^W are the number of W atoms coming in and out of mesh element i, $N_{in}^{Xe^+}$ is the number of Xe ions bombarding the target, Ω is the atomic volume of sputtered/redeposited W, Φ is the effective Xe^+ flux, A_{eff} is the effective surface area of the cross section along horizontal direction, A_i is the surface area of the mesh element.

The results from the evolution equation and sputter yield calculations can be used to update the location of mesh cell centers at timestep $n+1$, given by

$$\begin{aligned} h_i^{n+1} &= h_i^n + \Delta h_i \\ &= h_i^n + \frac{\left(N_{in}^W - N_{out}^W\right)_i \Omega \Phi A_{eff}}{a_i N_{in}^{Xe^+}} \Delta t, \end{aligned}$$

and these displacements can be interpolated with smoothing technique to find the new locations of cell nodes.

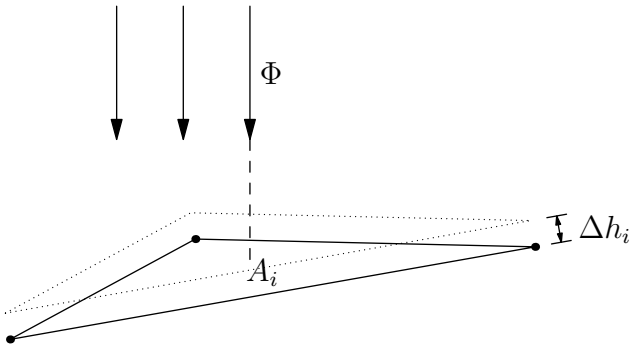

Figure 42: Triangular surface elements for adaptive meshing

Here, we use Laplacian smoothing as it is by far the most common smoothing technique. In its simplest form, consists of recursively placing each vertex at the average position of the neighboring faces containing that vertex. The smoothing operation is described per-vertex j as

$$h_j = \frac{1}{M} \sum_{i}^{M} h_{ij}$$

where M is the number of adjacent faces containing vertex j.

Results & Discussion

Here, three different structures: the uniform W bulk, microarchitected W foam and microarchitected W dendrite are studied. To understand the dynamic effect of sputtering redeposition, we examine the depth profile of W samples by shooting rays at normalized depths $z = 0.0$, 0,17, 033, 0.5, 0.67, 0.83 and 1.0 from 4 sides of the bounding box along the horizontal direction which cut through the center of each cross section at various time steps, and then take the average to obtain the statistics. Figure 43 is the time-dependent net sputtering yield of the W bulk, foam and dendrite. Initially, the net sputtering yield of the bulk is 0.75 atoms per ion, the foam 0.38 and the dendrite 0.26. With time, as the sputtering redeposition process gradually change the morphology of the samples, the net sputtering yields change accordingly. In Figure 44-(a), the average ligament thickness of the foam versus time in increment of 2 seconds up to 20.0 seconds is plotted. Figure 44-(b) shows the percentage thickness change $[\%]$ of the foam versus time in increment of 2 seconds up to 20.0 seconds. It shows that the microarchitecture change of the foam is most obvious at the surface layer ($z = 0.0$), where the ligament thickness starts off increasing slightly, then decreasing and then increasing again, which we interpret as that the top of the sample gets eroded by the incoming ions and then traps the outgoing ions. Whereas the bottom portion of the foam is not even touched.

To have a closer look at the sputtering redeposition process, we also plot the depth profile of the half-sized foam, as shown in Figure 45. In Figure 46-(a), the average ligament thickness of the dendrites versus time in increment of 2 seconds up to 20.0 seconds is plotted. Figure 9 (b) shows the percentage thickness change $[\%]$ of the dendrites versus time in increment of 2 seconds up to 20.0 seconds. At different depths, we observe their corresponding thickness variations with time,

which relate to their net sputtering redeposition yields, and that can be attributed to the different height and orientation of each dendrite. Although having different depth profiles versus time, both the W foam and the W dendrites demonstrate their effectiveness in reducing the net sputtering yield, and thus can be ideal candidates for plasma devices.

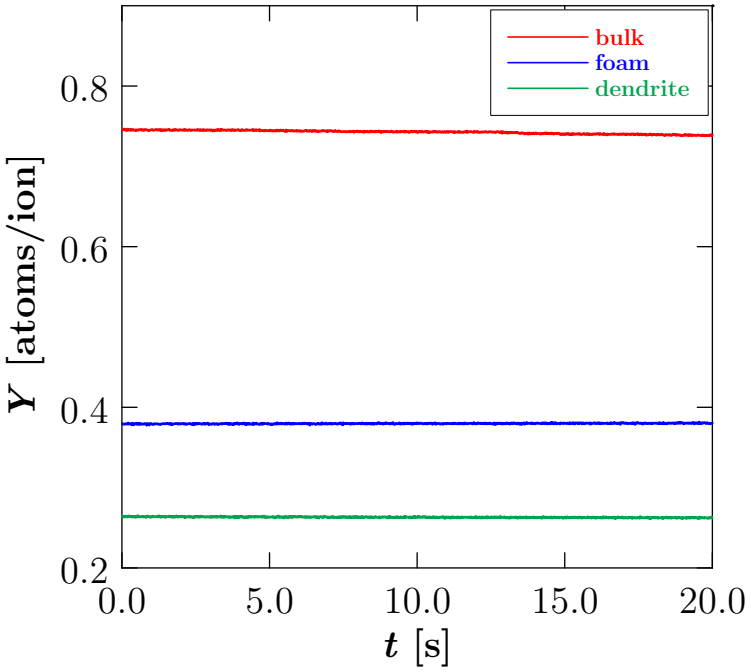

Figure 43: Calculated erosion rates of bulk, foam, and dendrites.

Conclusions

Surface morphology (from micron-level surface roughness to 0.1-mm patterning) can strongly affect the net sputter yield of plasma-facing surfaces. Here, we have presented an examination of the effects of both surface architecture on sputter deposition and erosion using a 3D computationally efficient model.

2.2.7. Particle & Heat Transport in Foams

A 3-D reconstruction of a 65 PPI tungsten foam sample is generated using 975 X-ray tomography images. The foam is represented as either a finite element (FE) model or a pixel-based model, each holding different advantageous properties making them suitable for various applications. The foam model reconstruction procedure is outlined below and two simulation techniques and results using each model type are given.

Reconstruction Procedure

The grayscale X-ray tomography images are first passed through a filter with a set threshold value to convert each image into a 2-D binary array. The filtered images are then stacked on top of each other to create a 3-D logical array with 1's representing material and 0's representing space. This creates the pixel-based representation of the foam. An isosurface routine is run on this foam representation, generating a surface composed of triangles bounding the volume of the foam. The number of surface elements can be on the order of 10^7; a mesh-reduction scheme is run to reduce

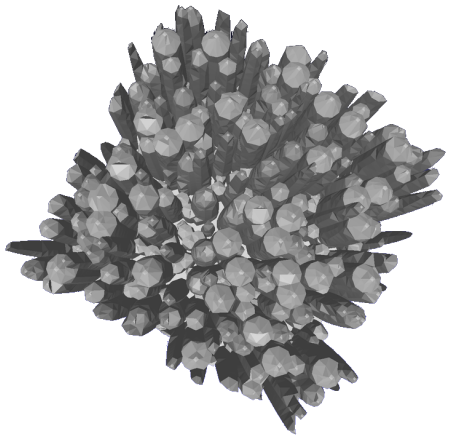

Figure 44: Dendrite geometry generated using meshlab.

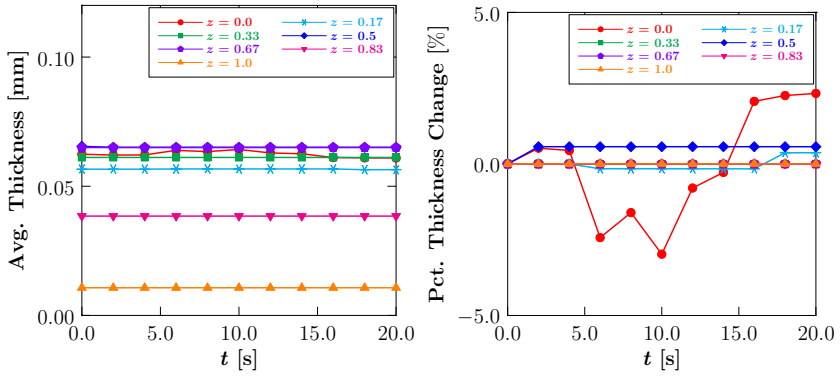

Figure 45: (a) Average thickness of the W foam versus time at various normalized depth. (b) Percentage thickness change of the W foam versus time at various normalized depth.

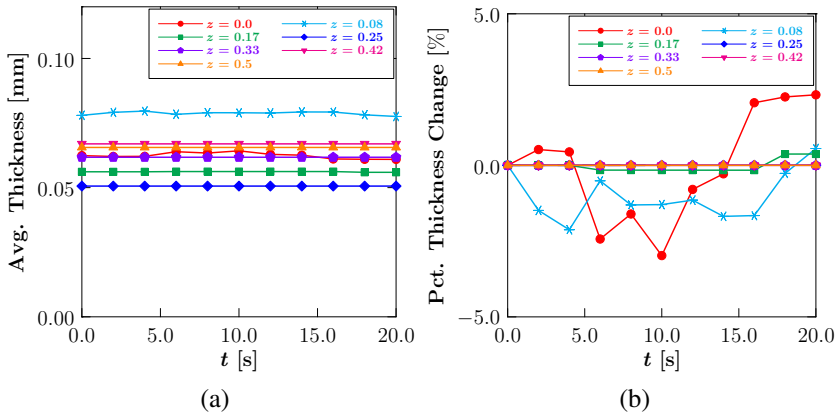

Figure 46: (a) Average thickness of the half-sized W foam versus at time various normalized depth.(b) Percentage thickness change of the half-sized W foam versus time at various normalized depth.

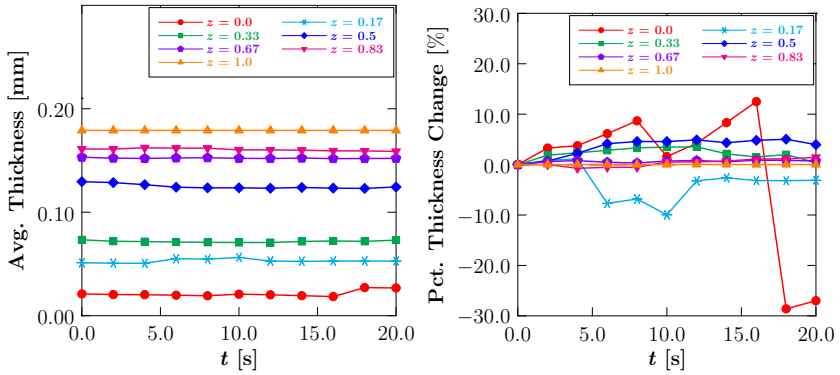

(a) (b)

Figure 47: (a) Average thickness of the W dendrites versus at various normalized depth. (b) Percentage thickness change of the W dendrites versus time at various normalized depth.

this number down to the order of 10^5. This generates a reasonably sized FE model of the foam suitable for FE simulations.

Though the reconstruction procedure can be time-consuming to run and generates large files, the advantage of using this method is the creation of a foam model based on real data. This eliminates the need to come up with an approximate foam shape and accurately captures the geometry of a foam with ligaments randomly distributed.

Transient Heat Conduction with Radiation

Using the FE model of the foam, a transient heat conduction study is run with two radiation cases compared. In the first case radiation emitted from the ligaments is allowed to re-absorb into the foam. In the second case, radiation is not allowed to re-absorb. Because the foam is porous in structure, we expect mutual irradiation of the ligaments to expedite the conduction of heat through the foam's ligaments. A heat pulse of 1 MW/m^2 is applied to the top surface of the foam for 10 seconds and the transient effects are simulated for an additional 40 seconds. The temperature at a point at the bottom-center of the foam is tracked with both the surface-to-ambient and surface-to-surface radiation cases compared, as seen in Figure 49. The effects of convection are neglected. The total conductivity of a foam in the absence of convection is given as the sum of the conductivity of the solid and conductivity due to radiative contribution, with the latter given as

$$\lambda^*_{\mathrm{r}} = 4\beta_1\sigma\overline{T}^3 t \exp(-K_{\mathrm{s}}\frac{\rho^*}{\rho_{\mathrm{s}}}t) \tag{41}$$

where β_1 is a constant less than 1, σ is Stephan's constant, $\overline{T}$ is the mean temperature, t is time, K_{s} is the extinction coefficient, and ρ^*/ρ_{s} is the relative density of the foam. It is readily seen that this expression is always positive and will therefore contribute to a higher conductivity in foams, consistent with the simulation results.

Monte Carlo Simulations of Atomic Transport

The pixel-based model of the foam can be used in particle transport simulations, with each pixel representing an atom or group of atoms depending on the length scale.

One potential application of foams is in self-healing materials subjected to helium ion bombardment. As the upper layers are stripped of atoms due to sputtering, lower layers will thicken

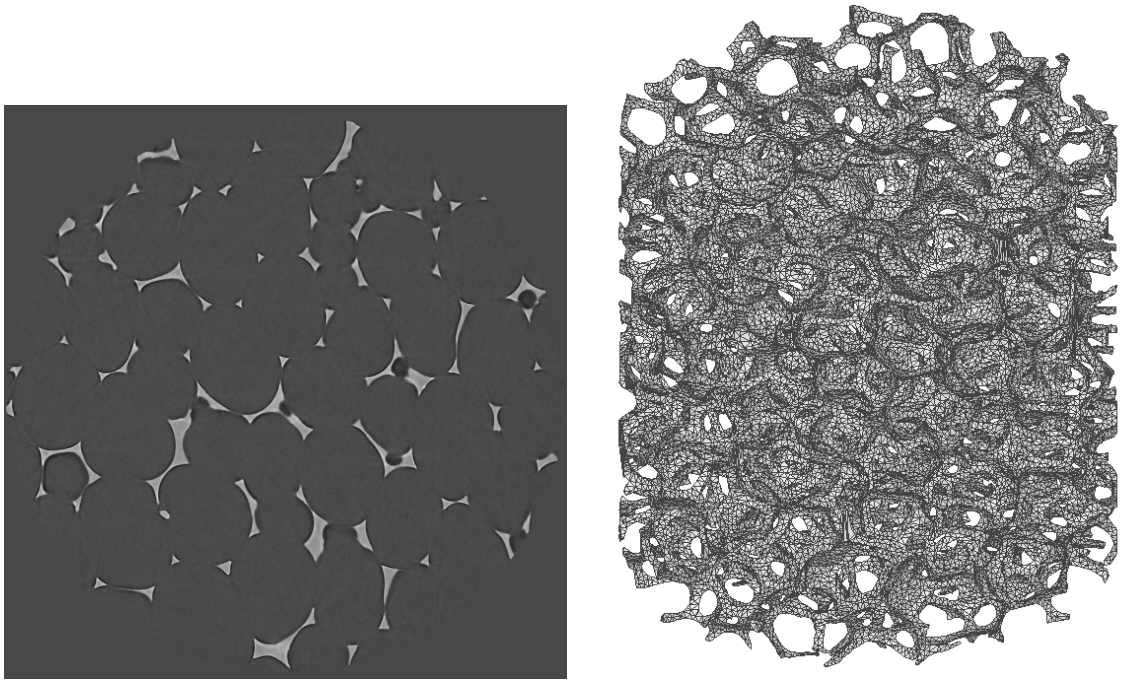

(a) (b)

Figure 48: Two stages of the foam reconstruction. (a) Original X-ray tomography scan of foam; (b) FE reconstruction with triangular elements.

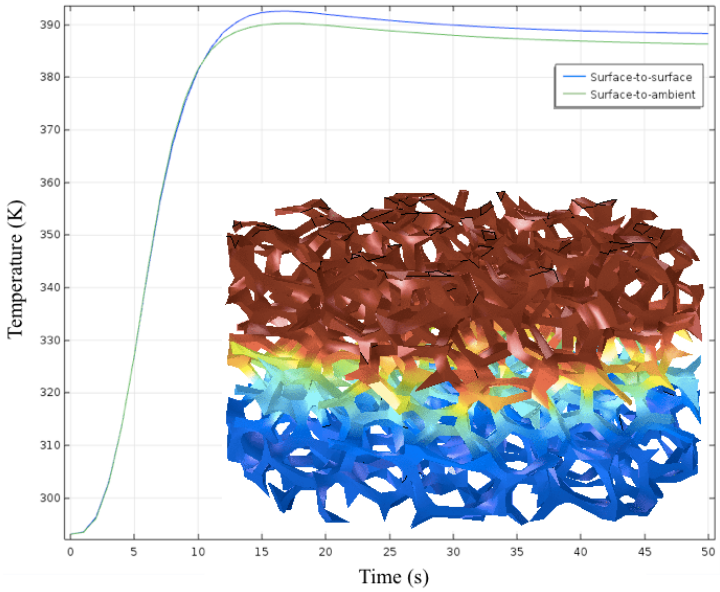

Figure 49: Transient heat study on half-foam FE model. Two different radiation cases are tested with temperature taken at a point at the bottom-center of the foam.

as some of the atoms are redeposited on their surface as seen in Figure 50a. Additionally, it is necessary to determine the penetration depth of the ions. Upper layers of the foam cast ”shadows” on the lower layers where ions cannot reach (Figure 50b). A pixel-based model of the foam can easily capture the shadowing effect by considering each surface pixel as a discretized surface element. If all of the pixels directly above a surface pixel are assigned values of 0, it is open to ion bombardment. If there exists a pixel assigned a value of 1 in that line, it is shadowed.

The pixel-based approach to simulating this phenomenon eliminates the need to run a potentially time-consuming ray-triangle intersection algorithm by discretizing the system into a grid. Additionally, the geometry of the foam can easily be altered by manipulating the pixels to generate foams with thicker or thinner ligaments to compare foams of different densities.

2.3. Task 3: In-situ Testing of Erosion & Redeposition

2.3.1. Sputtering Erosion of W-Foam in a Helium Plasma

The weight loss measurements have been made on each one of the tested samples to determine the effective sputtering rate. These measurements revealed some significant loss of material during helium irradiation past the tungsten sputtering threshold of 100 eV. While the first test was inconclusive due to the sample getting caught on the manipulator, each other sample lost over 1 mg of mass, with sample 4 losing over 5 mg. This is significant when considering the material?s ability to self-heal during irradiation. Measurements of the second halves of tungsten-coated rhenium pillars (TEX3) showed much lower weight loss than the first halves. This can be attributed to the fuzz and web nano-structure resistance to sputtering, presumably by deposition of sputtered off atoms on the growing fuzz or web nano-structure. Weight loss tests on planar tungsten were conducted in the past, and the results were comparable to the current foam samples, except for sample 2, run2 of the 45 PPI TEX3 (last sample in Table 3). When comparing different foam architectures, it is evident that nodular foam (TEX1) performs better than foam with pillars (TEX2) at reducing material loss. This may be due to the inability of Re pillars to trap sputtered surface atoms. Since all weight loss ratios in Table 3 are above one, all textured tungsten foam samples performed better than flat tungsten.

2.3.2. Sputtering Erosion of Metallic Foams in Ar Plasma

Contributors: Richard E. Wirz, Gary Z. Li, Angelica Ottaviano, Cesar Huerta, Zhitong Chen

Experimental Setup

The following experiments were performed in the Wirz Research Group?s Plasma interactions (Pi) test facility. The Pi facility consists of a 250 A LaB6 hollow cathode plasma source coupled to an axial magnet system for directing a focused plasma to a target sample. The sample is biased negatively relative to ground potential (anode) to enable energetic ion bombardment for sputtering studies. An abbreviated schematic of the Pi facility is shown in Figure 51. The magnetic field near the target was designed to enable diagnostic access to the near-target plasma region where sputtering and redeposition processes are concentrated. The operating conditions used for these sputtering tests are reproduced from Li et al. in the table below:

Results

Dual-Foam Sputtering Experiment (Jointly funded with MURI project)

The Dual Foam sample is a multi-layered target composed of a 20 PPI Al foam, 40 PPI Cu foam, and solid nickel plate as shown in Figure 52. The main goals of this test were to determine the

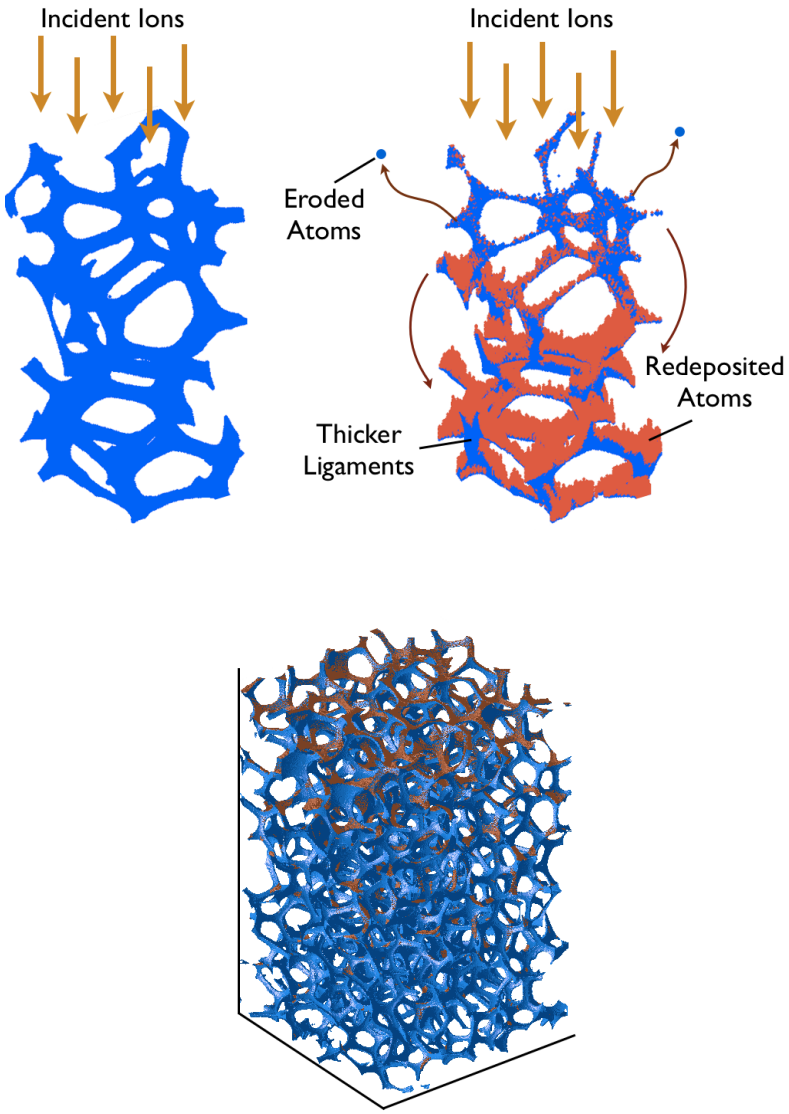

Figure 50: Ion deposition simulations using the pixel-based foam reconstruction. (a) Foam section showing the sputtering of atoms on higher ligaments and redeposition on lower ligaments ; (b) Foam section with ion-facing surfaces shown in red.

Sample	Weight-Loss Ratio (Flat W / Textured W)
45 PPI TEX1	6.96
80 PPI TEX1	N/A
45 PPI TEX2	5.91
80 PPI TEX2	1.54
45 PPI TEX3 (sample 1 run 1)	2.07
45 PPI TEX3 (sample 1 run 2)	3.72
45 PPI TEX3 (sample 2 run 1)	2.72
45 PPI TEX3 (sample 2 run 2)	19.76

Table 3: Results of weight loss ration of flat W to textured W. The texture type is indicated by TEX1 for nodular W-foam, TEX2 for Re micro-pillars on top of nodular W-foam, and TEX3 for W-coated Re-micro-pillars on top of nodular W-foam, respectively. A value higher than unity indicates a sel-healing effect, where some of the sputtered atoms are deposited onto the surface.

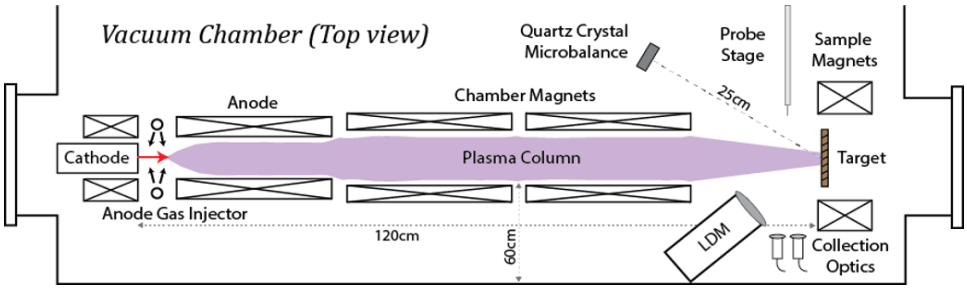

Figure 51: Pi facility schematic.

Parameter	Typical values
Plasma density	$10^{18} m^{-3}$
Electron temperature	7 eV
Ion Energy to target	40-300 eV
Ion flux to target	$10^{17} cm^{-2} s^{-1}$
Exposure diameter/ area	1.5 cm/ 1.8 cm^2

Table 4: Near-target plasma conditions

sputtered particle transport properties between different layers using Scanning Electron Microscope (SEM) images and Energy Dispersive Spectroscopy (EDS). In this test, the target is rotated by approximately 30° relative to the plasma and the LDM line-of-sight is normal to the target surface. The QCM sensor is fixed at 30° relative to the target normal at a distance of 25 cm. By monitoring the differential sputtering rate, the QCM can provide information on how much the sputtering yield changes over the duration of the test. The plasma configuration presented in the previous section is used to provide consistent focused ion flux to the target with the target biased to -250 V to provide energetic ion bombardment. The test was conducted over 5 days for a total of 26 hrs of biased exposure.

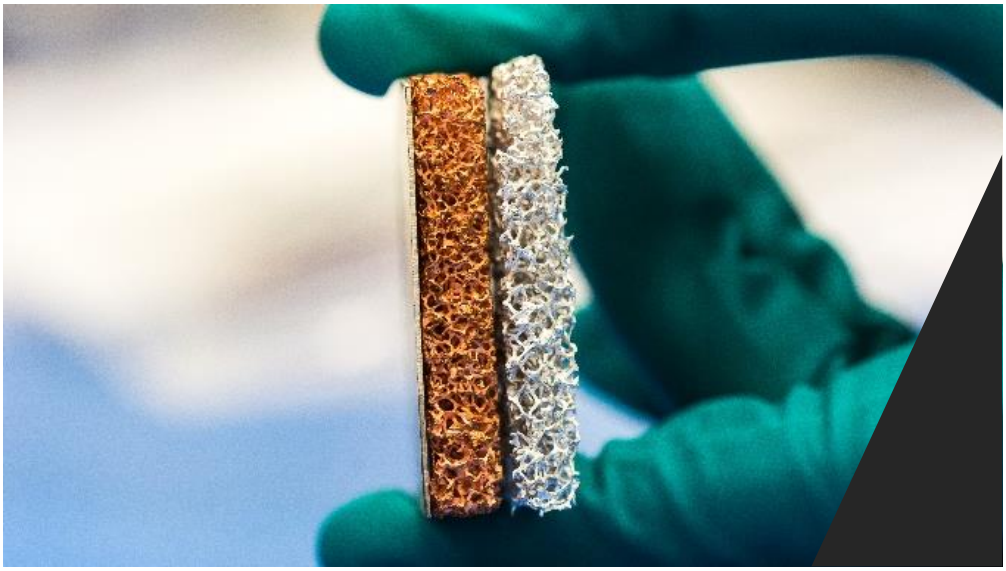

Figure 52: Dual Al-Cu foam sample.

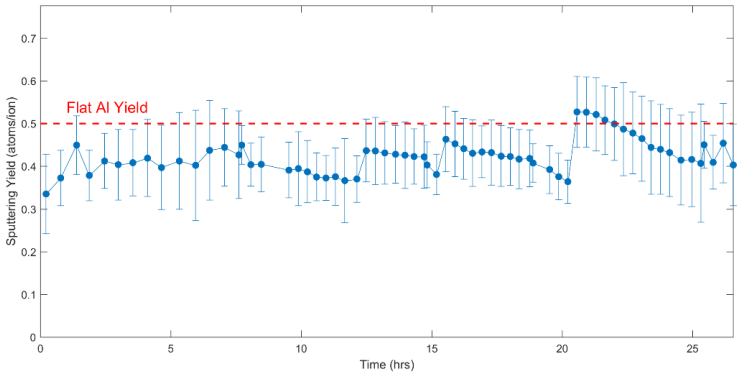

Figure 53: Approximated total sputtering yield of dual foam.

Since the QCM was fixed to a single polar angle, the total sputtering yield cannot be directly obtained. However, the total yield can be estimated by assuming the differential sputtering yield is constant at all polar angles and is azimuthally symmetric. Based on the analysis in Li et al.[**?**], the total sputtering yield can be plotted as a function of time in Figure 53 with the yield of flat aluminum included for reference. Clearly, the sputtering yield of the aluminum foam with minor contributions, if any, from the underlying copper and nickel layers, is significantly less than that of the flat aluminum sample. Additionally, the sputtering yield for the dual foam sample is more or less constant over the 26 hour exposure with minor discontinuities due to start-up transients between days of testing.

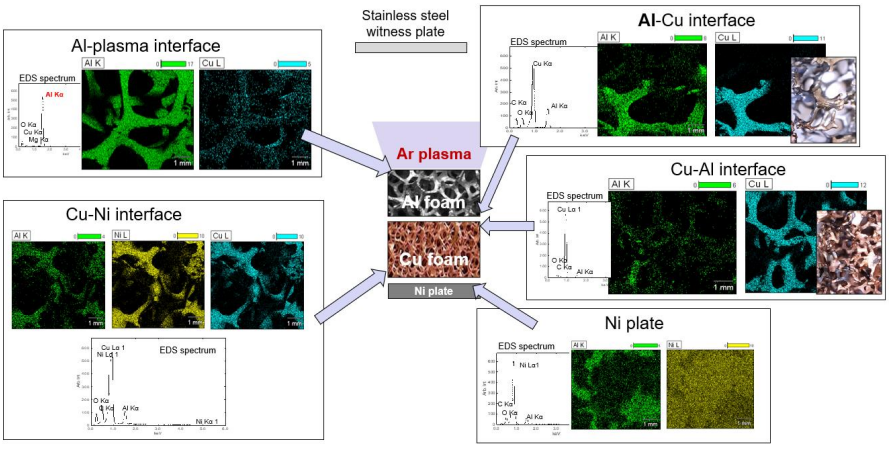

Figure 54: EDS spectra of dual foam interfaces.

The EDS results are presented in Figure 54. It is shown that there is cross-deposition between all interfaces, i.e. aluminum is present on the copper foam and copper is present on the aluminum foam. This observation indicates that the plasma is penetrating through the thin foam layer and reaching the underlying layers. Qualitatively, this result implies that layering of foams could have useful applications and that understanding the inter-foam transport is of key importance for utilizing foam for plasma device applications.

80 PPI W Foam Sputtering Measurements

The second experiment focused on identifying the sputtering resistance of a tungsten foam of relevance to fusion divertors. The 80 PPI tungsten foam sample was manufactured by Ultramet Inc. using a chemical vapor deposition process and was previously exposed to low-energy helium bombardment in the PISCES facility [**?**]. In addition, W coated rhenium micro-pillars were deposited on the foam ligaments for helium bubble formations studies as shown in the SEM images in Figure 56. The sample was oriented perpendicular to the plasma column and exposed to 250 eV argon ion bombardment for 2 hours at the same standard operating conditions as presented previously. QCM measurements were taken to evaluate the sputtering yield over this period. After exposure, the sample was removed from vacuum and examined via SEM.

The post-exposure SEM images in Figure 56 that the micro-pillars are all but eroded away after

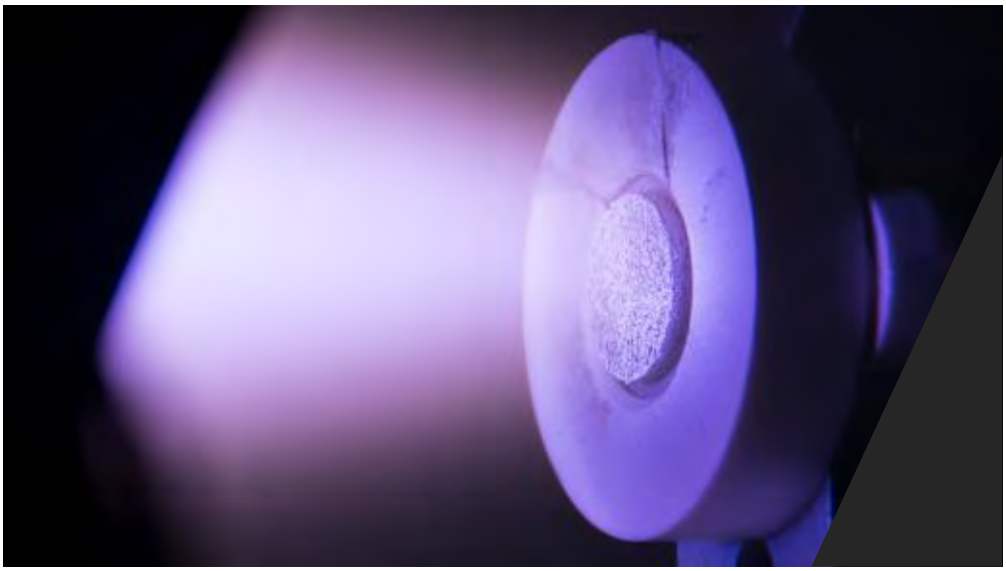

Figure 55: W foam sample in the Pi facility.

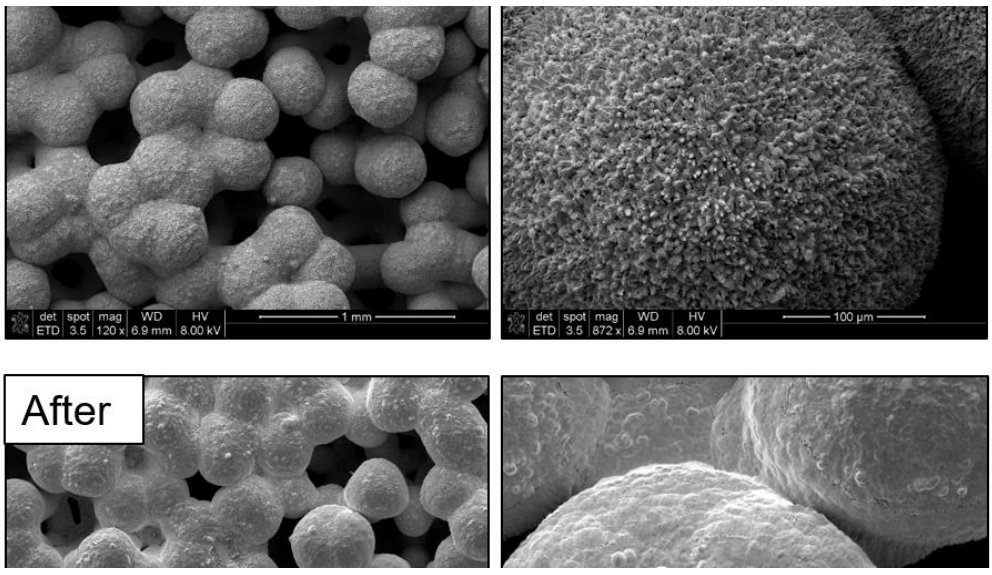

Figure 56: SEM images of the W sample.

2 hours. However, the geometry of the W foam is roughly unchanged indicating that the erosion time-scale is much larger than 2 hours. In contrast to the dual foam sample in the previous section, the angular sputtering distribution was measured by the QCM as shown in Figure 57. Similar to the SEM images, there are no major changes in the sputtering profile over time. In general, the differential sputtering rate appears to increase monotonically towards 0° polar angle. However, it must be noted that the W foam structure as seen in the SEM images is more bulbous than a normally fabricated foam sample which has longer ligaments and a matrix-like shape. As such, there is a larger projected surface area for sputtering which may contribute to the measured angular sputtering shape. The angular sputtering profiles are integrated to obtain the total sputtering yields as a function of time and is shown in Figure 58. As expected with the unchanging angular profile, the sputtering yield is also effectively constant over the 2 hour test duration. The ion fluence is calculated on the secondary x-axis by assuming a constant ion flux of 2×10^{17} ions $cm^{-2}s^{-1}$. On average, the W foam sputtering yield is 27% less than the value of 0.22 atoms/ion reported by Yamamura for 250 eV argon ions. While the 27% reduction is significant relative to flat tungsten, the sputtering yield for a more typical W foam structure (i.e. no bulbous structures, longer filament lengths, more pore area) is expected to be even further reduced. The results obtained here prove that tungsten foam will provide a substantial improvement upon flat tungsten divertors intended to be used in ITER, and may also have substantial implications for high current density EP devices that require a similar sputtering resistance.

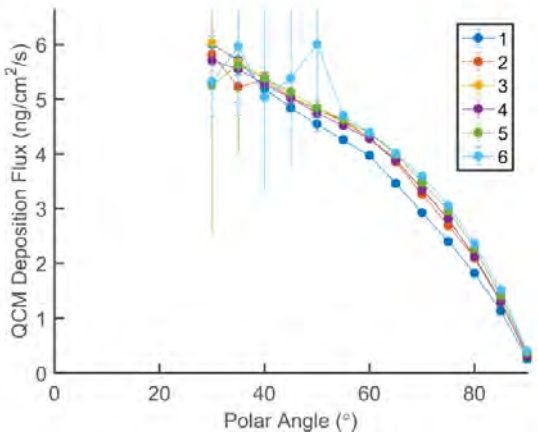

Figure 57: Angular sputtering profile for W foam.

2.4. Task 4: Experimental Thermomechanics

A new experimental facility constructed at UCLA for the simulation of high heat flux effects on plasma-facing materials is described. The High Energy Flux Test Facility (HEFTY) is equipped with a Praxair model SG-100 plasma gun, which is nominally rated at 80 kW of continuous operation, of which approximately 30 kW reaches the target due to thermal losses. The gun is used to impart high intermittent heat flux to metal samples mounted within a cylindrical chamber. The

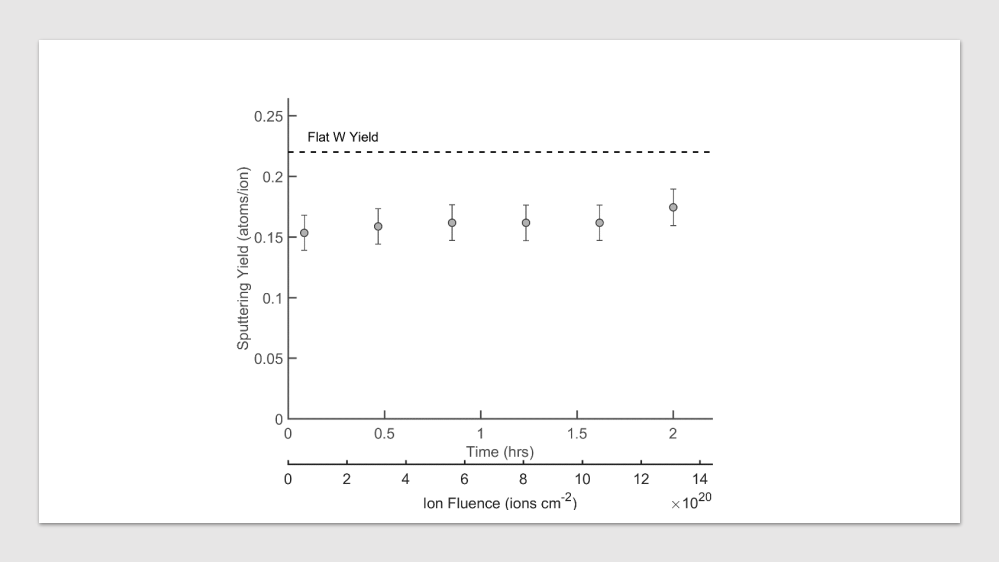

Figure 58: Total sputtering yield for W foam.

system is capable of delivering an instantaneous heat flux in the range of 30-300 MW/m^2, depending on sample proximity to the gun. The duration of the plasma heat flux is in the range of 1-1000 s, making it ideal for studies of mild plasma transients of relatively long duration. Tungsten and tungsten-copper alloy metal samples are tested in these transient heat flux conditions, and the surface is characterized for damage evaluation using optical, SEM, XRD, and micro-fabrication techniques. Results from a Finite Element (FE) thermo-elastoplasticity model indicate that during the heat-up phase of a plasma transient pulse, the majority of the sample surface is under compressive stresses leading to plastic deformation of the surface. Upon sample cooling, the recovered elastic strain of cooler parts of the sample exceeds that from parts that deformed plastically, resulting is a tensile surface self-stress (residual surface stress). The intensity of the residual tensile surface stress is experimentally correlated with the onset of complex surface fracture morphology on the tungsten surface, and extending below the surface region. Micro-compression mechanical tests of W micro-pillars show that the material has significant plasticity, failing by a "barreling"mode before plasma exposure, and by normal dislocation slip and localized shear after plasma exposure.

The magnitude and duration of the heat flux imparted to samples is computer controlled, and the number of pulses is also programmable. Circular tungsten specimens of 5.08 cm diameter and 0.508 mm thickness are mechanically attached to a specially designed sample holder, which delivers a constant jet of impinging cooling water (at room temperature) onto the back surface of the samples, while the front surface remains exposed to the incoming plasma heat flux. Calculated convective heat transfer coefficients on the order of 10^6 W/m^{2}K have been obtained for the back surface of the samples for a typical flow rate of 19 L/min. This flow rate can be reduced to reproduce a variety of experimental conditions. The aim of testing materials under cooling is primarily to generate thermal gradients in thick specimens, which in turn, will result in a range of thermal stress states that can be controlled by varying the cooling and heating rates of the samples. The dimensions of test chamber are: length = 81.28 cm, and diameter = 60.33 cm, operating at atmospheric pressure, and uses Ar as a shroud gas to guard against oxidation of the sample surface. The installed diagnostics consist of thermocouples, pressure gauges, and flow meters to determine

quantities such as the energy absorbed by the cooling circuit during an experimental run, as well as to ensure that the experimental conditions are within the safety confines of the unit. Other diagnostics include a dedicated data acquisition and computer control system, voltage and current meters, and a LabView interface.

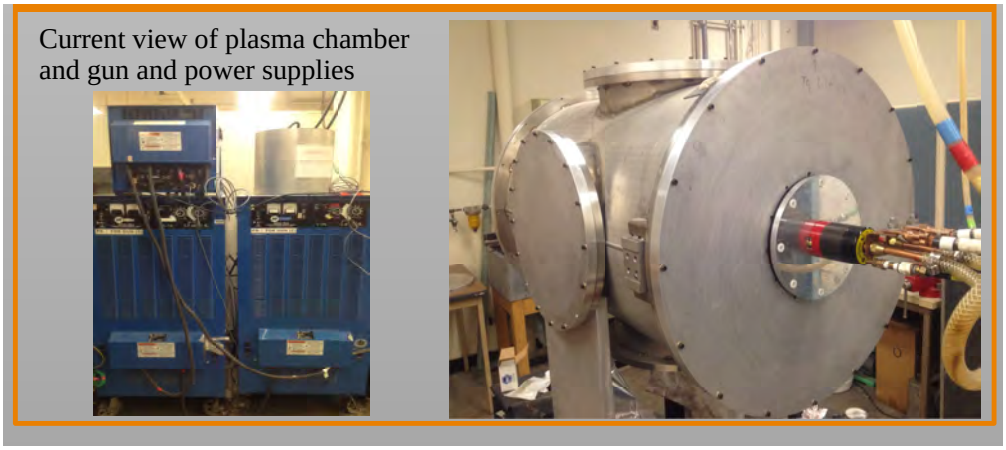

Figure 59: HEFTY device used for high heat flux experiments

While the measured heat flux is relatively low compared with previous experimental simulations of more intense plasma transients in excess of 100 MW/m^2 [93, 94], it allows for studies of the influence of low intensity and long-duration plasma transients that are also expected in EP, and PP devices. The samples tested in this experimental campaign were initially polished to prevent premature cracking from rough surface notches. Samples were subsequently exposed to 1100 pulses of 25 MW/m^2 heat flux, each with a duration of 4-6 seconds. The sample holder is designed in such a way that a constant jet of impinging water strikes the back surface of the sample at all times. Three tubes (one inlet and two outlet) carry water to and from the sample. Thermocouples were affixed to the inlet and outlet streams to monitor the change in temperature of the water during each pulse, this data can be seen for a single pulse. Details of the thermomechanical tests accomplished so far in the HEFTY facility are discussed in [95]. Our plans for upgrade of the themomechanical plasma testing facility (HEFTY) at UCLA, and its utilization in conducting new and innovative experiments on *mechanically loaded* microarchitected surfaces are discussed below.

Stress assisted diffusion of point defects can lead to interesting microstructural phenomena of particular interest to high temperature applications [96]. In order to further develop microarchitected materials it is important to fully understand the effects of stress on the evolution of the microstructure. This information can be used to improve current materials designs and optimize the systems for given applications. Hight heat flux experiments have been performed using HEFTY device shown in figure 59 to investigate resilient of different materials under thermal cyclic loading. New efforts are toward having more controlled experiments to examine samples under different stress regimes and study variety of failure modes. The results can be used to verify and improve computer simulations in this area of study.

Experimental Configurations

New sample holders are designed and fabricated to provide variety of constrains on samples and introduce combined thermal and mechanical loading during experiments. Using the new designs

samples can be tested under following configurations.

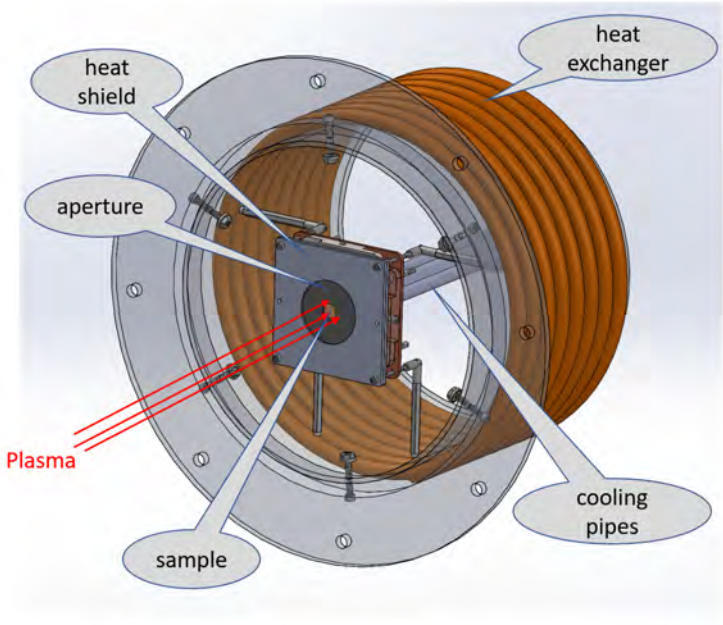

Figure 60: Free radial expansion configuration

Free Radial Expansion

This configuration can be used to experience thermal shock in different materials. As shown in figure 60 and 61 the front face of the sample is exposed to plasma and the back face is being cooled by conducting heat to cooling plate. Sample is being hold by spring loaded retaining fins and can expand freely in radial direction. Temperature gradient through thickness of the sample causes tensile stress on the back face which can grow the existing micro cracks on this face. Samples with different surface conditions can be examined to investigate main factors on causing thermal shock in materials.

Uniformly Constrained Sample

In this configuration a constraining block made of a high temperature material such as molybdenum or tungsten constrains the sample uniformly as shown in figure 62. Constraining block is not directly exposed to plasma and has smaller thermal expansion coefficient than the sample, so it can uniformly constrain the sample during experiment. This configuration can be used to generate experimental results for thermal cyclic loading and fatigue study for variety of materials.

Combined Mechanical and Thermal Loading

Ratcheting is one of the most critical failure modes that can occur in components under pressure and thermal cyclic loading such as pressure vessels.In this regime material goes under accumulative strain and fails eventually. Sample holder shown in figure 63 is designed and fabricated to study ratcheting in different materials by applying mechanical load on the sample while using plasma for thermal cycling. The bar sample is being pulled by grippers from both ends and the front face is exposed to plasma while the back face is being cooled through conduction with colling plate. At certain combination of mechanical and thermal loading, material will fail due to ratcheting. The results obtained from this experiment can be used to better understand this failure mode for different materials.

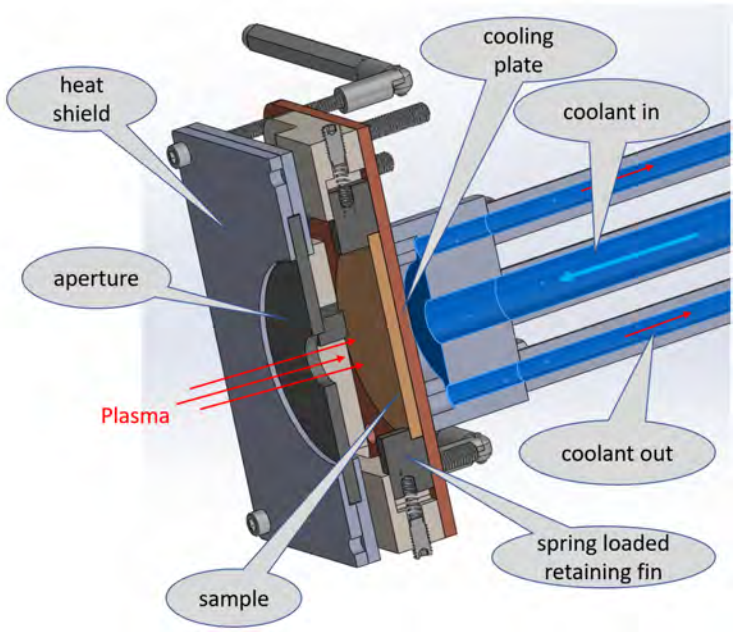

Figure 61: Cross section view of free radial expansion configuration

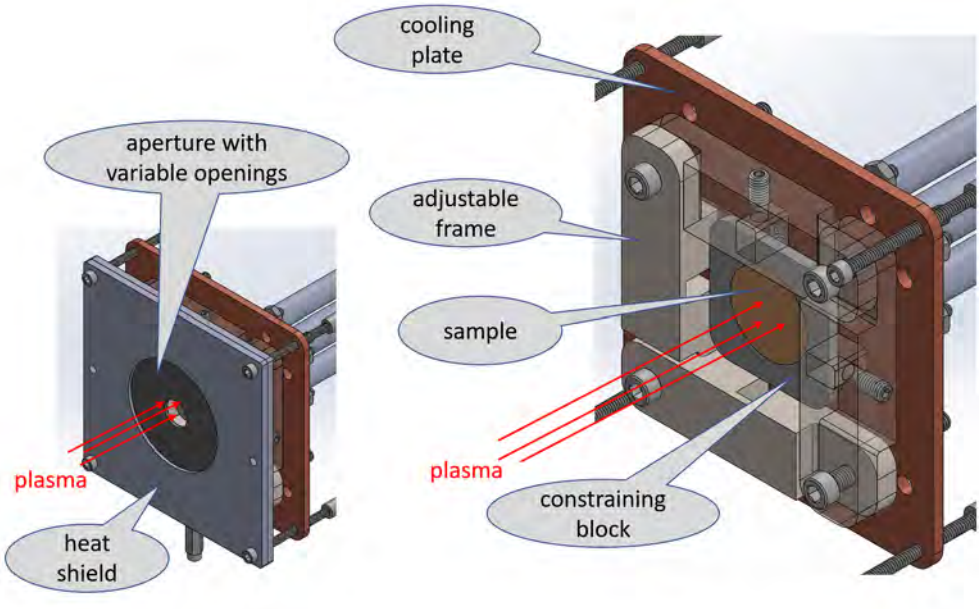

Figure 62: Uniformly constrained configuration

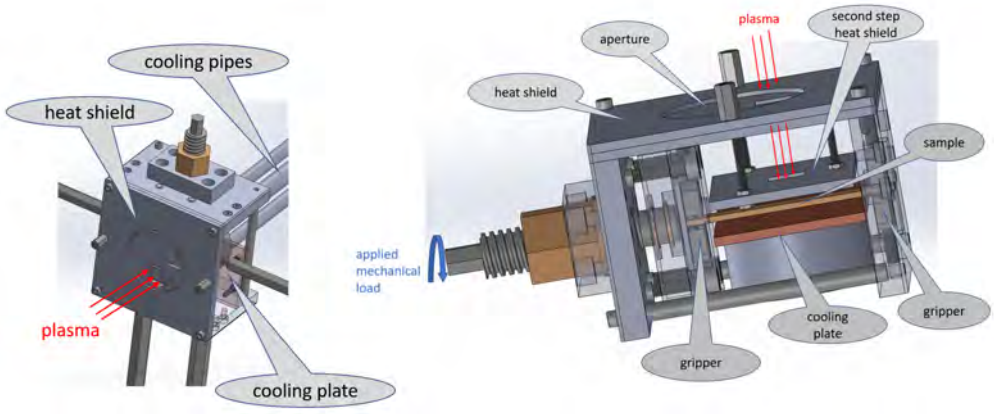

Figure 63: Combined loading configuration

3. Research Productivity & Publications

3.1. Presentations in Conferences & Meetings

The following presentations have been given by the Principal Investigator and or members of his team during the three-year period of the project:

1. Giacomo Po. An anisotropic non-singular theory of dislocations, MRS Spring Meeting 2017, Phoenix, AZ.
2. Giacomo Po. A continuum dislocation model of wedge micro-indentation, MRS Spring Meeting 2017, Phoenix, AZ.
3. Giacomo Po, Yinan Cui, David Rivera, David Cereceda, Tom Swinburne, Jaime Marian, and Nasr Ghoniem , Dislocation Dynamics simulations in micro-architectured tungsten, Multi-scale Modeling of Materials-2016 October, 9, 2016, Dijon, France.
4. Yinan Cui, Giacomo Po, Nasr Ghoniem, Irradiation effects on hardening & strain bursts at the microscale, Multiscale Modeling of Materials-2016 October, 9, 2016, Dijon, France.
5. N.M. Ghoniem, Micro-architected Materials for Space Propulsion and Power, October 14, 2016, Complutense University, Madrid, Spain.
6. N.M. Ghoniem, Development of micro-architected materials for space propulsion and pulsed power applications, Johns Hopkins University, November 4, 2016.
7. Yinan Cui, Giacomo Po, Nasr Ghoniem,, Loading controlled transition of plastic flow from dislocation avalanche to quasi-periodic strain bursts, International Conference on Plasticity, Porto Vallarta, Mexico, January 3, 2017.
8. N.M. Ghoniem, Resilient Self-Healing Materials for the Extreme Environment of Space Electric Propulsion & Power, AFOSR Review Meeting, Arlington, VA, May 22-26, 2017.
9. Yinan Cui, Giacomo Po, Nasr Ghoniem, ”Strain Bursts and Dislocation Avalanches in Obstacle-Hardened Materials,” American Physical Society Meeting, Los Angeles, CA, March 5-10, 2018, Invited presentation.
10. Andrew Sheng, Giacomo Po, Nasr Ghoniem, ”A Mesh-Independent Method for 3-D Propagating Cracks in Finite Domains,” U.S. National Congress on Applied and Theoretical Mechanics, Chicago, Illinois, June 5-9, 2018.

11. Yinan Cui, Giacomo Po, Nasr Ghoniem, "Dislocation Avalanches in Microplasticity," International Conference on Strength of Materials, The Ohio State University, Columbus, Ohio, July 15-19, 2018, Invited.
12. N.M. Ghoniem, "Multiscale-Multiphysics Modeling of the Mechanics of Extreme-Environment Materials," 9th International Conference on Computational Methods, Rome, Italy, August 6th ? 10th , 2018, Plenary Talk.
13. Nasr M Ghoniem, Yue Huang, and Fabio Cismondi, Organizers, Mini-symposium on "Computational Models for Multiscale/Multiphysics of Extreme Heat Flux Materials," The 9th International Conference on Computational Methods (ICCM2018), Rome, Italy, August 6-10, 2018.
14. J. Marian, Resilient Self-Healing Materials for the Extreme Environment of Space Electric Propulsion & Power, AFOSR Review Meeting, Arlington, VA, August 7-12, 2018.
15. Yinan Cui, "Temporal and spatial plastic instability of micrometer-scaled materials," International Conference on Multiscale Modeling of Materials, Osaka, Japan, Oct. 28- Nov. 2, 2018. Calculations of secondary electron emission yields in micro-architectured W and BN surfaces?
16. Jaime Marian, ?Calculations of secondary electron emission yields in micro-architectured W and BN surfaces," 14th Conference on Computer Simulation of Radiation Effects in Solids (COSIRES) Shanghai, China, June 18-22, 2018.
17. Nasr M. Ghoniem, "Multiscale-Multiphysics Modelling of the Mechanics of Extreme Environment Materials," University of California at Irvine (UCI), May 19, 2019.
18. Nasr M Ghoniem, "Resilient Self-Healing Materials for the Extreme EnvironmentofSpace Electric Propulsion & Power," AFOSR/RQRS Future of In-Space Propulsion meeting, Aerospace Corporation, Los Angeles, California, May 21-23, 2019.
19. Nasr M Ghoniem, Discrete Multiscale Methods for the Physics and Mechanics of Defects, 13th International Conference on the Mechanical Behavior of Materials June 10-14, 2019, Melbourne, Australia.
20. Yinan Cui, Giacomo Po, Nasr Ghoniem , Plastic Instability of Micrometer-Scale Irradiated Materials, 19th International Conference on Fusion Reactor Materials La Jolla, CA, October 27-November 1, 2019.

3.2. Publications

1. Chang, Hsing-Yin, Andrew Alvarado, and Jaime Marian. "Calculation of secondary electron emission yields from low-energy electron deposition in tungsten surfaces." *Applied Surface Science* **450** (2018): 190-199.
2. Burbery, N. B., G. Po, R. Das, N. Ghoniem, and W. G. Ferguson. "Dislocation dynamics in polycrystals with atomistic-informed mechanisms of dislocation-grain boundary interactions." *Journal of Micromechanics and Molecular Physics* **2**, no. 01 (2017): 1750003.
3. Admal, Nikhil Chandra, Giacomo Po, and Jaime Marian. "A unified framework for polycrystal plasticity with grain boundary evolution." *International Journal of Plasticity* **106** (2018): 1-30.
4. Po, Giacomo, Markus Lazar, Nikhil Chandra Admal, and Nasr Ghoniem. "A non-singular theory of dislocations in anisotropic crystals." *International Journal of Plasticity* **103** (2018): 1-22.

5. Can Erel, Giacomo Po, Tamer Crosby, and Nasr Ghoniem. Generation and Interaction Mechanisms of Prismatic Dislocation Loops in FCC Metals. Computational Materials Science 140, 2107 https://doi.org/10.1016/j.commatsci.2017.07.043
6. Nikhil Chandra Admal, Giacomo Po and Jaime Marian. Diffuse-interface polycrystal plasticity: expressing grain boundaries as geometrically necessary dislocations. Materials Theory 2017, 1:6 https://doi.org/10.1186/s41313-017-0006-0
7. Can Erel, Giacomo Po, Nasr Ghoniem. Dependence of Hardening and Saturation Stress in Persistent Slip Bands on Strain Amplitude During Cyclic Fatigue Loading. Philosophical Magazine, 2017, 1-24. https://doi.org/10.1080/14786435.2017.13615550
8. Yinan Cui, Giacomo Po, Nasr Ghoniem. Does irradiation enhance or inhibit strain bursts at the submicron scale? Acta Materialia 132, 2017, 285-297. https://doi.org/10.1016/j.actamat.2017.04.055
9. Yinan Cui, Giacomo Po, and Nasr Ghoniem. Influence of loading control on strain bursts and dislocation avalanches at the nano- and micro-scale. Physical Review B. 2017, 95, 064103. https://doi.org/10.1103/PhysRevB.95.064103
10. David Rivera, Edward Gao, Yue Huang, Giacomo Po, Nasr M. Ghoniem. A Dislocation-Based Crystal Viscoplasticity Model with Application to Micro-engineered Plasma-Facing Materials. Journal of Nuclear Materials 485, 2017, p 231-242. http://dx.doi.org/10.1016/j.jnucmat.2016.12.034
11. Nikhil Chandra Admal, Jaime Marian, Giacomo Po. The atomistic representation of first strain-gradient elasticity tensors. JMPS 99, 2107, 93-115. http://dx.doi.org/10.1016/j.jmps.2016.11.005
12. Yinan Cui, Giacomo Po, Nasr Ghoniem. Controlling Strain Bursts and Avalanches at the Nano- and Micro-scales. PRL 117, 2106, pp. 155502. https://doi.org/10.1103/PhysRevLett.117.155502
13. CSR Matthes, NM Ghoniem, D Walgraef, Stability and symmetry of ion-induced surface patterning, *Materials Theory*, 2017, 1 (1), 5.
14. CSR Matthes, NM Ghoniem, GZ Li, TS Matlock, DM Goebel, CA Dodson, et al., Fluence-dependent sputtering yield of micro-architectured materials, *Applied Surface Science*, 2017, 407, 223-235.
15. GZ Li, TS Matlock, DM Goebel, CA Dodson, CSR Matthes, NM Ghoniem, ..., In situ plasma sputtering and angular distribution measurements for structured molybdenum surfaces, *Plasma Sources Science and Technology*, 2017, 26 (6), 065002
16. D Rivera, RE Wirz, N Ghoniem, Experimental measurements of surface damage and residual stresses in micro-engineered plasma facing materials, *Journal of Nuclear Materials*, 2017, 486, 111-121.
17. D Rivera, Y Huang, G Po, NM Ghoniem, A dislocation-based crystal viscoplasticity model with application to micro-engineered plasma-facing materials, *Journal of Nuclear Materials*, 2017 485, 231-242.
18. Andrew Sheng, Nasr Ghoniem, Tamer Crosby, Giacomo Po. A mesh-independent method for three-dimensional crack growth in finite geometry International Journal for Numerical Methods in Engineering, **117** (1), 38-62, 2019.
19. Jaime Marian, Steve Fitzgerald, Giacomo Po. "Discrete dislocation dynamics to simulate irradiation hardening: current capabilities, applications, and research needs." Chapter, edited

by Andreoni, W. and Yip, S., 2018. *Handbook of Materials Modeling Applications: Current and Emerging Materials*.

20. Anter El-Azab and Giacomo Po. Continuum Dislocation Dynamics: Classical Theory and Contemporary Models. Chapter, edited by Andreoni, W. and Yip, S., 2018. *Handbook of Materials Modeling Applications: Current and Emerging Materials*.
21. Po, Giacomo, Nikhil Chandra Admal, and Bob Svendsen. "Non-local Thermoelasticity Based on Equilibrium Statistical Thermodynamics." *Journal of Elasticity* (2019): **1-23**.
22. Po, Giacomo, Nikhil Chandra Admal, and Markus Lazar. "The Green tensor of Mindlin?s anisotropic first strain gradient elasticity." *Materials Theory* **3**, no. 1 (2019): 3.
23. Robert Shahram Shaefer, Nasr M Ghoniem, and Brian Williams. Cellular structures with interconnected microchannels, January 30 2018. US Patent 9,881,699.
24. Amir Abdelmawla, Tarek M Hatem, and Nasr M Ghoniem. Dislocation-based finite element modelling of hydrogen embrittlement in steel alloys. In *TMS Annual Meeting & Exhibition*, pages 213–223. Springer, Cham, 2018.
25. Yinan Cui and Nasr M Ghoniem. Spatio-temporal plastic instabilities at the nano/micro scale. *Journal of Micromechanics and Molecular Physics*, 2018.
26. Yinan Cui, Giacomo Po, and Nasr Ghoniem. Size-tuned plastic flow localization in irradiated materials at the submicron scale. *Physical review letters*, 120(21):215501, 2018.
27. Yinan Cui, Giacomo Po, and Nasr Ghoniem. Suppression of localized plastic flow in irradiated materials. *Scripta Materialia*, 154:34–39, 2018.
28. Yinan Cui, Giacomo Po, and Nasr M Ghoniem. A coupled dislocation dynamics-continuum barrier field model with application to irradiated materials. *International Journal of Plasticity*, 104:54–67, 2018.
29. Edward Gao and Nasr M Ghoniem. A coupled rate theory-monte carlo model of helium bubble evolution in plasma-facing micro-engineered tungsten. *Journal of Nuclear Materials*, 509:577–590, 2018.
30. Edward Gao, Warren Nadvornick, Russ Doerner, and Nasr M Ghoniem. The influence of low-energy helium plasma on bubble formation in micro-engineered tungsten. *Journal of Nuclear Materials*, 501:319–328, 2018.
31. Nasr Ghoniem and Yinan Cui. Strain bursts and dislocation avalanches in obstacle-hardened materials. *Bulletin of the American Physical Society*, 2018.
32. Yue Huang, Fabio Cismondi, Eberhard Diegele, Giafranco Federici, Alessandro Del Nevo, Fabio Moro, and Nasr Ghoniem. Thermo-structural design of the european demo water-cooled blanket with a multiscale-multiphysics framework. *Fusion Engineering and Design*, 135:31–41, 2018.
33. Giacomo Po, Markus Lazar, Nikhil Chandra Admal, and Nasr Ghoniem. A non-singular theory of dislocations in anisotropic crystals. *International Journal of Plasticity*, 103:1–22, 2018.
34. Stefanos Papanikolaou, Yinan Cui, and Nasr Ghoniem. Avalanches and plastic flow in crystal plasticity: an overview. *Modelling and Simulation in Materials Science and Engineering*, 26(1):013001, 2017.
35. Po, Giacomo, Yue Huang, and Nasr Ghoniem. "A continuum dislocation-based model of wedge microindentation of single crystals." *International Journal of Plasticity* **114** (2019): 72-86.

36. Y Cui, G Po, P Srivastava, K Jiang, V Gupta, N Ghoniem, "The role of slow screw dislocations in controlling fast strain avalanche dynamics in body-centered cubic metals," *International Journal of Plasticity* 2019.
37. A Alvarado, HY Chang, W Nadvornick, N Ghoniem, J Marian, "Monte Carlo raytracing method for calculating secondary electron emission from micro-architected surfaces," *Applied Surface Science* **478**, 142-149, 2019.
38. Y Cui, G Po, YP Pellegrini, M Lazar, N Ghoniem, "Computational 3-dimensional dislocation elastodynamics,' *Journal of the Mechanics and Physics of Solids*, **126**, 20-51,2019
39. E Gao, R Doerner, B Williams, NM Ghoniem, "Low-energy helium plasma effects on textured micro-porous tungsten," *Journal of Nuclear Materials*, **517**, 86-96, 2019.
40. Y Cui, N Ghoniem, "Influence of Size on the Fractal Dimension of Dislocation Microstructure," *Metals*, **9** (4), 478, 2019.
41. Hsing-Yin Chang, Andrew Alvarado, Trey Weber, Jaime Marian, "Monte Carlo modeling of low-energy electron-induced secondary electron emission yields in micro-architected boron nitride surfaces", *Nuclear Instruments and Methods in Physics Research* Section B: Beam Interactions with Materials and Atoms, Volume **454**, 2019, 14-22.
42. Hsing-Yin Chang, Andrew Alvarado, Jaime Marian, "Calculation of secondary electron emission yields from low-energy electron deposition in tungsten surfaces," *Applied Surface Science*, Volume **450**, 2018, 190-199 (https://doi.org/10.1016/j.apsusc.2018.04.155)

3.3. Honors & Awards

During the project period, the principal investigator has had the following list of honors & awards:

- Nominated to the National Academy of Engineering.
- General Chair, The Nineteenth International Conference on Fusion Reactor Materials, La Jolla, California, October 27-November 1, 2019.
- Fellow of the Materials Research Society, MRS.
- Fellow of the American Nuclear Society, ANS.
- Fellow of the American Society of Mechanical Engineers, ASME.
- Fellow of the American Academy of Mechanics, AAM.
- Fellow of the Japan Society for Promotion of Science, JSPS.

Acknowledgements

The authors would like to acknowledge the support of the U.S. Air Force Office of Scientific Research (AFOSR), under research grant number FA9550-16-1-0444 with UCLA.

4. Bibliography

References

[1] C. S. Matthes, N. M. Ghoniem, G. Z. Li, T. S. Matlock, D. M. Goebel, C. A. Dodson, R. E. Wirz, Fluence-dependent sputtering yield of micro-architectured materials, Applied Surface Science 407 (2017) 223–235.

[2] J.-H. Song, H. Wang, T. Belytschko, A comparative study on finite element methods for dynamic fracture, Computational Mechanics 42 (2) (2008) 239–250.

[3] T. Rabczuk, Computational methods for fracture in brittle and quasi-brittle solids: state-of-the-art review and future perspectives, ISRN Applied Mathematics 2013.

[4] A. Sheng, N. Ghoniem, T. Crosby, G. Po, A mesh-independent method for planar three-dimensional crack growth in finite domains, International Journal for Numerical Methods in Engineering .

[5] J. Eshelby, F. Frank, F. Nabarro, XLI. The equilibrium of linear arrays of dislocations., The London, Edinburgh, and Dublin Philosophical Magazine and Journal of Science 42 (327) (1951) 351–364.

[6] N. M. Ghoniem, R. Amodeo, Computer Simulation of Dislocation Pattern Formation, vol. 3, Solid State Phenomena, 1988.

[7] G. Po, M. S. Mohamed, T. Crosby, C. Erel, A. El-Azab, N. Ghoniem, Recent progress in discrete dislocation dynamics and its applications to micro plasticity, JOM 66 (10) (2014) 2108–2120.

[8] E. Van der Giessen, A. Needleman, Discrete dislocation plasticity: a simple planar model, Modelling and Simulation in Materials Science and Engineering 3 (5) (1995) 689.

[9] N. Ghoniem, M, S.-H. Tong, L. Sun, Parametric dislocation dynamics: a thermodynamics-based approach to investigations of mesoscopic plastic deformation, Physical Review B 61 (2) (2000) 913.

[10] R. W. Conversano, D. M. Goebel, R. R. Hofer, T. S. Matlock, R. E. Wirz, Development and initial testing of a magnetically shielded miniature Hall thruster, IEEE Transactions on Plasma Science 43 (1) (2015) 103–117.

[11] F. Roters, D. Raabe, G. Gottstein, Calculation of stress—strain curves by using 2 dimensional dislocation dynamics, Comp Mater Sci 7 (1) (1996) 56–62.

[12] K. M. Davoudi, L. Nicola, J. J. Vlassak, Dislocation climb in two-dimensional discrete dislocation dynamics, J Appl Phys 111 (10) (2012) 103522.

[13] S. M. Keralavarma, T. Cagin, A. Arsenlis, A. A. Benzerga, Power-Law Creep from Discrete Dislocation Dynamics, Phys Rev Lett 109 (26) (2012) 265504.

[14] W. Cai, V. V. Bulatov, Mobility laws in dislocation dynamics simulations, Mat Sci Eng A 387 (2004) 277–281.

[15] D. Mordehai, E. Clouet, M. Fivel, M. Verdier, Introducing dislocation climb by bulk diffusion in discrete dislocation dynamics, Philosophical Magazine 88 (6) (2008) 899–925.

[16] B. Bako, E. Clouet, L. M. Dupuy, M. Bletry, Dislocation dynamics simulations with climb: kinetics of dislocation loop coarsening controlled by bulk diffusion, Philosophical Magazine 91 (23) (2011) 3173–3191.

[17] G. Po, N. M. Ghoniem, A variational formulation of constrained dislocation dynamics coupled with heat and vacancy diffusion, J Mech Phys Solids 66 (2014) 103–116.

[18] A. Ma, F. Roters, D. Raabe, On the consideration of interactions between dislocations and grain boundaries in crystal plasticity finite element modeling – Theory, experiments, and simulations, Acta Materialia 54 (8) (2006) 2181–2194.

[19] N. Kheradmand, A. F. Knorr, M. Marx, Y. Deng, Microscopic incompatibility controlling plastic deformation of bicrystals, Acta Materialia 106 (2016) 219–228.

[20] R. J. Amodeo, N. M. Ghoniem, Dislocation dynamics. I. A proposed methodology for deformation micromechanics, Physical Review B 41 (10) (1990) 6958–6967, URL http://link.aps.org/%Doi/10.1103/PhysRevB.41.6958.

[21] G. Po, M. Lazar, D. Seif, N. Ghoniem, Singularity-free dislocation dynamics with strain gradient elasticity, Journal of the Mechanics and Physics of Solids 68 (0) (2014) 161–178.

[22] N. Burbery, G. Po, R. Das, N. Ghoniem, W. Ferguson, Dislocation dynamics in polycrystals with atomistic-informed mechanisms of dislocation-grain boundary interactions, Journal of Micromechanics and Molecular Physics (2017) 1750003.

[23] L. Priester, D. Yu, Triple junctions at the mesoscopic, microscopic and nanoscopic scales, Materials Science and Engineering: A 188 (1) (1994) 113–119.

[24] G. Po, M. Mohamed, T. Crosby, C. Erel, A. El-Azab, N. Ghoniem, Recent Progress in Discrete Dislocation Dynamics and Its Applications to Micro Plasticity, JOM 66 (10) (2014) 2108–2120.

[25] N. Po, Giacomo; Ghoniem, Mechanics of Defect Evolution Library (MoDEL), URL https://bitbucket.org/model/model/src/9591cab213e1fa7d6eb9835ab8ca30179eab5b6e?at=polycrystals, 2017.

[26] T. C. Lee, I. M. Robertson, H. K. Birnbaum, TEM in situ deformation study of the interaction of lattice dislocations with grain boundaries in metals, Philosophical Magazine A 62 (1) (1990) 131–153.

[27] T. P. Darby, R. Schindler, R. W. Balluffi, On the interaction of lattice dislocations with grain boundaries, Philosophical Magazine A 37 (2) (1978) 245–256.

[28] W. Rachinger, Creep processes in polycrystalline aluminium, Acta Metallurgica 7 (6) (1959) 374–375, ISSN 0001-6160.

[29] L. Priester, "Dislocation–interface" interaction — stress accommodation processes at interfaces, Materials Science and Engineering: A 309–310 (0) (2001) 430–439.

[30] Z. Shen, R. Wagoner, W. Clark, Dislocation pile-up and grain boundary interactions in 304 stainless steel, Scripta metallurgica 20 (6) (1986) 921–926, ISSN 0036-9748.

[31] J. Kacher, B. P. Eftink, B. Cui, I. M. Robertson, Dislocation interactions with grain boundaries, Current Opinion in Solid State and Materials Science 18 (4) (2014) 227–243.

[32] C. T. Forwood, L. M. Clarebrough, Prismatic glide and slip transfer across a high-angle grain boundary, Philosophical Magazine A 44 (1) (1981) 31–41.

[33] Y. Gao, Z. Zhuang, X. You, A hierarchical dislocation-grain boundary interaction model based on 3D discrete dislocation dynamics and molecular dynamics, Science China Physics, Mechanics and Astronomy 54 (4) (2011) 625–632.

[34] J. W. Kysar, Y. X. Gan, T. L. Morse, X. Chen, M. E. Jones, High strain gradient plasticity associated with wedge indentation into face-centered cubic single crystals: Geometrically necessary dislocation densities, J Mech Phys Solids 55 (7) (2007) 1554–1573.

[35] J. W. Kysar, Y. Saito, M. S. Oztop, D. Lee, W. T. Huh, Experimental lower bounds on geometrically necessary dislocation density, Int J Plasticity 26 (8) (2010) 1097–1123.

[36] A. Gouldstone, N. Chollacoop, M. Dao, J. Li, A. M. Minor, Y.-L. Shen, Indentation across size scales and disciplines: Recent developments in experimentation and modeling, Acta Mater 55 (12) (2007) 4015–4039.

[37] D. Tabor, The Hardness of Metals, Oxford University Press, 2000.

[38] A. Gouldstone, H. J. Koh, K. Y. Zeng, A. E. Giannakopoulos, S. Suresh, Discrete and continuous deformation during nanoindentation of thin films, Acta Mater 48 (9) (2000) 2277–2295.

[39] W. D. Nix, H. Gao, Indentation size effects in crystalline materials: A law for strain gradient plasticity, J Mech Phys Solids 46 (3) (1998) 411–425.

[40] V. L. Berdichevsky, Continuum theory of dislocations revisited, Continuum Mech. Thermodyn. 18 (2006) 195–222.

[41] M. A. Makeev, R. Cuerno, A.-L. Barabasi, Morphology of ion-sputtered surfaces, Nuclear Instruments and Methods in Physics Research Section B: Beam Interactions with Materials and Atoms 197 (3) (2002) 185–227.

[42] G. Costantini, S. Rusponi, F. B. de Mongeot, C. Boragno, U. Valbusa, Periodic structures induced by normal-incidence sputtering on Ag (110) and Ag (001): flux and temperature dependence, Journal of Physics: Condensed Matter 13 (26) (2001) 5875.

[43] S. Habenicht, Morphology of graphite surfaces after ion-beam erosion, Physical Review B 63 (12) (2001) 125419.

[44] M. Navez, C. Sella, D. Chaperot, Nonlinear Ripple Dynamics on Amorphous Surfaces Patterned by Ion Beam Sputtering, Czetch Republic Academy of Science 254 (1962) 240.

[45] S. Rusponi, C. Boragno, U. Valbusa, Ripple structure on Ag (110) surface induced by ion sputtering, Physical review letters 78 (14) (1997) 2795.

[46] U. Valbusa, C. Boragno, F. B. de Mongeot, Nanostructuring surfaces by ion sputtering, Journal of Physics: Condensed Matter 14 (35) (2002) 8153.

[47] P. Sigmund, A mechanism of surface micro-roughening by ion bombardment, Journal of Materials Science 8 (11) (1973) 1545–1553, ISSN 0022-2461.

[48] R. M. Bradley, J. M. Harper, Theory of ripple topography induced by ion bombardment, Journal of Vacuum Science & Technology A: Vacuum, Surfaces, and Films 6 (4) (1988) 2390–2395.

[49] R. Asaro, W. Tiller, Interface morphology development during stress corrosion cracking: Part I. Via surface diffusion, Metallurgical Transactions 3 (7) (1972) 1789–1796.

[50] J. Paret, Long-time dynamics of the three-dimensional biaxial Grinfeld instability, Physical Review E 72 (1) (2005) 011105.

[51] K. Kassner, C. Misbah, J. Müller, J. Kappey, P. Kohlert, Phase-field modeling of stress-induced instabilities, Physical Review E 63 (3) (2001) 036117.

[52] P. Sigmund, Theory of sputtering. I. Sputtering yield of amorphous and polycrystalline targets, Physical review 184 (2) (1969) 383.

[53] R. Cuerno, A.-L. Barabási, Dynamic scaling of ion-sputtered surfaces, Physical review letters 74 (23) (1995) 4746.

[54] R. M. Bradley, Redeposition of sputtered material is a nonlinear effect, Physical Review B 83 (7) (2011) 075404.

[55] M. Kardar, G. Parisi, Y.-C. Zhang, Dynamic scaling of growing interfaces, Physical Review Letters 56 (9) (1986) 889.

[56] C. Godrèche, Solids far from Equilibrium, vol. 1, Cambridge University Press, 1991.

[57] J. Villain, Continuum models of crystal growth from atomic beams with and without desorption, Journal de physique I 1 (1) (1991) 19–42.

[58] Y. Kuramoto, T. Tsuzuki, Persistent propagation of concentration waves in dissipative media far from thermal equilibrium, Progress of theoretical physics 55 (2) (1976) 356–369.

[59] G. Sivashinsky, Nonlinear analysis of hydrodynamic instability in laminar flames. Derivation of basic equations, Acta astronautica 4 (11) (1977) 1177–1206.

[60] A. Keller, S. Facsko, Ion-induced nanoscale ripple patterns on Si surfaces: theory and experiment, Materials 3 (10) (2010) 4811–4841.

[61] S. Facsko, T. Bobek, A. Stahl, H. Kurz, T. Dekorsy, Dissipative continuum model for self-organized pattern formation during ion-beam erosion, Physical Review B 69 (15) (2004) 153412.

[62] H. Bethe, Zur theorie des durchgangs schneller korpuskularstrahlen durch materie, Annalen der Physik 397 (3) (1930) 325–400.

[63] R. Shimizu, Y. Kataoka, T. Ikuta, T. Koshikawa, H. Hashimoto, A Monte Carlo approach to the direct simulation of electron penetration in solids, Journal of Physics D: Applied Physics 9 (1) (1976) 101.

[64] I. Adesida, R. Shimizu, T. Everhart, A study of electron penetration in solids using a direct Monte Carlo approach, Journal of Applied Physics 51 (11) (1980) 5962–5969.

[65] R. Shimizu, D. Ze-Jun, Monte Carlo modelling of electron-solid interactions, Reports on Progress in Physics 55 (4) (1992) 487.

[66] Z.-J. Ding, R. Shimizu, A Monte Carlo modeling of electron interaction with solids including cascade secondary electron production, Scanning 18 (2) (1996) 92–113.

[67] N. F. Mott, The scattering of fast electrons by atomic nuclei, Proceedings of the Royal Society of London. Series A, Containing Papers of a Mathematical and Physical Character 124 (794) (1929) 425–442.

[68] L. Reimer, B. Lödding, Calculation and tabulation of mott cross-sections for large-angle electron scattering, Scanning 6 (3) (1984) 128–151.

[69] R. Browning, T. Li, B. Chui, J. Ye, R. Pease, Z. Czyzewski, D. Joy, Low-energy electron/atom elastic scattering cross sections from 0.1–30 keV, Scanning 17 (4) (1995) 250–253.

[70] R. Browning, T. Li, B. Chui, J. Ye, R. Pease, Z. Czyżewski, D. Joy, Empirical forms for the electron/atom elastic scattering cross sections from 0.1 to 30 keV, Journal of Applied Physics 76 (4) (1994) 2016–2022.

[71] M. Gryziński, Classical theory of atomic collisions. I. Theory of inelastic collisions, Physical Review 138 (2A) (1965) A336.

[72] M. Gryziński, Two-particle collisions. I. General relations for collisions in the laboratory system, Physical Review 138 (2A) (1965) A305.

[73] M. Gryziński, Two-particle collisions. II. Coulomb collisions in the laboratory system of coordinates, Physical Review 138 (2A) (1965) A322.

[74] M. Gryziński, Classical theory of electronic and ionic inelastic collisions, Physical Review 115 (2) (1959) 374.

[75] H. Stolz, Zur Theorie der Sekundärelektronenemission von Metallen Der Transportprozeß, Annalen der Physik 458 (3-4) (1959) 197–210.

[76] R. A. Ferrell, Characteristic energy loss of electrons passing through metal foils. II. Dispersion relation and short wavelength cutoff for plasma oscillations, Physical Review 107 (2) (1957) 450.

[77] R. A. Ferrell, Angular dependence of the characteristic energy loss of electrons passing through metal foils, Physical Review 101 (2) (1956) 554.

[78] D. Drouin, R. Gauvin, D. C. Joy, Computation of polar angle of collisions from partial elastic mott cross-sections, Scanning 16 (2) (1994) 67–77.

[79] Y. Lin, A study of the secondary electrons .

[80] D. C. Joy, A. D. Romig Jr, J. Goldstein, Principles of analytical electron microscopy, Springer Science & Business Media, 1986.

[81] N. F. Mott, The scattering of fast electrons by atomic nuclei, in: Sir Nevill Mott–65 Years In Physics, World Scientific, 13–30, 1995.

[82] S.-R. Lin, N. Sherman, J. K. Percus, Elastic scattering of relativistic electrons by screened atomic nuclei, Nuclear Physics 45 (1963) 492–504.

[83] P. Bunyan, J. Schonfelder, Polarization by mercury of 100 to 2000 eV electrons, Proceedings of the Physical Society 85 (3) (1965) 455.

[84] Y. Sun, H. Xu, B. Da, S.-f. Mao, Z.-j. Ding, Calculations of Energy-Loss Function for 26 Materials, Chinese Journal of Chemical Physics 29 (6) (2017) 663.

[85] J. Ashley, Interaction of low-energy electrons with condensed matter: stopping powers and inelastic mean free paths from optical data, Journal of electron spectroscopy and related phenomena 46 (1) (1988) 199–214.

[86] H. Weghorst, G. Hooper, D. P. Greenberg, Improved computational methods for ray tracing, ACM Transactions on Graphics (TOG) 3 (1) (1984) 52–69.

[87] M. Schmidt, H. Lipson, Distilling free-form natural laws from experimental data, science 324 (5923) (2009) 81–85.

[88] M. Schmidt, H. Lipson, Eureqa (version 0.98 beta)[software], Nutonian, Somerville, Mass, USA .

[89] H.-Y. Chang, A. Alvarado, J. Marian, Calculation of secondary electron emission yields from low-energy electron deposition in tungsten surfaces, Applied Surface Science 450 (2018) 190–199.

[90] A. Alvarado, H.-Y. Chang, W. Nadvornick, N. Ghoniem, J. Marian, Monte Carlo Raytracing Method for Calculating Secondary Electron Emission from Micro-Architected Surfaces, Applied Surface Science .

[91] J. F. Ziegler, M. D. Ziegler, J. P. Biersack, SRIM–The stopping and range of ions in matter (2010), Nuclear Instruments and Methods in Physics Research Section B: Beam Interactions with Materials and Atoms 268 (11-12) (2010) 1818–1823.

[92] M. Nakles, J. Pierru, J. Wang, M. Domonkos, Experimental and Modeling Studies of Low Energy Ion Sputtering in Ion Thrusters, in: 39th AIAA/ASME/SAE/ASEE Joint Propulsion Conference and Exhibit, 5160, 2004.

[93] I. Garkusha, A. Burdakov, I. Ivanov, E. Kruglyakov, K. Kuklin, I. Landman, V. Makhlaj, S. Polosatkin, A. Shoshin, V. Tereshin, et al., PLASMA-SURFACE INTERACTION DURING ITER TRANSIENT EVENTS: SIMULATION WITH QSPA Kh-50 & GOL-3 FACILITIES, Problems of Atomic Science & Technology (6) (2008) 58–60.

[94] V. Makhlaj, I. Garkusha, N. Aksenov, A. Chuvilo, M. Ladygina, I. Landman, J. Linke, S. Malykhin, S. Pestchanyi, A. Pugachev, et al., Simulation of ITER edge-localized modes' impacts on the divertor surfaces within plasma accelerators, Physica Scripta 2011 (T145) (2011) 014061.

[95] D. Rivera, T. Crosby, A. Sheng, N. M. Ghoniem, Characterization of thermomechanical damage on tungsten surfaces during long-duration plasma transients, Journal of Nuclear Materials 455 (1) (2014) 500–506.

[96] W. Wolfer, M. Ashkin, A. Boltax, Creep and swelling deformation in structural materials during fast-neutron irradiation, ASTM-STP 570 (1975) 233–52.